INVESTIGATION INTO SOFT TEMPLATED BIOACTIVE GLASS NANO PARTICLES FOR BIOMEDICAL APPLICATIONS

THESIS SUBMITTED TO
DELHI TECHNOLOGICAL UNIVERSITY
FOR THE AWARD OF THE DEGREE OF
DOCTOR OF PHILOSOPHY

Submitted by

Namit Dey
(Roll No. 2K18/Ph.D./BT/512)

Under the Supervision of

Dr. ASMITA DAS
DEPARTMENT OF BIOTECHNOLOGY

&

Dr. DEENAN SANTHIYA
DEPARTMENT OF APPLIED CHEMISTRY

DEPARTMENT OF BIOTECHNOLOGY
DELHI TECHNOLOGICAL UNIVERSITY
SHAHBAD DAULATPUR, MAIN BAWANA ROAD,
DELHI-110042, INDIA
OCTOBER 2023

A thesis submitted to the Department of Biotechnology, Delhi Technological University in partial fulfilment of the requirement for degree of Doctor in Philosophy.

Dedicated to my family

Department of Biotechnology
Delhi Technological University
(Formally Delhi College of Engineering)
Shahbad-Daulatpur, Bawana Road
Delhi-110042, India

DECLARATION

This is to certify that the work presented in this thesis entitled "**Investigation into soft templated bioactive glass nano particles for biomedical applications**" is original and has been carried out by me for the degree of **Doctor of Philosophy** under the supervision of **Dr. Asmita Das, Assistant Professor, Department of Biotechnology** and **Dr. Deenan Santhiya, Assistant Professor, Department of Applied Chemistry**.

I hereby certify that the work presented in this thesis is a compilation of my own studies and investigations carried out at Delhi Technological University during the period from January 2019 to May 2023, except where otherwise stated.

Namit Dey
October 2023

Department of Biotechnology
Delhi Technological University
(Formally Delhi College of Engineering)
Shahbad-Daulatpur, Bawana Road
Delhi-110042, India

CERTIFICATE

This is to certify that the Ph.D. thesis entitled "**Investigation into soft templated bioactive glass nano particles for biomedical applications**" submitted to the Delhi Technological University, Delhi-110042, India in fulfillment of the requirements for the award of the degree of **Doctor of Philosophy** has been carried out by the candidate Namit Dey under the supervision of **Dr. Asmita Das**, **Assistant Professor, Department of Biotechnology** and **Dr. Deenan Santhiya**, **Assistant Professor, Department of Applied Chemistry**. It is further certified that the work embodied in this thesis has neither partially nor fully submitted to any other university or Institution for the award of any degree or diploma.

Dr. Asmita Das
Asst. Professor
Department of Biotechnology
Delhi Technological University
Shahbad Daulatpur
Bawana, Delhi-110042

Dr. Deenan Santhiya
Asst. Professor
Department of Applied Chemistry
Delhi Technological University
Shahbad Daulatpur
Bawana, Delhi-110042

Prof. Yasha Hasija
Head of Department
Department of Biotechnology
Delhi Technological University
Shahbad Daulatpur
Bawana, Delhi-110042

ACKNOWLEDGEMENT

First of all, I would like to acknowledge the blessings of God for guiding me throughout my life and my PhD, and providing me with the strength and courage to overcome multiple difficulties during this journey, some of which seemed unsurmountable at times. Secondly, I would like to take this opportunity to express my deep appreciation and gratitude to all those who have contributed to the completion of my thesis.

I owe my heartfelt gratitude to Hon'ble Vice Chancellor, Delhi Technological University, for his unconditional support and kind encouragement throughout the work.

I am immensely thankful to my thesis advisors, Dr. Asmita Das and Dr. Deenan Santhiya for their unwavering support, guidance, and expertise throughout the entire research process. I express my immense gratitude towards Dr. Asmita for ensuring that my entire PhD journey was smooth and stress-free. Dr. Santhiya has not only been my mentor for this research work, but also for my life decisions during the time we worked together on this thesis. Her valuable advice and our discussions about life and work are something I will cherish for the rest of my life. She has been the support that gave me strength, especially during the times when things got really difficult and I was on the verge of giving up. I will continue to seek her advice throughout my life.

I would like to extend my gratitude to Prof. Yasha Hasija (HOD, Biotechnology), my doctoral research committee members, Prof. Jai Gopal Sharma, Prof. Pravir Kumar, and Dr. Navneeta Bharadvaja, DRC external members Prof. Sonika Bhatnagar, Prof. A.K Dubey, SRC external

members Dr. Tulika Prasad and Prof. Indrajit Roy for their insightful feedback and constructive suggestions. Your collective wisdom has significantly enriched the quality of this work.

My research work would not have been possible without the contributions of Mr. C B Singh, Mr. Jitender, and all the office staff from the Department of Biotechnology, DTU. I am also thankful to the HOD and faculty of Department of Applied chemistry, DTU, and all the supporting staff for allowing me to carry out the majority of my studies in the chemistry department.

A special gratitude goes to Dr. Munia Ganguli for paving the way for me to acquire this PhD position and for her guidance throughout my research. I am immensely thankful to her for providing the opportunity to carry out many of my studies in her lab at CSIR IGIB.

My journey as a PhD student is incomplete without mentioning my lab mates from my labs in DTU and IGIB. I would like to express my gratitude towards Ms. Neha Tiwari, whose formidable support has made this journey possible to say the least. I am thankful to Dr. Nidhi, Dr. Meenakshi Gautam, Dr. Manjot Kaur, Dr. Himansh Goyal, Dr. Sunil, Ms. Megha, Ms. Divya Goel, Ms. Narjes and Ms. Krizma for always being there to help me in every possible way. Also, my lab mates from CSIR IGIB Dr. Sarita, Dr. Anupama, Dr. Aanchal, Dr. Simanti, Ms. Betsy, Ms. Divya Rao and my buddies Franklin and Sabyasachi deserve special mention. All of them have been really kind to me throughout my journey, and I respect them immensely for being there when I needed them the most. Their companionship is something I will miss once I leave, and I will cherish all the time we spent together, both good and bad, throughout my life.

My heartfelt thanks go to my family and friends for their constant support and encouragement. Your belief in me sustained me through the challenging moments of this journey.

I would like to express my appreciation to the Department of Science and Technology (DST-SERB), Government of India, for their financial support, which made it possible for me to pursue my studies and research. Last but not least, I want to acknowledge the entire Delhi Technological University community for providing the necessary resources and a conducive environment for academic excellence. This thesis represents not only my work but also the collective efforts of all those who have been part of this academic endeavor.

Thank you for being a part of this journey.

Namit Dey
Department of Biotechnology,
October, 2023.

ABSTRACT

Bioactive glass nanoparticles have numerous applications in the repair and regeneration of both hard and soft tissue. It has also used widely as drug delivery vehicle. Through the bio-inspired route of synthesis, bioactive glass nanoparticles can be synthesized with minimum non-green chemicals, time, energy, and cost-to-synthesis. Although surfactants are traditionally referred to as soft templates, we have used components like glycosaminoglycans (hyaluronic acid), drugs (doxorubicin) and biomolecules (gelatin) as alternative to the traditional soft templates. The bio-inspired route allows for the use of both hard and soft templates to easily initiate the synthesis and formation of nano-sized, mesoporous, amorphous, bioactive, and biocompatible bioactive glass nanoparticles. Additionally, the absence of a calcination step allows the template to be retained within the nanoparticles, providing specific properties to the resulting bioactive glass.

In this thesis, we explore alternative templates, such as gelatin-calcium carbonate nanocomposites, doxorubicin, and hyaluronic acid, as substitutes for traditional surfactants for synthesizing bioactive glass. The goal is to harness the advantages that the bio-inspired route offers in terms of applications of range of templates that would ideally be difficult in case of traditional synthesis methods like sol-gel and melting quenching due to either high temperature involved in synthesis or calcination process or use of non-green solvents and synthetic surfactants.

In the first study, we report a surfactant free route to synthesize hollow mesoporous bioactive glass nanoparticles at ambient atmospheric condition. Here, through the bio-inspired route, gelatin is utilized as soft template for synthesizing calcium carbonate nanocomposites which in turn gives rise to hollow bioactive glasses through multiple steps. The synthesized particles contain hollow core as a result of mild acid mediated removal of gelatin-calcium carbonate nanoparticles used as hard template. Removal of template was confirmed through FTIR and

XRD while round morphology and sizes below 100 nm could be observed by TEM. In addition, N_2 adsorption and desorption analysis confirmed hollow and mesoporous nature of the bioactive glass shell. Interestingly, post removal of template, particles reported higher surface area, pore volume and pore diameter along with decrease in surface charge. Deposition of hydroxyapatite on hollow bioactive glass in Simulated Buffer Fluid (SBF) could be observed from Day 7 of immersion while well-developed hydroxyapatite depositions could be observed by Day 30. This proved bioactivity of the material while cytotoxicity analysis on Human Osteosarcoma cell line (U2OS) through MTT assay proved the biocompatible nature of the hollow bioactive glass particle.

In the second study, a common anti-cancer drug doxorubicin solution in Tris buffer acts as a soft template for preparing bioactive glass nanocomposites. Doxorubicin preparation with bioactive glass as a novel hybrid nanoparticle formulation was carried out through the bio-inspired route where different precursors of bioactive glass are added to a Tris(hydroxymethyl)aminomethane buffer adjusted to slightly alkaline pH containing doxorubicin. With increasing concentration of doxorubicin, loading increased in quantity with comparatively higher drug release in acidic pH than neutral pH. Without synthetic surfactant or high temperature calcination, bioactive glass-ceramic nanoparticles demonstrated significantly superior cytotoxic behavior towards osteosarcoma cell line when compared to equivalent free drug or its action towards non-cancerous cell line. The particles exhibited hydroxayapatite deposition when immersed in simulated body fluid for 7 days. The bio-inspired route for synthesis of doxorubicin-bioactive glass-ceramic hybrid nanoparticles was an efficient cost-effective synthesis mechanism which is environmentally friendly without hampering the stability or activity of the drug.

Novel HA nano-formulations are constantly in demand due to its applications ranging from the medical to cosmeceutical industries. Therefore, in the third study, we explored a novel nano-

composition of HA and bioactive glass (BG) for the delivery of HA across biological barriers. Using a bio-inspired method, HA, acting as soft template and mixed with Tris(hydroxymethyl)aminomethane buffer at mild alkaline pH was able to direct the synthesis of amorphous hyaluronic acid-bioactive glass nano-composites (BGHA) with step-wise addition of precursors. Unlike the traditional Stober's method, the synthesis process does not require ethanol or ammonia, making it more environment friendly. The non-requirement of high-temperature calcination also makes the process energy efficient. The inherently mesoporous BGHA nano-composites demonstrate effective penetration across biological barriers, such as skin and bone cell membranes in *in-vitro* cell culture and human skin mimicking artificial skin membrane in *ex-vivo* studies. Further studies were conducted to analyze retention and penetration in keratinocytes, which form a viable barrier in the skin in addition to the lipid barrier. In addition, we externally conjugated HA to BGHA and observed similar results. Overall, nano-composition of high molecular weight hyaluronic acid (HA) and bioactive glass (BG) for efficient delivery of HA across biological barriers explored through the bio-inspired method can have potential medical and cosmeceutical applications if investigated further.

LIST OF PUBLICATIONS

- "Zein coated calcium carbonate nanoparticles for the targeted controlled release of model antibiotic and nutrient across the intestine."
  Meenakshi Gautam, Deenan Santhiya, and **Namit Dey**.
  Materials Today Communications 25 (2020): 101394.

- "Bioactivity reinforced surface patch bound collagen-pectin hydrogel."
  Himansh Goel, Nidhi Gupta, Deenan Santhiya, **Namit Dey**, Himadri B. Bohidar, and Aditi Bhattacharya.
  International journal of biological macromolecules 174 (2021): 240-253.

- "Pathway-driven peptide–bioglass nanocomposites as the dynamic and self-healable matrix."
  Nidhi Gupta, Ashmeet Singh, **Namit Dey**, Sabyasachi Chattopadhyay, Jojo P. Joseph, Deepika Gupta, Munia Ganguli, and Asish Pal.
  Chemistry of Materials 33, no. 2 (2021): 589-599.

- "Bio-Inspired Synthesis of Hollow Mesoporous Bioactive Glass Nanoparticles Using Calcium Carbonate as Solid Template."
  Namit Dey, Deenan Santhiya, and Asmita Das.
  ChemistrySelect 7, no. 12 (2022): e202200392.

- "One-Pot Synthesis of Doxorubicin-Bioactive Glass-Ceramic Hybrid Nanoparticles through a Bio-Inspired Route for Anti-Cancer Therapy."
  Namit Dey, Deenan Santhiya, and Asmita Das
  ChemistrySelect 8, no. 5 (2023): e202203664.

CONTENTS

Page no.

LIST OF FIGURES

LIST OF TABLES

LIST OF ABBREVIATIONS

0.25 BGHA	Hyaluronic-acid bioactive glass nanocomposite prepared at 0.25 mg/ml concentration of hyaluronic acid
0.25 DOX-BG	Doxorubicin-bioactive glass nanocomposite prepared at 0.25 mg/ml DOX concentration
0.5 BGHA	Hyaluronic-acid bioactive glass nanocomposite prepared at 0.50 mg/ml concentration of hyaluronic acid
0.5 DOX-BG	Doxorubicin-bioactive glass nanocomposite prepared at 0.5 mg/ml DOX concentration
0.75 DOX-BG	Doxorubicin-bioactive glass nanocomposite prepared at 0.75 mg/ml DOX concentration
1.0 BGHA	Hyaluronic-acid bioactive glass nanocomposite prepared at 1 mg/ml concentration of hyaluronic acid
AFM	Atomic Force Microscopy
APTES	(3-Aminopropyl)triethoxysilane
AR	Analytical Reagent
BET	Brunauer-Emmett-Teller
BG	Bioactive glass
BGHA	Bioactive glass -Hylauronic acid nanocomposite
BJH	Barrett-Joyner-Halenda
Ca^{2+}	Divalent calcium ion
CaAc	Calcium Acetate
CCNP	Calcium Carbonate nanoparticle
CCNP-BG	Calcium Carbonate nanoparticles coated with bioactive glass
CLSM	Confocal laser scanning microscope
CT	Calf-thymus
CTAB	Cetyltrimethylammonium bromide
DMEM	Dulbecco's modified Eagle's medium
DMF	Dimethylformamide

DMMB	Dimethylmethylene blue
DMSO	Dimethyl sulfoxide
DNA	Deoxyribonucleic acid
DOX	Doxorubicin
DOX-BG	Doxorubicin-bioactive glass nanocomposite
EDC	Ethylene dichloride
EDS	Energy-Dispersive X-ray Spectroscopy
F127	Pluronic F127 surfactant
FACS	Fluorescence-activated cell sorting
FE-SEM	Field Emission - Scanning Electron Microscopy
FITC	Fluorescein isothiocyanate
FITC -HA-BGHA	Bioactive glass -hyaluronic composites covalently bound to fluorescein isothiocyanate tagged hyaluronic acid
FITC-BGHA	Fluorescein isothiocyanate tagged bioactive glass
FITC-HA	Fluorescein isothiocyanate tagged hyaluronic acid
FTIR	Fourier-Transform Infrared Spectroscopy
HA	Hyaluronic acid
HaCaT	Human Epidermal Keratinocyte line
HBGNP	Hollow bioactive glass nanocomposite
HBSS	Hank's Balanced Salt solution
HCA	Hydroxy carbonate apatite
HMW	High molecular weight
JCPDS	Joint Committee on Powder Diffraction Standard
kDa	kilo Dalton
MDa	Mega-Dalton
MTT	3-(4,5-dimethylthiazol-2-yl)-2,5-diphenyl-2H-tetrazolium bromide
N_2	Nitrogen
Na^+	Sodium ion
NaAc	Sodium Acetate

NBO	Non-Bonding Oxygen
NCCS	National Centre for Communication Security
NHS	N-Hydroxysuccinimide
O.D.	Optical Density
P123	Pluronic 123
PBS	Phosphate buffer saline
PEG	poly(ethylene glycol)
PFA	Paraformaldehyde
PO_4^{3-}	Phosphate ion
RPM	Revolutions Per Minute
RT	Room Temperature
SBF	Simulated Body Fluid
SC	Stratum corneum
TEM	Transmission Electron Microscopy
Template-free BG	Bioactive glass prepared without any template
TEOS	Tetraethyl Orthosilicate
TEP	Triethyl phosphate
TGA	Thermogravimetric analysis
TRIZMA	tris(hydroxymethyl)aminomethane
U2OS	Human Bone Osteosarcoma Epithelial Cells
UV	Ultra-violet
XRD	X-Ray Diffraction

CHAPTER 1

INTRODUCTION

1.1 History of bioactive glass: Bioglass®, a bone replacement material composed mainly of four components was developed almost 54 years ago by Prof. Larry Hench in 1969[1]. The discovery of Bioglass® which has now given rise to an entirely new class of ceramic biomaterial termed as 'bioactive glass', has its own journey. Bioglass® was a landmark invention during a time when the development of biomaterials was solely based on bio-inertness. Termed as the first generation of biomaterials, these implants aimed to provide mechanical support and reduce scar formation without inciting any adverse immune reactions. Bioglass® was a wonder material during those times as it ushered in the development of second-generation biomaterials which apart from providing mechanical support and reducing scar formation, would not be completely bio-inert in a positive way[1]. Instead, it would initiate interfacial bonding with host tissue without initiating any adverse immune reactions[2]. This binding with host tissue brought about a landmark change in the perception of the development of biomaterials as it was observed that such binding properties complemented the process of repair and regeneration greatly, thus establishing the era of the development of the second generation of biomaterials. Later, multiple properties of Bioglass® were discovered where it was observed that it could further elicit multiple gene activations in its implant site which provided cues for repair and regeneration[3]. These discoveries suggested Bioglass® to also be considered as a third-generation biomaterial which, by then, had already established itself as a leading biomaterial across the globe[4].

Prior to the development of SiO_2-CaO-Na_2O-P_2O_5 Bioglass®, most material implants were either plastic or metallic in nature and were rejected by the body[1]. There was a massive room for the development of materials that would not be rejected by the body. Bioactive glass bridged

this gap through the formation of a 'living bond' at its site of implantation in the human body. Prior to this, most metal or plastic implants would lead to the formation of scar tissue in the interface between itself and the host tissue. The hypothesis that a biomaterial should have a somewhat similar composition to that of native tissue was the foundation for the development of Bioglass®[1]. Prof. Larry Hench discovered the composition of 45% SiO_2-24.5% Na_2O-24.5% CaO-6% P_2O_5 and observed that the material could deposit a hydroxyapatite layer in biological fluids[5,6]. This deposition of hydroxyapatite that was observed was the fundamental reason for the superior bone bonding properties exhibited by the material. The formation of hydroxyapatite in the interface between Bioglass® and bone is what leads to the impressive bone-binding property exhibited by the material[7]. The formation of hydroxyapatite is a result of a sequence of chemical reactions occurring at the surface of Bioglass® when in contact with biological fluids[8–10].

Some of the reactions in this sequence are as follows:

1. Exchange of cations (Na^+ or Ca^{2+}) from the glass surface with the H^+ or H_3O^+ from the surrounding body fluid giving rise to Si-OH bonds
2. Rupture of the silica network of the bioactive glass (Si-O-Si) and simultaneous formation of Si-OH in the interface between bioactive glass and the surrounding solution
3. The formed Si-OH condenses and repolymerizes to form a SiO_2 layer.
4. These SiO_2 provide the site for the deposition of Ca^{2+} and PO_4^{3-} migrating from the surrounding solution thus forming a CaO-P_2O_5 film on top of the SiO_2 film.
5. This film then undergoes crystallization in the presence of OH^- and CO_3^{2-} anions migrating to the CaO-P_2O_5 film leading to the formation of hydroxyl carbonate apatite on the surface of the bioactive glass
6. The formation of this hydroxy carbonate apatite layer is mainly observed in the interface of the bioactive glass and the surrounding body fluid.

The evolution of Bioglass® to 'bioactive glass' began with intense research on the constituents of Bioglass® , where both the ratio of the compositions was varied and new components were introduced.

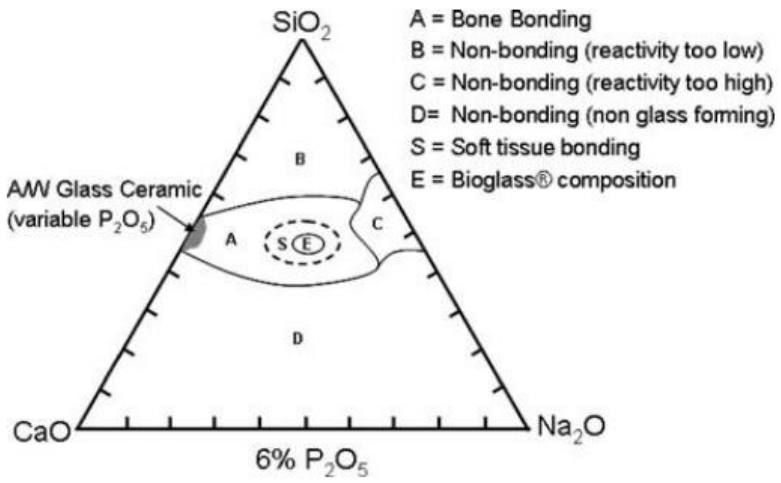

Figure 1.1: Compositional diagram for bone-bonding for bioactive glass preparation developed by Prof. Larry Hench[1]. Highest bone binding can be observed in region S which constitute the trademark 45S5 Bioglass®

When discussing the composition of bioactive glass, it is important to note that a weight percentage of 75% SiO_2 along with 6 % P_2O_5 exhibits the best bone binding ability[1,8,11]. Anything lower than 60 % SiO_2 is usually bi-inert and seldom exhibit bone binding properties[1,12,13]. While early studies focused on understanding the bone binding properties, a study by June Wilson in 1981 demonstrated that Bioglass® can also bind to soft connective tissue while establishing the systemic safety of particulate form of Bioglass®[14]. Once safety trials of Bioglass® were conducted and regulatory approvals were obtained, it was trademarked by the University of Florida for commercial use distinguishing the composition of 45S5 Bioglass® from other bioactive glass compositions and glass-ceramic products. Among the clinical products constituting Bioglass®, middle ear bone implants (DOUEK MED®) in 1985[15] and dental implants (ERMI®) in 1988 are the oldest and most popular. Although there are numerous bioactive glass-based clinical products that are currently under development for

various applications, the limited mechanical strength of bioactive glass largely prevents its use as a load-bearing device. This limits the utility of bioactive glass as a bone implant.

With the development of the third generation biomaterials, it was observed that molecular modifications to bioactive glass composites could enhance interaction with cells and can influence proliferation, differentiation, organization, and production of extracellular matrix [11]. This was made possible through the interaction of the bioactive glass composites with cell-integrins, cell membrane etc. In addition to providing mechanical support and tissue binding ability, the process of tissue repair and regeneration could also be modulated through modification of cellular growth, proliferation, migration, differentiation and remodeling cascades through the dissolution products from bioactive glass. Some examples of third-generation bioactive glass products include NovaThera, Novabone® (PerioGlass®) and NovaMin[16]. These developments have led to the application of bioactive glass as both bulk bioactive glass materials (as scaffolds, implants) and particulate forms (powders, micro- or nanoparticles or composites etc.). The global market for bioglass based materials is expected to grow from USD 172.5 million in 2021 to USD 214.1 million in 2026, with a CAGR of 7.5% during the forecast period. It is expected that India, which is part of Asia Pacific will witness the highest CAGR due to applications in dental, cosmetic, and biomedical fields. In India, companies like SynThera Biomedical are involved in synthesis of tailored bioactive glass based products like bone graft substitutes and non-sensitizing dental creams and toothpastes.

The rate of dissolution of products of bioactive glass is a critical factor in eliciting their biological effects. These biological effects are gene activations or upregulations induced by the dissolution products (Si, Ca, P etc.) which result in higher expression of genes involved in function like growth factor production and activation. These gene upregulation events along with interfacial interactions of collagen and hydroxyl carbonate apatite helps in accelerated repair and regeneration of wound sites, especially in case of bone tissue injury.

1.2 Synthesis of bioactive glass: Early bioactive glass materials were primarily synthesized through high temperature melting, where the glass phase was melted at very high temperatures and cast into bulk sized shapes[17–19]. These would serve as implants or scaffolds. These methods required significant energy and manpower. Also, it was hardly possible to synthesize bioactive glass composites with organic molecules through this method due to the extreme synthesis conditions.

1.3 Sol-gel method for synthesis of bioactive glass: An important milestone was achieved in 1991 when the sol-gel method was successfully applied to synthesize bioactive glass[20]. The 55S bioactive glass compositions were successfully synthesized using the sol-gel method, and they demonstrated better bioactivity than the traditional melt-derived 45S5 Bioglass® [20]. The sol-gel method opened up possibilities for generating bioactive glasses that belonged to the third-generation biomaterials. Also, two-component bioactive glasses (SiO_2-CaO) and quaternary bioactive glass compositions were developed through this method which were proven to be equally bioactive in nature. Additionally, new components such as silver [21], titanium [22], copper [23], and boron [24] were incorporated into the bioactive glass network through the sol-gel route. Among these, silver containing sol-gel derived bioactive glass demonstrated interesting anti-microbial properties [21]. The sol-gel method synthesis did not require high temperature for synthesis when compared to traditional melt-quenching methods. Furthermore, sol-gel method allowed for synthesis of particles with a range of sizes and morphology [25]. It also allowed for post-synthesis functionalization of the bioactive glass particles through interaction with surface Si-OH groups. Due to these advantages, the sol-gel method became immensely popular for the synthesis of bioactive glasses when compared to traditional melt-quenching methods.

The sol-gel technique involves the controlled hydrolysis and condensation of precursors of bioactive glass [20,26]. The primary precursor of bioactive glass is tetraethyl orthosilicate (TEOS),

which is the precursor of SiO_2. Other precursors include triethyl phosphate (TEP) for phosphate, sodium nitrate for Na^+ and calcium nitrate for Ca^{2+}. Water or ethanol is generally used as solvents in most sol-gel techniques, and the process usually takes place in acidic or basic conditions [25]. To synthesize bioactive glass nanoparticles through traditional sol-gel techniques, TEOS is added first to the reaction mixture which generally contains a catalyst. This leads to the controlled hydrolysis and condensation of TEOS, resulting in the formation of SiO_2 nanoparticles. The addition of TEP or other precursors during the course of the reaction leads to the incorporation of the components in the matrix which after drying and calcination, leads to the formation of BG nanoparticles [25]. The introduction of structure-forming agents in the sol-gel technique allows for the formation of complex bioactive glass structures and paves the way for the synthesis of hollow or mesoporous nanoparticles.

Bioactive glass nanoparticles have a wide range of biomedical applications, particularly in drug delivery due to their size, large surface area, and mesoporous nature [25,27]. They also allow for the incorporation of BGs in polymer matrices, providing the opportunity to form a variety of composites. Although bioactive glass nanoparticles can also be obtained through the milling of melt-derived bulk bioactive glass, controlling the of size and morphology is challenging as it is a top-down approach compared to the bottom-up approach of the sol-gel technique [25]. However, some limitations of sol-gel techniques include particle size which is generally in the sub-micron scale, and a high tendency to agglomerate in the formed BG nanoparticles, leading to the formation of larger clusters of BG [25].

1.4 Stober's synthesis of bioactive glass: A modification of the sol-gel method is the Stober's method [28,29]. Stober's method is a form of base-catalyzed sol-gel reaction and can be used for the synthesis of BG nanoparticles [25]. In Stober's method, the precursors of bioactive glass are added to an ethanol solution mixed with ammonium hydroxide, which acts as a catalyst.

Ethanol is important for initiating the hydrolysis of TEOS [25,28]. The Stober's method allows metallic ions to be incorporated into the formed BG. By properly controlling the addition of metal ion precursors, molar ratios of TEOS, process parameters like pH, and reaction time, the properties of BG nanoparticles can be controlled. Further addition of organic species for modulating the shape of the BG nanoparticles can be carried out through the Stober's synthesis. Synthetic surfactants like CTAB are generally used in Sober's synthesis of BG nanoparticles as pore- forming agents [30]. The post -synthesis removal of CTAB leads to the formation of a porous shell of the BG nanoparticles. Apart from Stober's method, there are other sol-gel methods for BG nanoparticle synthesis, such as acid/base co-catalyzed method, post-modification method, micro-emulsion assisted method, aerosol-assisted method etc. [25]. Apart from soft templates like CTAB or P123, hard templates can also be used for synthesis of BG nanoparticles [31].

Although Stober's method is the most popular method for synthesizing silica and bioactive glass nanoparticles, there are multiple disadvantages associated with it. These include the use of non-green solvents like ethanol, catalysts like ammonium hydroxide, synthetic surfactants, and high-temperature calcination. These factors make it difficult to synthesize nanocomposites of bioactive glass with biological molecules, as most biological molecules are sensitive to non-green solvents and thermal stress during calcination. Additionally, in case of sol-gel and Stober's method, removal of surfactant is essential to generate mesoporous shell of BG. As such, when a biological molecule or drug is used in a traditional Stober's method as structure directing agent, it will have to be removed for generation of porosity in the formed BG. As a result, the only option is to load the biomolecule or drug onto the BG nanoparticles in an additional post-synthesis step where they can be loaded on the surface through ionic or covalent interactions with surface silanol groups or accommodated in the pores of the BG nanoparticles.

1.5 Bio-inspired route for synthesis of bioactive glass: A different route for synthesizing inorganic nanoparticles with the help of organic substrates is the bio-inspired route for synthesis [32–34]. As the name suggests, this route is inspired by various inorganic depositions observed in nature, particularly in crustaceans, where the deposition of inorganic silica or calcium can be observed as shells [35,36]. The bio-inspired route has been explored for the synthesis of various nanoparticles using multiple biological molecules [32–34]. In our lab, we have explored the bio-inspired route for the synthesis of bioactive glass for years through use of different templates such as CT-DNA, cellulose, gelatin, L-Lysine, plant extract (Trigonella foenum-graecum), peptide hydrogels, etc. [37–41]. All reactions have been carried out in the complete absence of non-green solvents and high temperature calcination. Particles obtained have been in the nano-size range and well-dispersed is solution. Further, retention of the template has been observed in most formed bioactive glasses [37,38,41]. Based on these observations, the salient features of the bio-inspired route can be outlines as follows:

1) The reaction is inspired by nature, particularly marine organisms called diatoms where elaborate depositions of silica are observed in a variety of complex but beautiful patterns.
2) Such controlled deposition of inorganic silica occurs on organic substrates like proteins or silica deposition vesicles (SDVs) in diatoms.
3) In the bio-inspired route, deposition of silica occurs on organic substrates like DNA, amino acids, proteins, carbohydrates, glycosaminoglycans (GAGs), etc. in the presence of TRIZMA buffer (Tris buffer), which slightly mimics the marine environment.
4) By consecutively adding precursors of bioactive glass (TEOS, TEP, NaAc, and CaAc) at fixed time intervals to Tris buffer (pH 7-8.5) in the presence of organic substrates, it is possible to generate bioactive glass nanoparticles in a very short time.

5) The organic substrate acts as the template for the synthesis of the bioactive glass nanoparticles in a short time. Without the substrates, the particles take longer time to form and are predominantly rich in calcium and do not have enough silica network formation. Additionally, most of the particles generated in the absence of organic substrates are crystalline in nature and do not have bioactive properties. Hence, the organic substrates added during the formation of bioactive glass in the bioinspired route are referred to as soft templates in our studies.
6) Our choice of soft templates is mostly known bio-molecules. We have observed that the properties of formed bioactive glass to vary based on the properties of the template we use.
7) The obtained particles are mostly in the nano-range, well-dispersed, and amorphous in nature.
8) Furthermore, they are inherently mesoporous and do not require the removal of the organic substrate retained in the particle at the end of the reaction.
9) This is a significant development as it allows for the use of medically relevant molecules as templates for bioactive glass synthesis. Without organic solvents, nitrates for metal ion precursors, and high-temperature calcination, it is possible to conserve the template in the bioactive glass nanoparticles.
10) In this way, the bio-inspired method allows for the formation of nanocomposites of bioactive glass in a one-pot reaction that can be used for a range of applications depending on the template used.

In this thesis, we have explored different biologically relevant templates such as gelatin-CCNP, doxorubicin, and hyaluronic acid, as templates for the production of bioactive glass nanocomposites. All of these syntheses were carried out using the bio-inspired route. The selection of these templates was based on their ability to interact with TEOS, resulting in

the production of bioactive nanocomposites of BG and the respective template. All synthesized nanocomposites are amorphous and biocompatible in nature.

1.6 Based on these studies, the **objectives of the thesis** can be summarized as follows:

1) To explore the bio-inspired route for synthesizing bioactive glass nanocomposites using templates other than traditional surfactants.
2) To conduct size, surface charge, and morphological investigations of the formed nanocomposites as well as comprehensive physico-chemical characterizations.
3) To evaluate the bioactivity of the formed bioactive glass nanocomposites
4) To study the *in-vitro* cyto-compatibility of the formed bioactive glass nanocomposites with bone and skin cell lines
5) To assess the properties of the formed bioactive glasses based on the template used such as the efficacy of DOX-BG in anti-cancer treatment and the permeability of BGHA across biological barriers like intra- and inter-cellular membrane and artificial skin membrane.

1.7 Contents of the thesis:

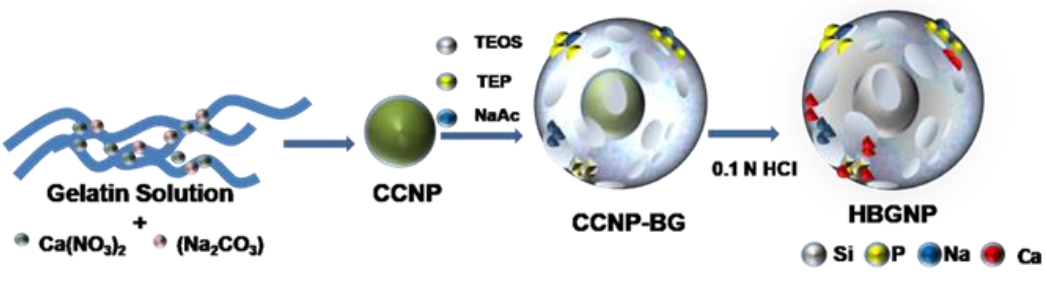

Figure 1.2: Bio-inspired route for synthesis of bioactive glass nanoparticles is an inexpensive and environment friendly method

In the first study, we utilized the bio-inspired route for synthesis of gelatin-calcium carbonate nanocomposites. These nanocomposites were then used as templates for the synthesis of bioactive glass nanocomposites in a similar bio-inspired method. With mild acid treatment to

the CCNP-BG nanocomposite formed in this step, the template CCNP could be etched out. The calcium ions released as a result of the etching of the template CCNP becomes entrapped in the bioactive glass network. This entrapped calcium acts as a source of calcium, eliminating the requirement of additional precursor of calcium such as those used in sol-gel or traditional bio-inspired route for synthesis of bioactive glass. We have presented the detailed mechanism of the synthesis and physico-chemical characterization of the same in chapter 2 of this thesis. Furthermore, the bioactivity of the hollow bioactive glass nanoparticles formed in this study was evaluated in the presence of Simulated Body Fluid (SBF). Additionally, the cyto-compatibility of these hollow bioactive glass nanoparticles towards bone cells was assessed. The objective of this study is to develop hollow bioactive glass nanoparticles using a bio-inspired route, with the intention with the intention of utilizing them as targeted drug delivery devices for bone-related treatments.

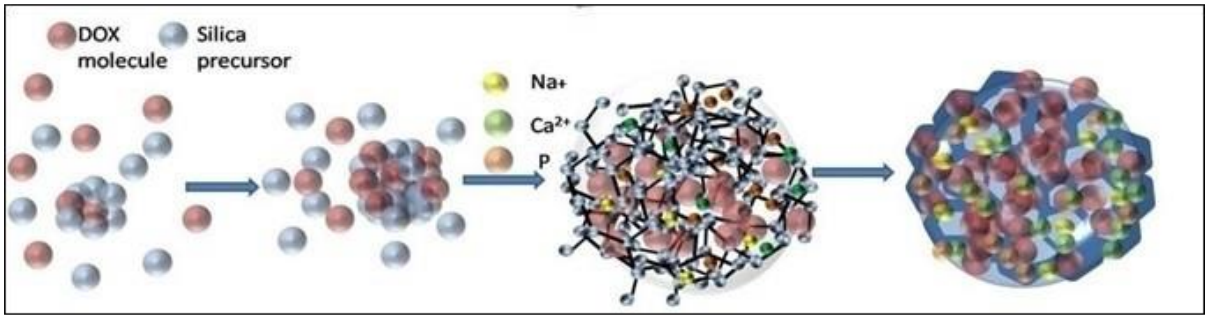

Figure 1.3: One-pot synthesis of doxorubicin- bioactive glass ceramic nanoparticles (DOX-BG) through the bioinspired route.

In the second study presented in chapter 3, we have utilized the common anti-cancer drug, doxorubicin (DOX), as a template for synthesizing bioactive glass-doxorubicin nanocomposites. The drug, DOX served as both a template for directing the synthesis of the nanocomposite and as cargo for delivery. By employing mild reaction conditions, using a biologically favorable buffer like TRIZMA, and avoiding calcination, we were able to preserve the drug within the final bioactive glass nanoparticles. The reaction conditions allowed the drug

to maintain its structure and effectiveness as an anticancer agent was significantly enhanced due to its nano formulation. The study is unique because the drug itself acts as a structure directing agent in the formation of the bioactive glass nanocomposite, while also serving as the cargo for bone cancer related treatments. Besides, size, surface charge and morphology, multiple physico-chemical characterizations of the formed DOX-BG nanocomposites have been carried out and the results have been presented in chapter 3. The bioactivity of the DOX-BG nanocomposites have also been evaluated in addition to controlled drug release properties. Additionally, we compared the effectiveness of the drug on both cancerous and normal cell lines in its free form versus when its nanocomposite form. We observed that as the concentration of the drug in the reaction mixture increased, the resulting particles had a correspondingly higher drug loading in the nanocomposites.

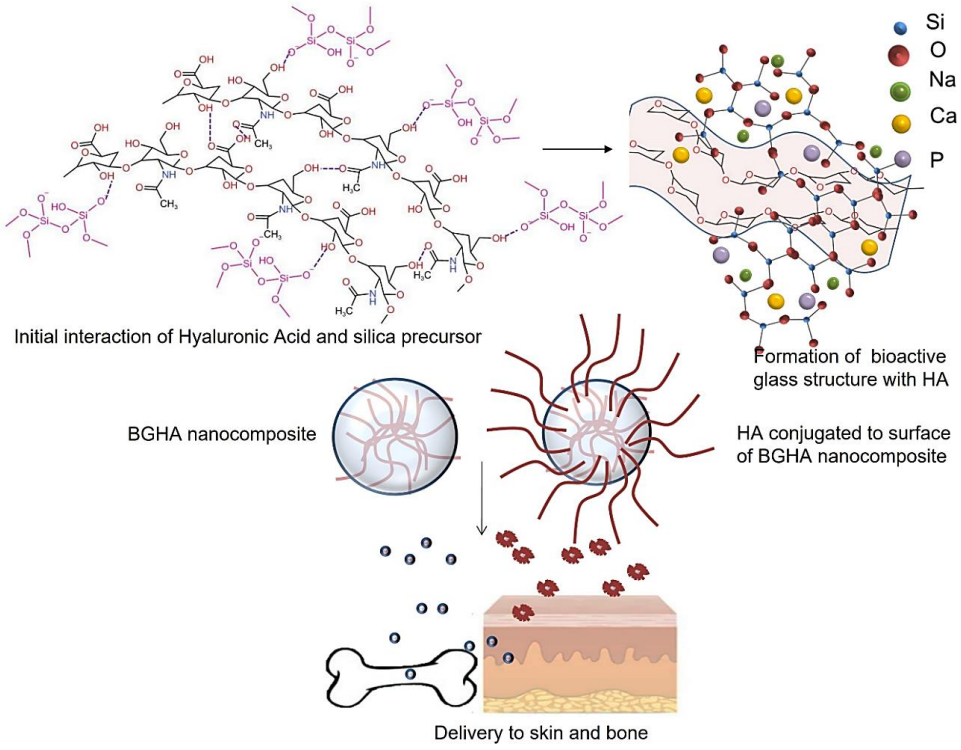

Figure 1.4: One pot synthesis of hyaluronic acid-bioactive glass nanocomposites for non-invasive delivery of HA to skin and bone

In the fourth chapter of the thesis, we synthesized nanocomposites of hyaluronic acid-bioactive glass (BGHA). All morphological and physico-chemical characterization of the nanocomposites along with bioactivity studies have been presented in this chapter. The chapter also contains detailed *in-vitro* cellular studies for studying cyto-compatibility and cellular uptake of the nanocomposites in skin and bone cell lines. Furthermore, transwell-based assays and Franz Diffusion chamber based studies have been presented in this chapter for studying permeation of the nanocomposites across human skin.

Overall, this thesis aims to establish the bio-inspired method as a viable approach for synthesizing bioactive glass nanocomposites using various previously unused templates. We also highlight the potential of using biologically relevant templates as cargo. This opens up opportunities for utilizing novel drugs and biologics as templates for future BG nanocomposite synthesis (provided they can react with TEOS). These studies are currently being actively pursued in our group with successful outcomes.

CHAPTER 2

Bio-inspired Synthesis of Hollow Mesoporous Bioactive Glass Nanoparticles using Calcium Carbonate as Solid Template

2.1 Introduction

Mesoporous and hollow bioactive glass nanoparticles are being currently explored owing to the advantages it provides in terms of higher drug loading capacity, biocompatibility and formation of hydroxyapatite when in presence of biological solutions [42–51] .Due to the latter, it has been considered as a third-generation biomaterial with immense importance in both soft and hard tissue repair and regeneration [27,52,53]. Hollow mesoporous bioactive glass nanoparticles have been formerly synthesized through individual or combination of templates under sol-gel conditions [43–47,49–51]. Previous studies indicate CTAB alone [44,50,51,54]or in combination with block copolymers [46] to be effective template for generating hollow and mesoporous bioactive glass nanospheres. Further, use of co-templates for inducing mesoporous shell has been reported in addition to core-forming template. In a recent study by Bocaccini *et al*, [49] in order to overcome the limitations of soft templates, solid silica spheres have been utilized as hard templates for synthesis of hollow mesoporous bioactive glass. The solid template provides control over size and dispersion to hollow bioactive glass nanoparticles.

We have previously carried out synthesis of mesoporous bioactive glass nanoparticles in presence of structure directing templates like Calf Thymus (CT) DNA [39], gelatin [40], normal and grafted cellulose [38], pectin-collagen composites [55], self-assembling peptides [56] etc. under ambient conditions mostly without involving organic solvents and surfactants. Particles exhibit successful assembling of bioactive glass pre-cursors to form the modified silica network without high temperature calcination while maintaining mesoporous nature. The reaction conditions and precursor concentrations have been optimized for formation of nanosized bioactive glass particles that impart bioactivity when in biological solutions.

In this study, we have utilized bio-inspired route using calcium carbonate as a hard template to direct synthesis of mesoporous hollow bioactive glass nanoparticles. Calcium carbonate has proven to be an excellent hard template in earlier studies for hollow silica nanoparticles [57–60]. Further, calcium carbonate also acts as source of calcium for the bioactive glass thus providing bioactivity. Lastly, as templates, calcium carbonate can be removed with mild acid treatment without significantly hampering the Bioglass® structure and properties.

The obtained shell over the template is mesoporous in nature while removal of the core provided the hollow property. To our knowledge, synthesis of hollow mesoporous particles of bioactive glass without aid of surfactant through the bioinspired route remains to be explored which motivates us to carry out this study.

2.2 Materials and methods:

2.2.1 Materials: Precursors for synthesis of calcium carbonate nanoparticles i.e., calcium nitrate, sodium carbonate and components of TRIZMA buffer solutions were purchased from Sigma. Gelatin, the soft template for synthesizing the $CaCO_3$ Nanoparticles was purchased from LobaChemie, India. Precursors for synthesis of bioactive glass (BG) ceramics like tetraethyl orthosilicate (TEOS), triethyl phosphate (TEP), sodium acetate (NaAc) were procured from Sigma. For bioactivity study, Hank's Balanced Salt solution (simulated body fluid (SBF)) was purchased from Sigma. Human Osteosarcoma cells (U2OS) was purchased from NCCS, Pune. Other components like Dulbecco's modified Eagle's medium of high glucose content (DMEM), 3-(4,5-dimethylthiazol-2-yl)-2,5-diphenyltetrazolium bromide (MTT) were purchased from Sigma. All experimental works and washing steps were carried out with milli-Q water and all other reagents used were of analytical reagent (AR) grade. All experiments were performed in triplicates and averaged for reporting.

Preparation of buffer solutions: Preparation of template and $CaCO_3$-BG core-shell nanoparticles were carried out in 30 mM TRIZMA buffer (pH 8.5) containing 1.82 g/l TRIZMA HCl and 2.22 g/l TRIZMA base dissolved in milli-Q water. All cellular experiments were carried out using PBS solution (pH 7.4) containing 8 g/l of NaCl, 0.2 g/l KCl, 1.44 g/l Na_2HPO_4 and 0.24g/l of KH_2PO_4 dissolved in milli-Q water.

2.2.2 Method

Step 1: Preparation of gelatin template CaCO3 Nanoparticles (CCNP):

Steps involved in preparation of CaCO3 nanoparticles have been discussed in detail elsewhere (Figure 2.3) [61]. Briefly, required volume of calcium nitrate ($Ca(NO_3)_2$) and sodium carbonate (Na_2CO_3) were added sequentially in 10 mM of TRIZMA buffer (pH 8.5) containing 1% gelatin. The amount of $Ca(NO_3)_2$ and Na_2CO_3 were adjusted so as to obtain a final concentration of 10 mM in the TRIZMA buffer solution. After 12 hours or overnight incubation, particles were recovered through centrifugation at 12000 rpm. The particles were washed with pure milli-Q water, dried at 40°C in an air oven and preserved in vacuum desiccator.

Step 2: Deposition of bioactive glass precursors on the CaCO3 nanoparticles prepared in step 1(CCNP-BG):

Bio-inspired synthesis of CCNP-BG was carried out with CCNPs as template like our previously reported procedure with soft templates [38–40,55,62]. CCNP was mixed with 100 ml of TRIZMA buffer solution at pH 8.5 (10 mM) to obtain 1 mg/ml of template concentration. The bioactive glass precursors namely tetraethyl orthosilicate (TEOS) (9.29 g/L), triethyl phosphate (TEP) (1.0 g/L) and sodium acetate (6.36 g/L) were added sequentially into the 100 ml TRIZMA buffer solution containing CCNP. Each precursor was added at 30 minutes' interval and the whole reaction was carried out for 24 hours under constant stirring conditions (500

rpm) at 37°C. After 24 hours, the solution was centrifuged at 12000 rpm, the white precipitate obtained was washed with Milli-Q for removal of unreacted precursors and dried at 40 °C in an air oven and preserved in vacuum desiccator.

Step 3: Dissolving the crystal core to obtain hollow bioactive glass nanoparticles (HBGNP).

The particles obtained in step 2 were treated with 0.1 N HCl to dissolve the core $CaCO_3$ template. Post treatment with HCl for 30 minutes, the particles were washed with milli-Q water until the solution had a neutral pH and the particles were dried at 40 °C in an air oven and stored in vacuum desiccator. Steps followed in the synthesis of HBGNP are illustrated in scheme 1.

2.2.3 Characterization techniques:

Most characterization techniques (size, morphology, state of crystallinity, surface charge, hydrodynamic radius etc.) were carried out for CCNP, CCNP-BG and HBGNP.

X-Ray Diffraction: Powdered X-ray diffraction was performed for particles obtained in all three steps with a RigakuMiniflex-II diffractometer operating at 20 kV and 10 mA using Cu Kα radiation. All three particles (CCNP, CCNP-BG and HBGNP) were scanned at room temperature in the 2Θ range of 10°-70°C at a scan rate of 2°/min.

FTIR: The FTIR spectra of CCNP, CCNP-BG and HBGNP were recorded using NICOLET 380 FTIR spectrophotometer operating in the range of 4000-400 cm^{-1}. Dried samples were mixed thoroughly with potassium bromide (KBr) at 1:100 and pelleted. The IR spectra of the pellets were recorded in the operating range of 400-4000 cm^{-1}.

FE-SEM: The surface morphology of the CCNP, CCNP-BG and HBGNP were visualized through Thermal Field Emission Gun Scanning Electron Microscope (FEI Quanta 200F). Prior

to SEM studies, the samples were coated in gold and subsequently observed at an accelerating voltage of 12 KeV.

Energy dispersive X-ray spectroscopy: Energy dispersive X-ray spectroscopy coupled with SEM (Oxford X-MAX) was used to carry out elemental analysis of all sample types at 20 KeV.

TEM: Morphology of the samples was characterized through Transmission electron microscope (JEOL JEM-1400) with an acceleration voltage of 120 kV. All powdered samples were suspended in methanol and measurement was made post sonication of sample for about 15 min to avoid aggregation in solution.

Nitrogen sorption analysis: The textural properties of the samples were determined using the nitrogen adsorption-desorption analyses at -196°C using a Quantachrome Autosorb-1C TCD analyzer (Model ASICX-TCD6) and with nitrogen as adsorptive gas (N_2, cross sectional area 0.162 nm^2). Prior to analysis, samples were degassed under vacuum at 200 °C for 6 hours. The surface area was determined through Brunauer-Emmett-Teller (BET) equation on the nitrogen absorption data obtained. The pore size distribution was determined by Barret-Joyner-Halenda (BJH) method applied to the desorption branch of the isotherm.

Zeta Potential measurement: Zeta-potential of bioactive glass nanoparticles was monitored at each stage of fabrication in water using ZetasizerNano ZS (Malvern Instruments, UK) instrument. For each sample, measurements were carried out in triplicates and averaged.

2.2.4 Bioactivity assay:

Bioactivity or bone binding ability of the HBGNPs was checked in presence of SBF at 37°C. The composition of SBF is nearly like human blood plasma and bioactive components like bioactive glasses, on immersion in SBF leads to formation of hydroxyl carbonate apatite (HCA) layer on its surface. According to protocol described by Kokubo *et al* [63], samples were

immersed in SBF at a concentration of 1 mg/ml for almost 30 days at 37°C in an ORBITEK shaker incubator (Scigenics Biotech) under sterile condition. The SBF solution was replaced from time to time during the experiment to hinder lowering of cations in the solution as a result of the chemical change of material. Once the experiment was over, the particles were removed from the SBF through centrifugation, washed with deionized water and dried at room temperature. Particles were checked through XRD and FTIR for checking the deposition of hydroxyapatite layer.

2.2.5 Cell studies:

Cyto-compatibility of the HBGNP was checked through toxicity assay on Human Osteoblast-like Osteosarcoma cell line (U2OS). The cell lines were maintained in cell culture incubators with DMEM high glucose media and 10% heat-inactivated fetal bovine serum and 0.1% penicillin/streptomycin at 37°C and 5% CO_2. The cells were seeded in 96 well plates at 104 cells per well and on attaining 60% confluency were treated with different concentrations of the HBGNPs (10 µg/ml to 1 mg/ml) for 24 hours. Post 24 hours, they were subjected to MTT assay. MTT assay depends on cellular mitochondrial activity and measures reduction of tetrazolium component into formazan crystals. The level of reduction of MTT into formazan crystals is an assessment of state of the cellular metabolism and indicates live cells. 10% MTT in Opti-MEM (Invitrogen) was added to each well and incubated for 2 hours at 37°C under cell culture conditions. Post incubation period, the plate was taken out and added with 100 µL DMSO for dissolving the formazan crystal. Once incubated for 30 minutes, absorbance of each well was measured using a TECAN multiplate reader. The cell viability was calculated post normalizations of readings against the control well.

2.3 Results and discussions

In a typical bio-inspired synthesis of bioactive glass nanoparticles, precursors of components of bioactive glass namely tetraethyl orthosilicate (TEOS) (9.29 g/L), triethyl phosphate (TEP) (1.0 g/L), sodium acetate (6.36 g/L) and calcium acetate (4.21 g/L) are added sequentially into 100 ml of 10 mM Tris(hydroxymethyl)aminomethane (TRIZMA) buffer adjusted at pH 8.5 and 37 °C containing organic templates.

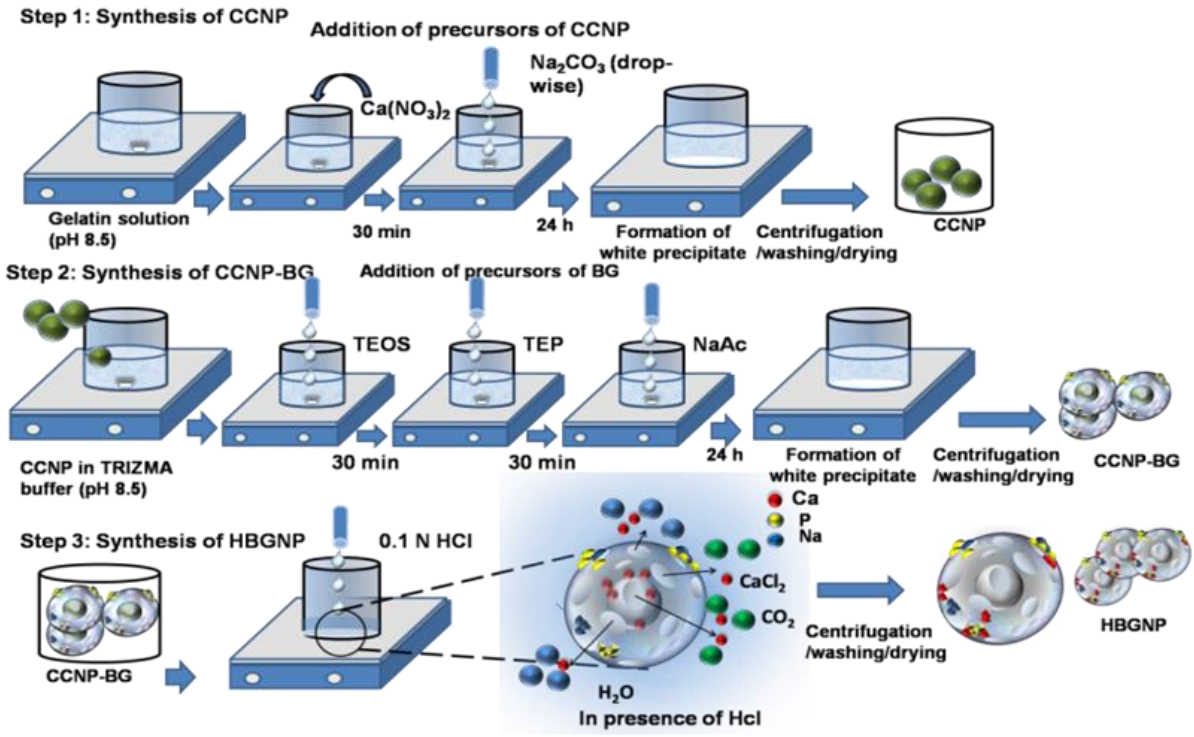

Scheme 2.1: Synthesis of calcium carbonate nanoparticles, CCNP (step 1), core shell CCNP-Bioactive glass nanoparticles, CCNP-BG (step 2) and hollow mesoporous bioactive glass nanoparticles, HBGNP (Step 3). Synthesis scheme of all three kinds of particles involved constant stirring speed at around 500 rpm and equal drip rates.

The precursor concentrations and buffer conditions have been utilized in multiple bio-inspired reactions involving inorganic deposition of bioactive glass [38,39], TiO_2 [32], ZnO [34] on various organic matrix. The slightly basic pH controls hydrolysis and condensation of TEOS, a

common pre-cursor of silica leading to formation of particles obtained through this method mostly below 100 nm [64].

Core shell calcium carbonate-bioactive glass nanoparticles (CCNP-BG) were synthesized through the above-mentioned technique. Here, instead of an organic template, CaCO3 nanoparticles (CCNP) were dispersed in the TRIZMA buffer at a concentration of 0.25 mg/ml and the precursors of bioactive glass were added drop-wise sequentially as shown in scheme 1. On mild treatment of 0.1 N HCl for 30 minutes, most of the CCNP can be removed from the core thus giving rise to hollow bioactive glass particles (HBGNP). It is pertinent to state that the template CCNP has been synthesized in a similar bioinspired synthesis in presence of gelatin as a structure directing template and has been reported recently [61].

2.3.2 Size and morphology of CCNP, CCNP-BG and HBGNP nanoparticles

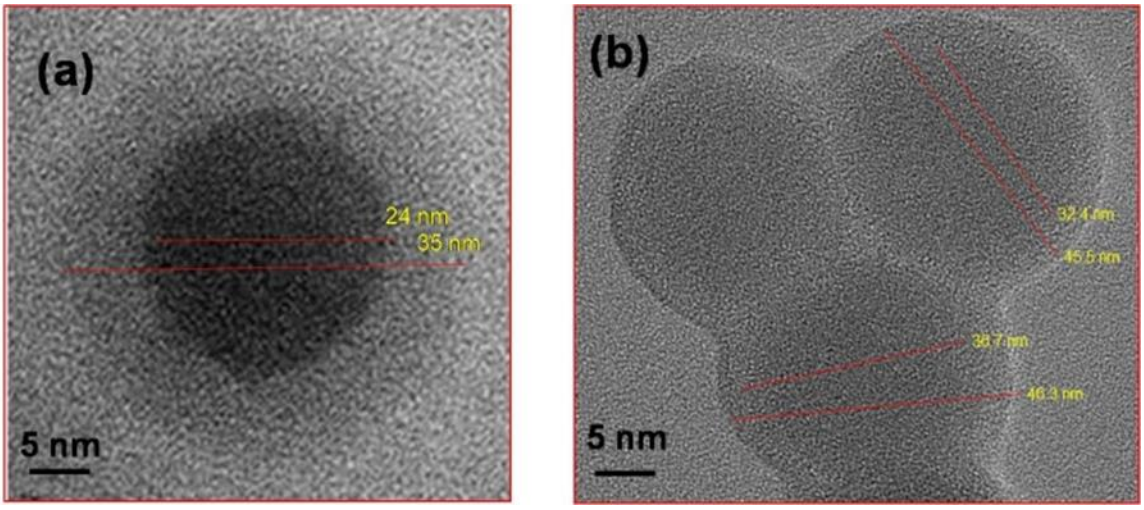

Figure 2.1: HRTEM images of (a) core-shell (CCNP-BG) and (b) hollow mesoporous (HBGNP) bioactive glass nanoparticles. From the representative images, measurements of core and shell have been provided based on calculation through image J bundled with 64-bit Java-1.8.0_172 analysis software for both (a) and (b).

Electron Microscope (HRTEM) micrographs depict the fundamental difference observed in the appearance of core-shell and hollow bioactive glass nanoparticles (Figure 2.1). Further,

comparison of TEM and Energy- Dispersive X-ray Spectroscopy (EDS) based characterization of the template, core-shell and acid etched products has been represented in figure 2.2.

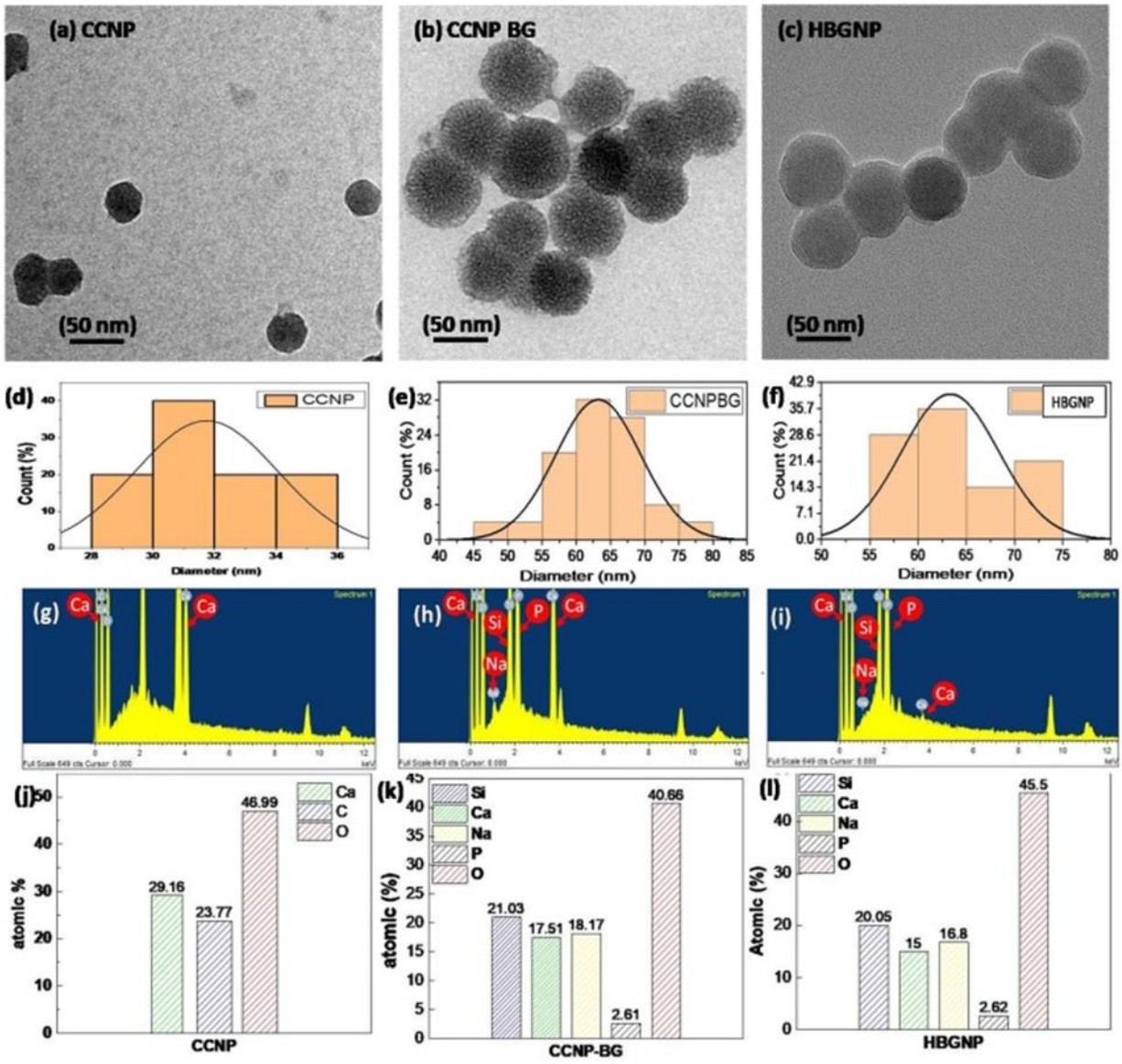

Figure 2.2: (a), (b) and (c) represent TEM images; (d), (e) and (f) represent particle sizes analyzed based on TEM images using image J bundled with 64-bit Java- 1.8.0_172 analysis software. (g), (h) and (i) represent EDS graphs for CCNP, CCNP-BG and HBGNP

CCNP nanoparticles have an average size of 30 nm (Figure 2.2 (a)). The size increases for CCNP-BG and HBGNPs (~30–60 nm) (Figure 2 (b and c)). The change in morphology of the HBGNP nanoparticles can be observed from the TEM micrograph. EDS mapping of CCNP shows peaks corresponding to Ca, C and O depicting its composition (Figure 2.22 (g)). EDS

mapping of CCNP-BG shows emergence of Si, P, Na in addition to Ca and O thus representing formation of bioactive glass assemblies around the CCNP template (Figure 2.2 (h)). For HBGNP, other than Si, P and Na (Figure 2.2 (i)), the presence of O may account for non-bridging O present on the surface of the bioactive glass nano-assemblies and CaO. Presence of Ca depicts that following dissolution of CaCO3 template, Ca^{2+} may have entrapped into the silica framework of the bioactive glass shell. Figure 2.2 (j), (k) and (l) represent bar charts of corresponding atomic percentages of components of template, core-shell and hollow mesoporous bioactive glass nanoparticles based on EDS analysis.

2.3.3 Physico-chemical characterization of CCNP. CCNP-BG and HBGNP

FTIR: Fourier Transform Infrared Spectroscopy (FTIR) spectra (Figure 2.3(a)) of CCNP reveals characteristic peaks of CCNP at 1390 cm^{-1} corresponding to symmetrical $-COO^-$ stretching of carbonate ions along with peaks at 872 cm^{-1} and 713 cm^{-1} corresponding to ν2 and ν3 CO_3^{2-} absorption bands of calcite.

The peaks are like that reported by Meenakshi *et al* [61] for gelatin templated CCNP thus confirming the present observation. Further, the mechanism involved in formation of CCNP has been discussed in Figure 2.3, Supplementary information. For CCNP-BG, it was observed that the peaks of CCNP were retained. The presence of new peaks at 1074 cm^{-1} and 966 cm^{-1} corresponds to Si-O-Si asymmetric stretching and bending vibrations respectively [39]. The peak at 966 cm^{-1} corresponds to Si-OH stretching vibration [65]. An additional peak at 798 cm^{-1} corresponding to characteristic ring structure of the silicate network can also be observed in the CCNP-BGFTIR spectra. All peaks other than those corresponding to template CCNP in the CCNP-BG samples have been reported in context of bioactive glass in previous studies [38,39,62]. For the HBGNP sample, the removal of the CCNP template through hydrolysis can be confirmed from its FTIR spectra. While the CCNP FTIR peaks (1390 cm^{-1}, 872 cm^{-1} and 713

cm^{-1}) were seen to be missing, the peaks corresponding to the BGNP could be observed (~1080 cm^{-1}, 970 cm^{-1}, 790 cm^{-1}) with slight shifts indicating retention of the bioactive glass network. The Si-OH group corresponding to 966 cm^{-1} is responsible largely for the apatite forming ability observed in case of the bioactive glass samples[39].

XRD: X-ray diffraction (XRD) patterns depict characteristics diffracting domains for CCNP at 29.44°, 36.03°, 39.48°, 43.24°, 47.62°, 48.61° and could be assigned as (012), (411), (113), (202), (018), (116) respectively (Figure 2.3(b)). These diffracting domains were consistent with the standard pattern JCPDS no. 01–085-1108 which corresponds to $CaCO_3$ with rhombohedral crystal system. The XRD graph of CCNP-BG showed retention of $CaCO_3$ diffracting domains indicating presence of the template in the CCNP-BG nanoassemblies. For HBGNPs, no diffraction could be detected other than a broad hump (15–30 degree) indicating the BG assembly is amorphous in nature. The mean crystalline size of CCNP and CCNP-BG could be calculated as 15 nm and 28.6 nm as per the Debye-Scherer equation,

$$D = K\lambda/\beta Cos\theta$$

Where K=0.9 for Cu-Kα, λ=wavelength (0.15406 nm), β= full width of half maximum (FWHM) and θ= diffraction angle.

Surface charge and thermal stability: Apart from this, surface charge and thermal stability of the template, core-shell and hollow bioactive glass nanoparticles was checked through zeta potential (Figure 2.3c) and thermogravimetric analysis (Figure 2.3d) respectively. The surface charge of the particles was calculated through the zetasizer instrument. While CCNPs were recorded to have an average zeta potential to be -21.9 mV, CCNP-BG and HBGNP recorded -37.3 mV and -16.8 mV respectively as their average zeta potentials. All compounds were recorded for their zeta potential at pH 7. The charge of CCNP is same as that reported by

Meenakshi *et al* for gelatin templated CCNPs [61]. Bioactive glass nanoparticles have been previously reported to possess negative zeta potential of in water (pH 7) [62].

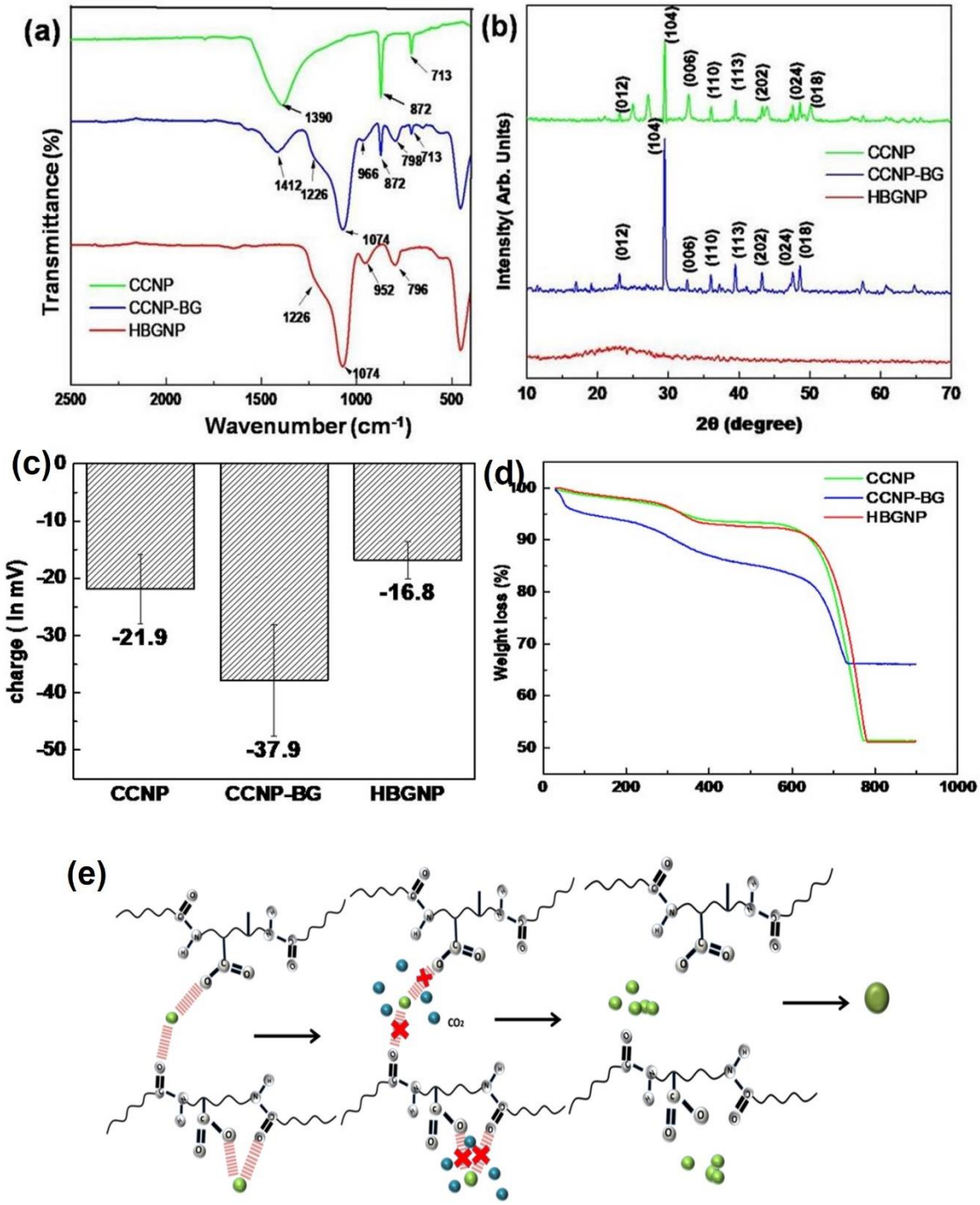

Figure 2.3: a) FTIR and b) XRD of all three samples (CCNP, CCNP-BG and HBGNP); c) Zeta potential measurement and d) Thermogravimetric analysis of the template (CCNP), core-shell (CCNP-BG) and

hollow bioactive glass nanoparticles (HBGNP); e) Mechanism of gelatin templated bio-inspired synthesis of CCNP.

In our case, the zeta potential obtained was more negative for CCNP-BG probably because of presence of the template CaCO3 and non-bonding oxygen atoms present in normal BG surface role of charge in monodispersity [66]. The addition of HCl leads to removal of such non-bridging Oxygen as well as surface SiO^- ions which may have led to decrease in negative charge from the surface of HBGNP when compared to CCNP-BG. Compiled TGA thermograms (Figure 2.3d) reveal that first decomposition of CCNP could be observed at approx. 330 °C and ended at 760 °C with almost 50% weight loss. The observation is similar to the CCNP TGA thermogram by *Meenakshi et al.* suggesting decomposition of CaCO3 to calcium oxide and escaping of CO_2 [61] . For HBGNP, a similar curve could be observed with almost 50% weight loss at 760 °C. The observation recorded for CCNP-BG was however different as only 30% weight loss could be recorded. While the first decomposition was observed below 100°C, possibly due to water loss, the extent of weight loss was lower than CCNP and HBGNP even at higher temperatures. However, the comparatively initial rapid rate of degradation of CCNP-BG can be due to the presence of the bioactive glass network, condensation of terminal silanol groups and phase transformation of amorphous silica to quartz [67].

A graphical representation of the mechanisms involved in synthesis of the HBGNPs has been presented in figure 2.3e. The graphical representation demonstrates formation of CCNPs from gelatin at pH 8.5. The mechanism is similar to deposition of inorganic groups on organic substrates as observed in crustaceans and mollusks especially in marine environment. Gelatin is involved in synthesis of the CCNPs through opening up multiple nucleation sites. The precursor of CCNP, $Ca(NO_3)_2$on addition to the gelatin matrix interacts with gelatin matrix in the form of gelatin-$Ca(OH)_2$ which on addition of Na_2CO_3 leads to formation of $CaCO_3$ at the nucleation sites. As shown in the graphical representation, it can be hypothesized that there is

an initial interaction of $Ca(OH)_2$ with the COO^- groups present in the side chain of gelatin matrix which later gets disrupted on availability of CO_2 as a result of addition of the second pre-cursor thus leading to formation of CCNP crystals as observed from the XRD data. The mechanism has been discussed in detail in the study by Meenakshi *et al* [61].

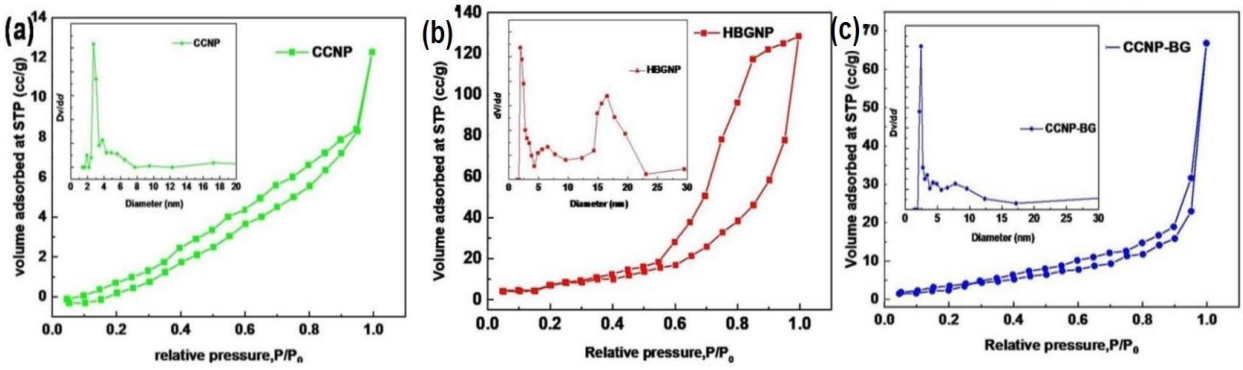

Figure 2.4: Comparison of the nitrogen adsorption-desorption isotherms and respective pore size distribution of CCNP, CCNP-BG and HBGNP nanoparticles. Among the three, HBGNP showed the largest hysteresis loop depicting mesoporous nature.

Nitrogen-adsorption desorption analysis (BET): Nitrogen sorption analysis of CCNP represented Type III isotherm with Hysteresis loop 3, while that of CCNP-BG appeared to be type IV isotherm with H3 loop and HBGNPs represented Type IV isotherm and H3 loop [68] (Figure 2.4). CCNP may comprise of sparsely distributed marginal mesopores which is generally observed due to surface roughness of inorganic materials/crystals grown on organic substrates [32] or in presence of Tris Buffer [69]. Interestingly, CCNP-BG also depicts marginal or narrow mesoporous characteristic with pores mostly in the range of 10 nm. It will be pertinent to remember that the bio-inspired process does not involve calcination as particles is mostly dried at room temperature. As a result of this, the deposited silica may be inherently nanoporous in nature [25]. Earlier studies have reported mesoporous bioactive glass nanoparticles even with retention of template [38,39]. The non-rigid nature of the shell can be inferred from the characteristic H3 isotherm loop [68]. For HBGNPs, the isotherm and the hysteresis loop obtained

(Type IV isotherm and Hysteresis loop 3) is typical of hollow mesoporous bioactive glass nanoparticles observed in earlier studies [44,50,51,54]. Along with this, the bimodal nature of the pore size distribution graph obtained through the Barrett-Joyner-Halenda (BJH) method depicts two sets of mesopores (one centered at 2–5 nm while other pore distribution at 15–25 nm) as has been demonstrated in earlier studies [50,66]. This indicates the presence of a central void along with the inherent mesoporous shell of the bioactive glass. Further, removal of template resulted in almost three-fold increase in surface area for HBGNPS but only marginal increase in average pore diameter. Pore volume increased approx. two-fold indicating the formation of void in HBGNPs (Table 2.1). This indicates that HBGNPs are more mesoporous than CCNPs and CCNP-BGs.

Pore characterization	**CCNP**	**CCNP-BG**	**HBGNP**
BJH surface area (in m^2/g)	17.35	33.93	90.58
Average Pore diameter (in nm)	4.8	26.98	28.82
BJH Cumulative desorption pore volume (in cc/g)	0.026	0.113	0.229

Table 2.1: Surface area and pore characterization of CCNP, CCNP-BG and HBGNP through Brunauer–Emmett–Teller (BET) analysis.

2.3.4 Bioactive property of HBGNP

Bioactive glass biomaterials are known to have bone regenerative nature which makes it different from silica particles. Bioactivity is measured in terms of *in-vitro* biological response at the interface of the bioactive glass and biological fluid (SBF) and is assessed through deposition of hydroxyapatite like bone bonding formation.

The *in-vitro* response is carried out in SBF as per the study by Kokubo *et al* [70]. The formation of hydroxyapatite deposits on surface of HBGNPs immersed for different time periods (7, 15 and 30 days) was checked through XRD, FESEM and FTIR studies (Figure 2.5 (a, b)).

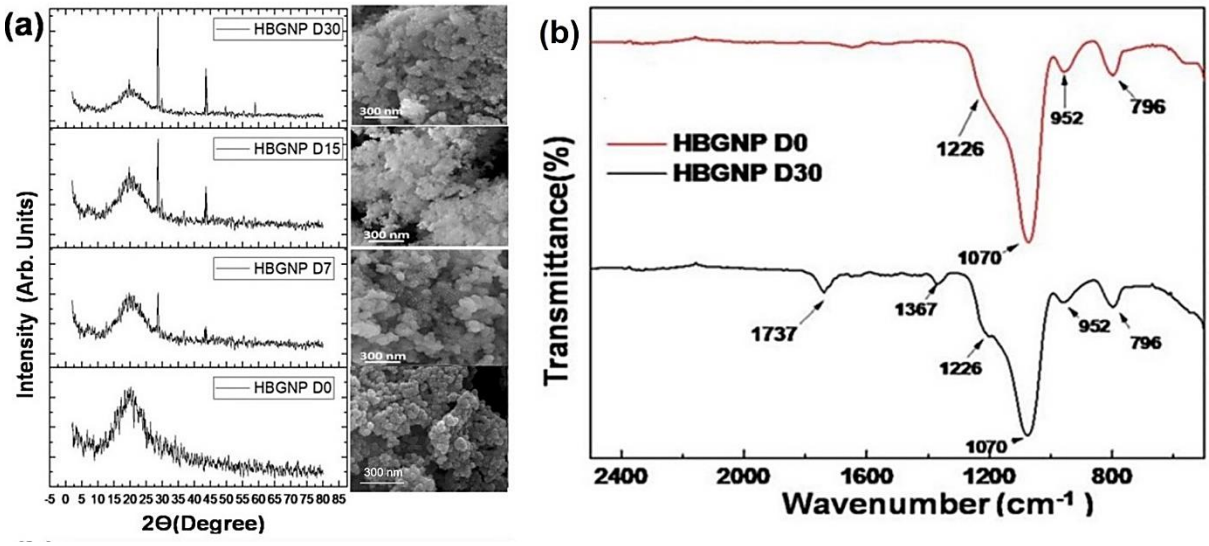

Figure 2.5: (a) FTIR data (b) XRD data spectra for HBGNP before and after immersion in SBF

SEM images reveal that with increase in immersion time, the surface of the bioactive glass nanoparticles became coarser and covered with lath-like apatite crystals. The SEM images for the synthesized HBGNPs were like that reported earlier by Nidhi *et al* [38].With increase in immersion time, the deposition tends to increase (which can also be observed from the XRD data) ultimately leading to layered morphology as observed on Day 15 and 30. In order to understand the nature of the deposition, XRD and FTIR of the immersed sample was carried out (Figure 2.5).

XRD: The XRD graph of HBGNP post incubation in SBF shows characteristic diffracting domains at 22.8° (111), 31.7° (211) and 46.6° (222) along with the broad bump at 2Θ range of 15° to 30° representing a semi-amorphous character of the sample. The diffracting domains agree with JCPDS file no. 01–072-1243 corresponding to $Ca_{10}(PO_4)_6(OH)_2$. The intensity of the peaks mentioned above increase with immersion time indicating higher deposition and growth of hydroxyapatite layer. Similar observations with bioactive glass particles have been recorded in earlier studies [38,62]. When in SBF, the Si-O-Si groups present on the surface of HBGNP undergoes hydrolysis to form $Si\text{-}O^-$ resulting in release of sodium, phosphate, and

calcium ions in solution due to disruption of the silica network. The calcium and phosphate ions may also be attracted to the $Si\text{-}O^-$ ions on the HBGNPs from the surrounding environment in SBF. Such events promote formation of calcium-phosphate complexes which end up getting deposited on the surface of the nanoparticles through ionic interactions thus giving rise to formation of hydroxyapatite crystals which is highly favorable for bone binding activities of the bioactive glass particles.

FTIR: Comparison of FTIR data of HBGNPs immersed in SBF for 30 days with that before immersion revealed new peaks at 1737 cm^{-1} and 1367 cm^{-1} which correspond to C=O stretching and Si=O stretching. The additional peaks may correspond to hydroxyl group deposited in the sample and the carbonate peaks indicating deposition of HCA layer. Further the shoulder of the sharp band corresponding to phosphate group (1228 cm^{-1}) seems to be more prominent indicating probably formation of apatite rich layer.

2.3.5 Mechanism of synthesis

Stober's synthesis mechanism has been reported earlier for hollow silica nanoparticles with $CaCO_3$ as solid template with slight modifications [58,71,72]. TEOS is used as a traditional precursor of silica or bioactive glass based on its ability to readily undergo hydrolysis in aquatic conditions [73]. However, the rate of hydrolysis for TEOS is much slower than other metal alkoxides thus requiring the presence of acid or base catalyst [73]. In our case, TRIZMA buffer (pH 8.5) leads to hydrolysis and condensation of TEOS leading to formation of nanosized clusters around CCNPs. This is a result of initial heterogeneous nucleation of hydrolyzed tetra functional silicon alkoxide network throughout the surface of CCNPs. The interaction between the silica shell and $CaCO_3$ has been proposed to be that of electrostatic in nature based on surface zeta potential [73,74]. The natural affinity of $CaCO_3$ towards deprotonated TEOS in poly(alcohol)amine buffers is due to coordination between Ca^{2+} and CO_3^{2-} ions of CCNPs

which attracts NH_4^+ and OH^- ions on its surface from the external Tris(hydroxymethyl)aminomethane buffer environment (TRIZMA).

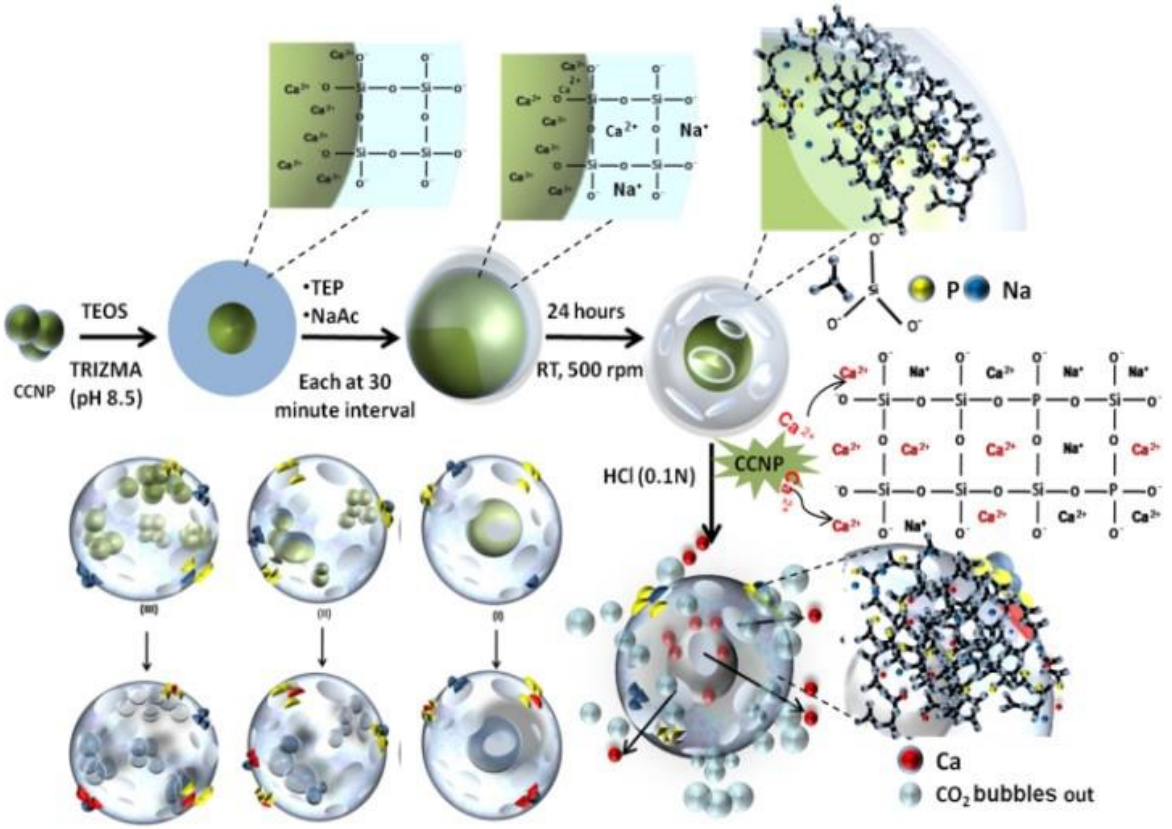

Figure 2.6: Graphical representation of plausible mechanism of formation of CCNP, CCNP-BG and HBGNP

This helps in the initial nucleation reactions which is then followed by growth based on homogenous nucleation. During addition of the other precursors (TEP and NaAc) deposition of the phosphate and sodium ions take place in the silica network leading to formation of bioactive glass. The hydrolysis of TEOS allows reaction with $PO4^{3-}$ (covalent bonding with Si-OH) and Na^+ (ionic interaction with SiO^-) which leads to formation of the BG network. Apart from the formation of core shell architecture (depicted as (I) in Figure 2.6), it is possible that multiple CCNPs (due to their high propensity to rapidly aggregate in solution) may lead to formation of a single CCNP-BG (II and III). Shell thickness also depends on amount of precursor (TEOS) used [67] and particle size is mainly a function of the pH of the solution [64]. In

presence of 0.1 N HCl, the CCNPs get converted to $CaCl_2$ with H_2O and CO_2 which would bubble out of the solution. While the CO_2 escape may result in mesoporous shell assembly, in our case the same could not be confirmed as the BG network around CCNP inherently is mesoporous in nature as observed through BET analysis of CCNP-BG. The obtained Ca^{2+} ions from the reaction get impregnated in the BG network as the addition of HCl may destabilize the silica network temporarily. The surface area of HBGNPs (~90 g/cm^3) and shell thickness (~10 nm) and alkaline synthetic conditions hints towards a Type B hollow architecture [73].

2.3.6 Cyto-compatibility of hollow mesoporous bioactive glass nanoparticles

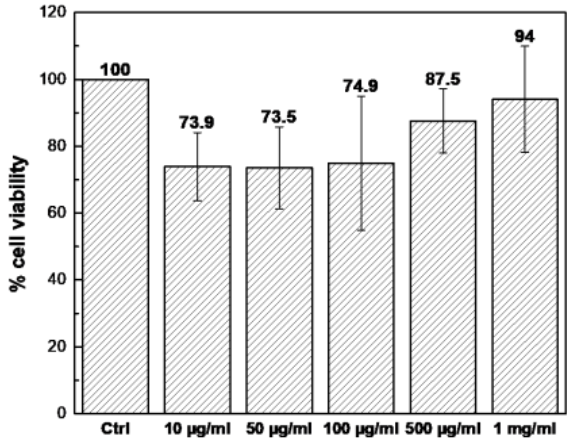

Figure 2.7: MTT assay for HBGNP at increasing concentrations (10 µg/ml to 1 mg/ml)

Since bioactive glasses are predominantly used in case of bone related treatments, we evaluated cytocompatibility (through 3-(4,5-Dimethylthiazol-2-Yl)-2,5-Diphenyltetrazolium Bromide, MTT assay) of the HBGNPs on Human Osteosarcoma cell lines (U2OS) as model bone cell line. After 24 hours of treatment of the particles at different concentrations, MTT assay was performed to assess the presence of live cells (Figure 2.7). Control (ctrl) depicts cells in media without any treatment. The viability obtained from the remaining wells was normalized against this control. At all concentrations, the particles appeared to be biocompatible in nature and had more than 70% of cell viability. At higher concentrations, cellular viability appears to increase slightly but not significantly.

2.4 Conclusion

The current study focuses on exploring the bio-inspired route for preparing hollow BG nanoparticles that could be applied in bone regeneration studies. Using CaCO3 as inorganic template, we synthesized core-shell CCNP-BGs which on mild acid treatment resulted in formation of the final product. Further, avoiding solvent or surfactant use makes the process eco-friendly while allowing future in-situ encapsulation of solvent/pH/temperature sensitive quest molecules during formation of bioactive glass shell. Besides, absence of calcination helps in conservation of heat sensitive cargo retained in the final product. Dissolution of the core retains calcium in the BG network which is essential for its bioactivity. Due to high pore volume and bioactivity, mesoporous HBGNPs can be utilized for various delivery based applications and bone targeted delivery.

CHAPTER 3

One-pot synthesis of Doxorubicin-Bioactive glass-ceramic Hybrid nanoparticles through bio-inspired route for anti-cancer therapy

3.1 Introduction

The advantage of bioactive glass over silica nanoparticles is that the latter provides attractive hydroxyapatite forming property when in contact with blood plasma [75,76]. This promotes binding of bioactive glass nanoparticles to bone tissue thus allowing specificity for site of action. Besides, it suits the theory of 'kill and heal' in cancer where controlled release of anti-cancer drugs like doxorubicin induces killing of cancer cells and the bioactive glass can promote regeneration of the area through inducing healthy bone growth and osteogenic differentiation [77–80]. Although many studies have focused on building doxorubicin loaded bioactive glass nanoparticles [81–90], none attempted a one-pot synthesis process due to limitations of current sol-gel processes to synthesize the same. In fact, bioactive glass in traditional sol-gel methods require high temperature calcinations for incorporation of cations and anions [91,92]. This calcination step which is generally carried out at 600-800°C is counterproductive for one-pot co-condensation reactions involving high-temperature labile drugs and bio-molecules with bioactive glass. As such, the only option is to first synthesize the bioactive glass nanoparticles, carry out high temperature calcination step and then induce external loading with drugs. This external loading can be further facilitated if the bioactive glass nanoparticles are mesoporous in nature as it provides sites for loading and accommodation of drugs and allows prolonged controlled release [88,89,93]. However, induction of mesoporosity in bioactive glass requires usage of surfactants like CTAB, Pluronic® P123, F127, PEG etc. during the synthesis process which is later removed through acid treatment or calcinations for induction of mesoporosity [93–95]. Improper removal of surfactants may lead to unwanted toxicity and is primary concern in this

approach. In our case, the absence of calcination step in the one-pot synthesized hybrid nanoparticles allows retention of the drug which itself acts as template for the synthesis of the nanoparticles and provides controlled drug release like that observed for methods involving drug loading post-synthesis.

From studies involving one-pot synthesis of doxorubicin-silica [96–101] and other classes of nanoparticles [102–104], it can be predicted that functional groups of the drug can react with precursors of bioactive glass. Precursors of bioactive glass like tetraethoxysilanes on getting hydrolyzed to subunits of silicon oxides can react with hydroxyl groups of doxorubicin thus allowing incorporation of the same during different stages of the growth of the nanoparticles. The advantage of one-pot synthesis of drug-nanoparticle hybrid formulations is that it eliminates the requirement of an additional step for drug loading. Further, co-condensing drug with bioactive glass nanoparticles should help in avoiding burst release of the same which is sometimes desirable where controlled and steady release of drugs is required.

To our knowledge, synthesis of DOX-BG ceramic nanoparticles in a one-pot bio-inspired route in absence of surfactant and high temperature calcinations has hitherto been unreported thus motivating us to carry out the same. Further, the particles obtained are mesoporous in nature as the bio-inspired route inherently induces porosity in bioactive glass even in absence of surfactants. This is due to irregularities of the amorphous silicon-oxide structure formed, presence of cations and anions (like Ca^{2+}, Na^{+} and PO_4^{3-}) which act as network inducers and modifiers and presence of organic molecules (DOX in this case) used as template in the bioactive glass-ceramic structure. This mesoporosity can be harvested for secondary loading of other classes of drugs, biomolecules, or specific surface functionalization for active targeting in addition to the drug (DOX in this case) that is already incorporated within bioactive glass-ceramic nanoparticles.

DOX -BG ceramic nanoparticles obtained through this study were stable with sizes in nano-range. Unlike the traditional Stober's method which requires alcoholic solutions and ammonia buffers, the reaction medium of bio-inspired method is a mild Tris(hydroxymethyl)aminomethane buffer (TRIZMA®) that is a common component in protein-based studies in molecular biology and is thus non-degrading for doxorubicin. Effective entrapment of doxorubicin in the bioactive glass ceramic could be observed optically through color change of the formed nanoparticles and was further characterized physico-chemically through techniques like UV-Visible spectroscopy, FTIR, TEM, SEM, TGA, XRD etc. Importantly, the DOX-BG ceramic nanoparticles performed significantly better in terms of killing of osteosarcoma cells when compared to equivalent dosage of free doxorubicin. Further, the extent of killing of osteosarcoma cells was higher when compared to non-cancerous cells.

Prior to this, drug loaded silica xerogels, monoliths, composites which are bioactive in nature have been synthesized through sol-gel methods [105–107]. The studies elaborated the advantages of such systems like low temperature and mild pH conditions for synthesis and informed of porosity in the formed compounds combined with its effect on release of doxorubicin. However, the sizes of many such formulations appeared to be in micrometer range and were established as implant material. Through our method, we could control the sizes of the formed DOX-BG ceramic composites in nanometer range and could further establish properties like traditional mesoporous bioactive glass nanoparticles. The particles exhibited capacity for depositions of hydroxy carbonate apatite (HCA) when in contact with simulated body fluid (SBF) maintained at 37°C in a shaker incubator. With sustained drug release in acidic conditions and bioactivity, the formulation may provide advantages of controlled release of drugs like doxorubicin with narrow therapeutic index at sites of osteosarcoma without premature release when administered locally or systemically.

3.2 Materials and methods

3.2.1 Materials

Doxorubicin hydrochloride was procured from Sigma-Aldrich. The precursors for the bioactive glass synthesis were obtained from Sigma-Aldrich. These include tetraethyl orthosilicate (TEOS), triethyl phosphate (TEP), sodium acetate (NaAc) and calcium acetate (CaAc). In order to study bioactive properties of the DOX-BG formulations, Hank's Balanced Salt Solution (HBSS) was utilized and procured from Sigma-Aldrich. Human Osteosarcoma cells (U2OS) was chosen as model bone cancer cell line while Human keratinocytes (HaCaT) was chosen as model non-cancerous cell line and purchased from National Center for Cell Science (NCCS), Pune. Dulbecco's Modified Eagle Medium (DMEM-F12) was purchased from Sigma-Aldrich and used for U2OS culture. 3-(4,5-dimethylthiazol-2-yl)-2,5- diphenyltetrazolium bromide (MTT), a reagent for cytotoxicity analysis were purchased from Sigma-Aldrich. All experimental works and washing steps were carried out with de-ionized water and all other reagents used were of analytical reagent (AR) grade. All experiments were performed in triplicates and averaged for reporting.

3.2.2 Methods

Preparation of buffer solutions: Tris(hydroxymethyl)aminomethane (TRIZMA® buffer) was used for preparation of the DOX-BG nanoparticles. 30 mM of the buffer was used as the reaction media and contained 1.82 g/l TRIZMA® HCl and 2.22 g/l TRIZMA® base dissolved in Milli-Q water and pH was adjusted to pH 8.5. Autoclaved Phosphate Buffer Saline (PBS) (pH 7.4) was prepared using 8 g/l of NaCl, 0.2 g/l KCl, 1.44 g/l Na_2 HPO_4 and 0.24 g/l of KH_2PO_4 dissolved in de-ionized water and used for cellular experiments. Acidic Buffer was prepared by dissolving 8.4 g of sodium acetate and 3.35 ml of glacial acetic acid in sufficient water to produce 1000 ml of total volume.

Preparation of DOX-BG nanoparticles: In a typical bio-inspired synthesis, various concentrations of template are prepared in presence of TRIZMA® buffer. Post preparation of the TRIZMA® buffer, doxorubicin dissolved in de-ionized water (stock solution-5 mg/ml) was added to TRIZMA® buffer to attain final concentrations of 0.25, 0.50 and 0.75 mg/ml. At these concentrations, the DOX-TRIZMA reaction medium was placed on a magnetic stirrer at 500 rpm and at 37 °C. In majority of reactions, overall reaction volume was maintained at 10 mL Doxorubicin readily dissolved in TRIZMA® buffer and precursors of bioactive glass namely TEOS (464.5 mg), TEP (50 mg), NaAc (210.5 mg) and CaAc (318 mg) were added sequentially into the buffer solution at an interval of 30 minutes from each other. The reaction was carried out in dark for 12 hours and resulting particles were obtained through centrifugation of the reaction solution at 12,000 rpm at room temperature (RT) and washed with de-ionized water multiple times in order to remove un-reacted precursors and drug. The particles were dried in a solid bath incubator at 37°C for 24 hours and stored in sealed micro-centrifuge tubes. The reaction media was retained for assessing drug loading through determination of remnant drug amount by UV-visible spectroscopy.

3.2.3 Characterization techniques

Various techniques have been applied for characterizing the size, surface charge, morphology, porosity etc. of doxorubicin-bioactive-glass hybrid nanoparticles of various template concentrations (0.25 DOX-BG. 0.50 DOX-BG and 0.75 DOX-BG).

In order to characterize the size and morphology of the DOX-BG preparations, particles were dispersed in de-ionized water at a concentration of 0.1 mg/ml and sonicated using a probe sonicator (Sonics, vibra cell) for homogenous distribution.

Particles were checked for size through Dynamic Light Scattering (DLS) and morphology through Transmission Electron Microscopy (TEM) and Scanning Electron Microscopy (FE-SEM).

Dynamic Light Scattering (DLS): DLS was used for measuring the hydrodynamic radius of the formed DOX-BG nanoparticles. Measurements were carried out using a Malvern Zetasizer Nano instrument for all three formulations of DOX-BG. Prepared samples were measured at 25 °C and z-average diameter has been reported for size distribution.

TEM: Transmission electron microscope (Tecnai G2200KV HRTEM SEI HOLLAND) was used for analyzing the size and morphology of the DOX-BG formulations at an acceleration voltage of 200 kV. All DOX-BG formulations were dried and re-dispersed in de-ionized water. Post 15 minutes of sonication, aqueous drops of the formulations were formed on carbon coated copper grids and dried at room temperature before analysis.

FE-SEM: In order to observe the surface morphology of the DOX-BG nano-formulations, Thermal Field Emission Gun Scanning Electron Microscope (FEI Quanta 200F) was utilized. All samples were coated in gold and observed at accelerating voltage of 5 kV.

In order to confirm successful formation and solid-state characteristics of the formed DOX-BG nanoparticles, Fourier Transform infrared Spectroscopy (FTIR) and X-Ray Diffraction (XRD) was carried out.

FTIR: NICOLET 380-FTIR spectrophotometer (4000-400 cm^{-1}) was used for characterizing the bulk structure of DOX-BG nano-formulations. Samples were formed into pellets using dried KBr at 1: 100 ratio before running the same in the operating range of 4000-400 cm^{-1} in transmission mode in the instrument at a resolution of 1 cm^{-1}.

X-Ray Diffraction: In order to characterize the solid state of the formed DOX-BG nanoparticles at various concentrations of doxorubicin, powdered X-Ray Diffraction was carried out through Rigaku Miniflex-II diffractometer operating at 20 kV and 10 mA using Cu Kα radiation. All scans were carried out at room temperature in the 2θ range of 10 °-70 °C at a scan rate of 2°/min. Energy dispersive X-ray spectroscopy (EDS): EDS was coupled with SEM at an operating voltage of 12 KV (ZEISS EVO MA15) for carrying out measurement of elemental composition of the particles. Data was reported for average relative atomic% of Si, P, Ca, Na and C from three representative surfaces.

Thermogravimetric analysis (TGA): Thermal stability of the DOX-BG nanoparticles was investigated through TGA (Perkin Elmer thermogravimetric analyzer). Samples were heated over a range of 25 to 800 °C at a heating rate of 10 °C/min. The analysis was carried out in Nitrogen environment with maintenance of Nitrogen flow rate of 20 ml/min. The change in weight percentage over the treatment period and temperature was reported in the form of graph.

Nitrogen sorption analysis (Brunauer-Emmett-Teller (BET) analysis): BET based nitrogen adsorption and desorption technique was used for evaluation of porosity textural property of the DOX-BG nanoparticles. Nitrogen adsorption-desorption isotherm was measured using a Quantachrome Autosorb-1C TCD analyzer (Model ASICX-TCD6). The surface area and porosity measurements were carried out through nitrogen adsorption desorption analyses at -196 °C using nitrogen (N_2, cross sectional area 0.162 nm^2).

Solid samples were degassed under vacuum at 200 °C for 6 h. Brunauer-Emmett-Teller (BET) equation was used for calculating surface area of the nanoparticles while Barret-Joyner-Halenda (BJH) method applied to the desorption branch of the isotherm was used for calculating pore size distribution.

Zeta Potential measurement: Surface charge on the DOX-BG nanoparticles was measured using Zatasizer Nano-ZA (Malvern Instruments, UK). Particles were dispersed in de-ionized water at a concentration of 0.1 mg/ml and sonicated prior to measurement. Zeta potential measurements are presented as mean ± S.D. of three replicates.

3.2.4 Drug Release Studies

Release of drugs from the prepared DOX-BG nanoparticles was carried out in acidic buffer (pH 4.8) and neutral PBS buffer (pH 7.4). In this study, DOX-BG nanoparticles (1 mg/ml) were added in 10 ml of buffer solution and placed on a shaker incubator set at 37 °C and constant shaking at 150 rpm. Samples for measurement of released drugs were collected at pre-determined time points and replenished with fresh buffer. In order to measure free drug content at each time points, samples were centrifuged at 12,000 rpm for 10 min and supernatant was collected and analyzed via a UV-Visible spectrophotometer (TECAN, Infinite® 200 microplate reader) at λ max 480 nm. Prior to analysis, calibration curve was constructed for doxorubicin at a concentration range of 0.1 to 1 mg/ml. Regression co-efficient was calculated and the release data was calculated as per this standard. Cumulative drug release percentage was calculated and plotted against various time points.

3.2.5 Bioactivity assay

In order to study the *in-vitro* deposition of bone-like hydroxyapatite, DOX-BG samples were immersed in simulated body fluid (SBF) as per procedure described by Kokubo *et al* [63,70]. The DOX- BG samples were adjusted to concentration of 10 mg/ml of total volume of SBF. The samples were incubated for a period of 7 days in a shaker incubator at 37 °C. Samples were recovered post incubation through centrifugation (25°C, 12000 rpm), washed with de-ionized water and dried at room temperature for analysis of bioactivity. Analysis of bioactivity was carried out using FTIR, FE-SEM and XRD.

3.2.6 Cellular studies

Cellular studies included *in-vitro* cytotoxicity on model bone cancer (U2OS) and normal non-cancerous cell line (HaCaT) while qualitative and quantitative cellular uptake analysis of the DOX-BG nanoparticles were carried out in U2OS cell line.

MTT assay: In-vitro cytotoxicity of DOX-BG nanoparticles prepared at various template concentrations were checked in Human Osteoblast-like Osteosarcoma cell line (U2OS) and normal Human Keratinocytes (HaCaT) through MTT assay. Cells were cultured in DMEM-F12 media containing 10 % heat inactivated fetal bovine serum (FBS) and maintained in a cell culture humidified incubator at 37°C and 5% CO_2. All cytotoxic studies were carried out in sterile non-coated 96 well plates with cells seeded at almost 10,000 cells per well. Following day, all cells were treated with increasing concentrations of DOX-BG nanoparticle suspensions prepared using sterile Phosphate Buffer Saline (PBS). Similarly, free DOX was also used for calculating dose dependent cytotoxicity. The concentration of DOX-BG nanoparticles ranged from 0.1 mg/ml to 1 mg/ml while that of free DOX varied according to the weight of free DOX in the DOX-BG particles prepared. All treatments were provided for 24 hours post which each well was washed with PBS for removal of any remnant sample. 3-(4,5-dimethylthiazol-2-yl)-2,5-diphenyltetrazolium bromide (MTT) was used for evaluation of cell viability post treatment. Untreated wells were considered as negative controls. In order to carry out the MTT assay, MTT dissolved in serum free media (Opti-MEM) (Invitrogen) was added to each well to obtain a final concentration of 1 mg/ml and was incubated for 2 h in a humidified incubator at 37 °C. Post incubation period, DMSO was added to each well for dissolving the formed crystals and the absorbance of the solution was measured at 570 nm in a TECAN multiplate reader (TECAN, Infinite® 200 microplate reader).

Cellular viability is calculated as = (OD of the experimental samples)/ (OD of the control) × 100

Cellular uptake: In order to study intracellular uptake of the DOX-BG nanoparticles, fluorescence tagging of the DOX-BG formulations were carried out through addition of fluorescein isothiocyanate (FITC, Sigma -Aldrich). After incubation of DOX-BG formulations and FITC in presence of de-ionized water for 4 hours, particles are centrifuged at 12000 rpm, washed multiple times with distilled water and ethanol for removal of unbound stain and is dried at 37 °C in dark conditions. Once dried, particles are sealed and stored at 4°C.

After treatment of the FITC tagged DOX-BG formulations at concentrations reported in the cytotoxicity study (0.1 to 1 mg/ml) for 24 h on U2OS cell lines, wells were washed repeatedly with 1X PBS for removing any particles that are unbound or present attached to the well surfaces. Post washing, wells were added with 1X PBS and viewed through a Floyd cell imaging station at bright field and green channels and images were recorded. Further, cells were trypsinized from each well post-imaging and quantified for cellular uptake of the fluorescent DOX-BG formulations through flow cytometry (BD *accuri C6*). The resulting data was plotted in the form of a graph for percentage positive cells and mean fluorescent intensity for concentrations of DOX-BG ranging from 0.1 to 1 mg/ml.

3.2.7 Statistical analysis: Comparisons between control and treatment groups were analyzed using unpaired t- tests with p value ≥ 0.05 (95% CI) indicating significance. All graphs were constructed using Origin® and statistical analysis was carried through Graphpad Prism® for Windows.

3.3 Results and discussions

3.3.1 Synthesis of Doxorubicin-bioactive glass (DOX-BG) nanoparticles

Doxorubicin was dissolved in TRIZMA® buffer (pH 8.5) at variable concentrations (0.25 mg/mL, 0.50 mg/mL, and 0.75 mg/ mL). The doxorubicin TRIZMA® solution was placed on a magnetic stirrer at 500 rpm at temperature of 37°C. Various precursors of bioactive glass-ceramic like Tetraethyl orthosilicate (TEOS), Triethyl Phosphate (TEP), Sodium Acetate (NaAc) and Calcium Acetate (CaAc) were added sequentially at an interval of 30 min. The concentration of all precursors has been optimized based on earlier studies carried out with other templates through this method [37,39,55,62,108]. It has been observed in traditional Stober's method that increasing concentration of precursor like TEOS or an increased reaction time led to increase in size of the particle formed [109,110]. The bio-inspired method is a modified Stober's method where there is no requirement of alcoholic solutions for reduction of tetraethoxysilanes in presence of ammonia. Rather, a controlled hydrolysis and condensation of TEOS can instead be achieved in presence of TRIZMA® buffer at mild alkaline pH in presence of a template. It is to be mentioned that even after extracting the formed pellet post 12 h of reaction time through centrifugation, allowing the reaction solution to age produces more depositions over time. However, with increase in time and extraction of first round of particles, the concentration of the template drug decreases and the amount of drug that gets encapsulated reduces drastically which can be observed visually through reduction of intensity of the red color of the DOX-BG ceramic nanoparticles. It is due to this reason that DOX-BG ceramic particles obtained in the first round of extraction (12 h) for all concentrations of DOX were solely applied in all studies. Under similar reaction conditions parallel synthesis was carried out using the pre-cursors in TRIZMA® solution without the presence of template. It is to be mentioned that depositions formed without template not only took longer (1 week to 1 month) to form in substantial amount but also lacked homogenous particle size and demonstrated high aggregation.

3.3.2 Optimizing DOX loading through variation of template concentration

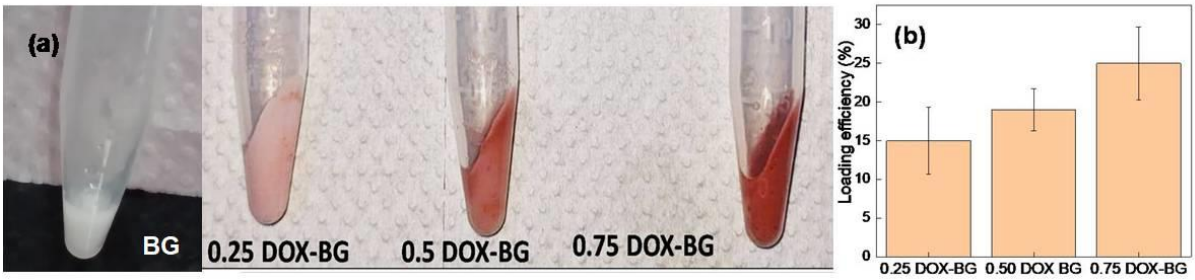

Figure 3.1: (a) Optical images of BG ceramic prepared without template DOX and DOX-BG ceramic nanoparticles prepared with different concentrations of Doxorubicin (0.25 mg/mL, 0.50 mg/mL, and 0.75 mg/mL) and (b) doxorubicin loading efficiency

In order to optimize the loading efficiency of DOX while formulation with bioactive glass, increasing concentration of DOX was tried as template (Figure 3.1). In sol-gel based studies, drug loading is often attributed to formation of drug-micelles through surfactants which plays a major role in determining loading efficiency [96,111]. Through the bio-inspired route, due to absence of surfactants, template concentration was considered as rate limiting component for drug loading. With increasing doxorubicin concentration in the TRIZMA® solution (in the range 0.25 to 0.75 mg/ml), marginal increase in loading efficiency could be observed but was not statistically significant. Overall, loading efficiency is within a range of 15 to 25% and does not differ significantly due to change in concentration of drug template considered in our case. The absolute amount of loaded DOX in each DOX-BG ceramic nanoparticle increases with increase in template concentration without significantly impacting the loading efficiency or the size of nanoparticles [100,101]. In a similar situation of DOX-silica synthesis through the sol-gel approach, Jiang *et al* stated loading efficiency to decrease further on increasing DOX or Tween-80 concentration above a particular concentration. This was observed even though absolute amount of DOX increased on enhanced DOX addition to the reaction mixture [96]. In a similar strategy by Wang *et al*, DOX was added to the traditional Stober's growth medium of silica nanoparticles without any surfactant to "grow DOX inside" the nanoparticles rather than post-

synthesis absorption of the drug on its surface [101]. The study also reported tuning of DOX concentration to optimize drug loading in the silica nanoparticle.

3.3.3 Size and morphology

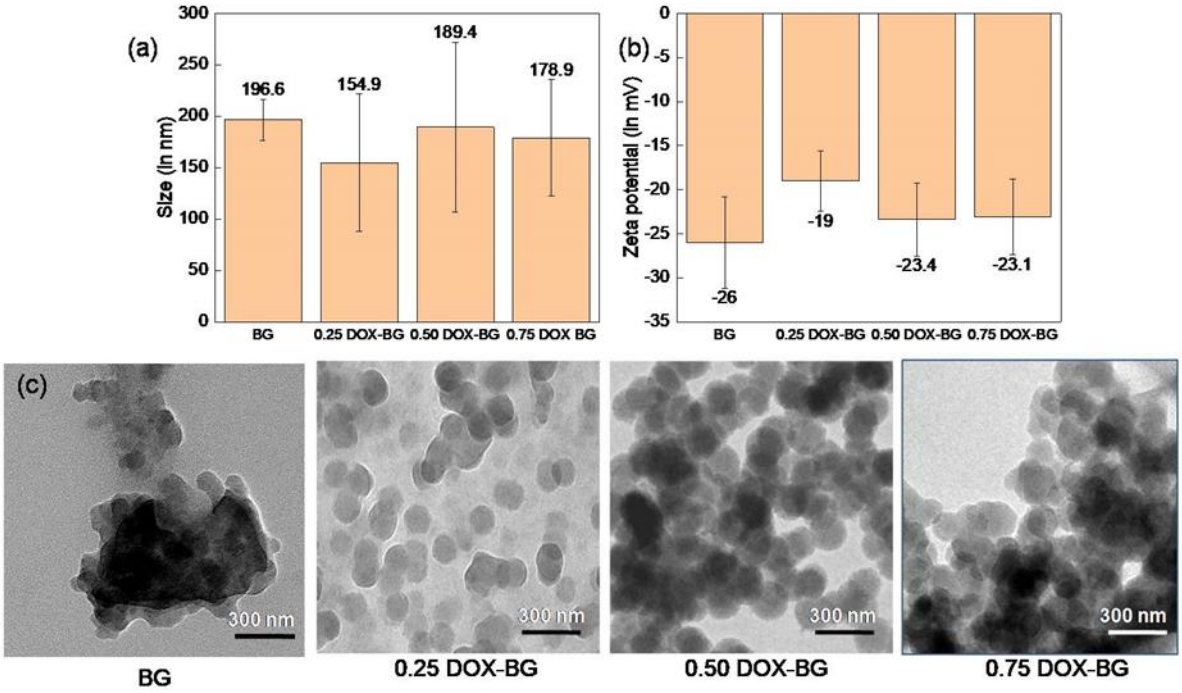

Figure 3.2: (a) Size of BG ceramic and DOX-BG ceramic nanoparticles as measured through DLS; (b) surface charge of the nanoparticles as observed through zetasizer and (c) (left to right) TEM images of the BG, 0.25, 0.50 and 0.75 DOX-BG ceramic nanoparticles, scale 0.3 µm.

Particles generated at various template concentrations have a range of average hydrodynamic radius of 150 nm to 200 nm when checked through DLS (Figure 3.2a). However, through TEM, much smaller sizes can be observed (Figure 3.2c). This can be since DLS reports particle sizes based on hydrodynamic radius when in water [112]. No statistically significant difference in size of nanoparticles could be observed with increasing template concentration. BG ceramic prepared without template demonstrated high aggregation but lesser with DOX-BG. In an earlier study, xerogels reported in case of the DOX-bioactive silica co-synthesized formulations reported sizes in micrometer range [105].

It is noteworthy to state that the sizes of the xerogels did not differ based on applied DOX concentrations like that observed in our case [105]. This suggests that particle size may not be a function of template concentration in our case but may have been regulated by pH, reaction time and temperature which has also been described for traditional Stober's methods [113]. However, we have observed in previous studies that concentration of template may lead to increase in size for one-pot DOX silica nanoparticles [96]. The reason attributed was due to DOX loading micelles which was a result of addition of surfactant in the reaction medium. Since the current study is free of surfactant, the phenomenon may not be pronounced in this case. Moreover, in presence of TRIZMA®, the ionic strength of DOX may not be too strong to promote larger sizes of formed bioactive glass-ceramic nanoparticles. In case of zeta potential, the surface charge of the DOX-BG ceramic nanoparticles was mostly found to be negative (15 to 23 mV) and is in accordance with reported literature (Figure 3.2b) [99,112,114].

On increased concentration of DOX template, the surface charge of the formed nanoparticles becomes more negative [114]. This is due to distribution of the DOX both in the inside and its presence on the outer surface of the nanoparticles [114]. BG ceramic alone without DOX demonstrated a negative charge of ~ 26 mV.

3.3.4 Physico-chemical characterization

FTIR: Through FTIR studies (Figure 3.3a), prominent peaks could be observed in case of 0.75 DOX-BG ceramic in the range of 1600 to 1400 cm^{-1} which can be due to the presence of the DOX in the DOX-BG ceramic nanoparticles. The intensity of the peaks from 1600 to 1400 cm^{-1} decreases for 0.50 and 0.25 DOX-BG ceramic nanoparticles probably due to comparatively lower drug presence when compared to 0.75 DOX-BG ceramic nanoparticles. The peaks at 1612 cm^{-1} ,1643 cm^{-1} and 1576 cm^{-1} can be attributed to C=O or C=C/C N groups of DOX [114]. Peaks in the range of ~1100 cm^{-1}, ~958 cm^{-1} and ~467 cm^{-1} could be observed for all DOX-

BG ceramic nanoparticles and corresponds to Si-O$^-$ stretches in Si-O-Si bond in the bioactive glass-ceramic structure [38,114,115]. Peaks at ~790 cm^{-1} observed for all DOX-BG ceramic nanoparticles correspond to Si-O$^-$ symmetric bending and stretching vibrations in the silica ring structure of the bioactive glass and C-S-C stretching vibrations [38,114]. The band at ~550 cm^{-1} corresponds to P-O vibrations present due to the interaction of the phosphate group with non-bonding Si-O$^-$ groups in the bioactive glass-ceramic structure [89]. In case of BG prepared without DOX, the highly intense peaks observed from 1550 to 1400 cm^{-1} along with peaks corresponding to SiO_2 (1100 cm^{-1}, 956 cm^{-1}, 795 cm^{-1}) indicate BG ceramic doped with crystalline carbonated hydroxyapatite [116,117] probably due to longer reaction time (1 week to month) in TRIZMA leading to deposition of carbonated hydroxyapatite nanocrystals on formed BG ceramic particles.

FTIR data suggests that the linkage between doxorubicin and bioactive glass-ceramic structure is mainly physical in nature. Majority of physical forces involved may be hydrogen bonding, electrostatic and hydrophobic forces of interactions. On comparison of FTIR peaks with free DOX, it was observed that the peak at 1640 cm^{-1} for free DOX corresponding to C=O vibrations as well as O-H and N-H bending vibrations of amide-I shifts towards lower wave number as a doublet at 1620 cm^{-1} and 1565 cm^{-1} for 0.75 DOX-BG. The changes observed in the peak at 1640 cm^{-1} vibrations of DOX and its shift as a doublet to lower wave number may indicate interaction through hydrogen bonding between O-H and N-H group of DOX with Si-O$^-$ bond of bioactive glass-ceramic network [38]. At pH 8.5, the amine groups of DOX being protonated may also get attracted towards the hydrolyzed silica precursor (Si-O$^-$) which is negatively charged thus leading to formation of complexes through electrostatic interactions. Further, the photo stability of the drug has been reported to improve when present in encapsulated form in pores of silica structure [114].

TGA: Thermogravimetric analysis of bioactive glass-ceramic particles with and without DOX depicts different thermograms (Figure 3.3c). For BG ceramic formulations without DOX, 23 wt/ wt% weight loss could be observed throughout the temperature range. Majority of the weight loss occurred at 100°C indicating removal of bound water as well as dihydroxylation of the silanol groups present in the BG ceramic formulations [97,118]. Also, BG prepared without DOX being crystalline may also contain water of crystallization thus constituting the weight loss observed. However, for DOX-BG ceramic nanoparticles (0.75 mg/ml template concentration), 50 wt/wt% weight loss could be observed throughout the temperature range. Apart from the first round of weight loss observed at 100°C corresponding to removal of bound water, rapid weight loss could be observed from 200°C corresponding to melting point of DOX (205°C) [89]. The gradual weight loss continued till 500°C owing to the intense combustion of DOX in the DOX-BG ceramic sample [89]. This indicates the presence of DOX in the bioactive glass-ceramic complexes that gets degraded at the range of 200 to 500°C [89,97]. The total weight loss of ∼50 wt/wt% observed in DOX-BG ceramic samples corroborates the loading efficiency data of ∼25% considering 15–20 wt/wt% weight loss is due to presence of bound water. For 0.25 and 0.50 DOX-BG, ∼20% and 30% weight loss could be observed indicating lower presence of DOX when compared to 0.75 DOX-BG.

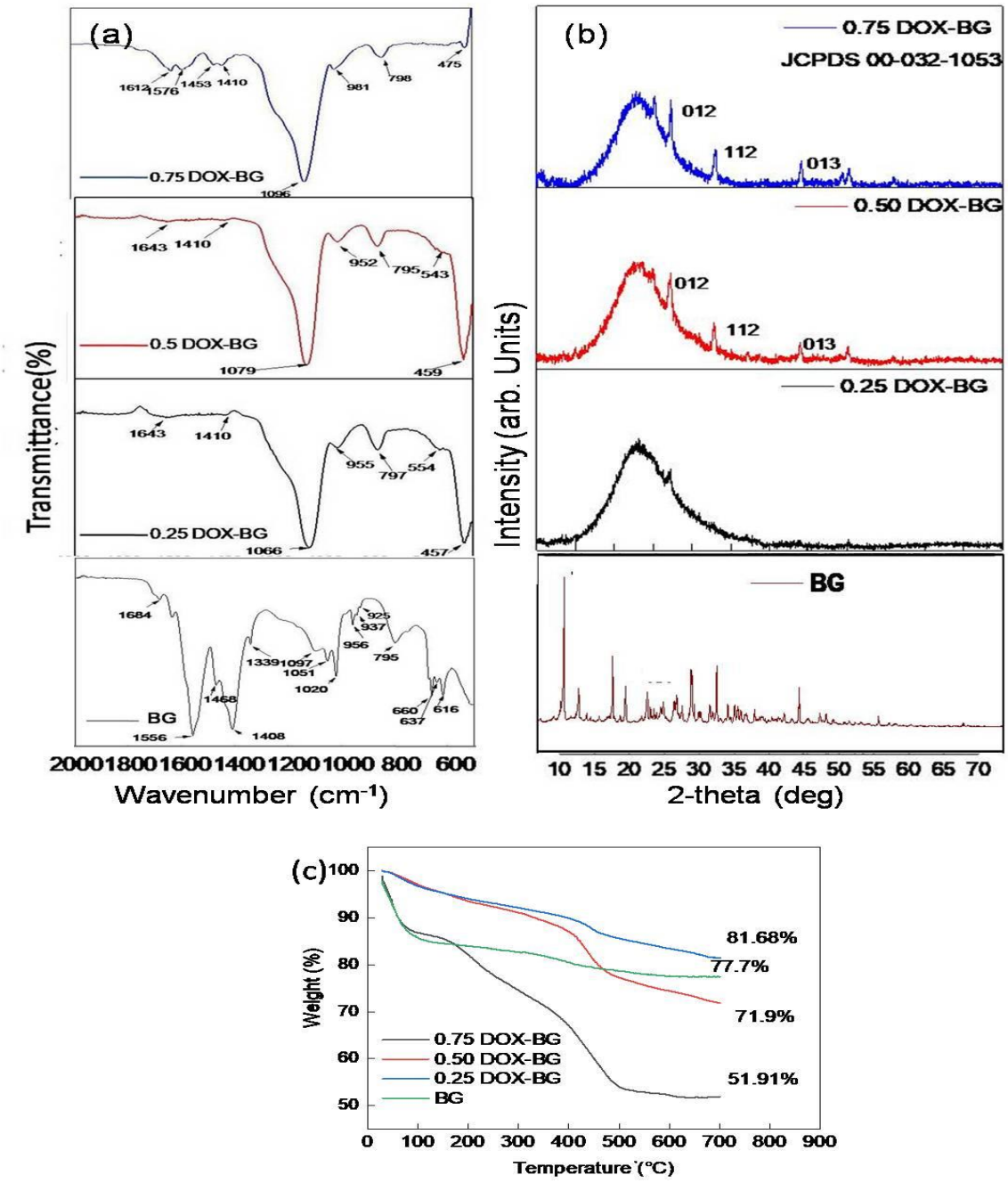

Figure 3.3: (a) FTIR spectra of 0.25 DOX-BG, 0.50 DOX-BG ceramic and 0.75 DOX-BG;(b) XRD of 0.25, 0.50 and 0.75 DOX-BG ceramic and (c) TGA thermogram of 0.75 DOX-BG ceramic and BG ceramic particles synthesized in absence of DOX

XRD: XRD diffractogram indicates semi-crystalline nature of the DOX-BG ceramic nanoparticles with broad characteristic diffraction 2θ maxima from 10–30° (Figure 3.3b) along with a few diffraction maxima. Diffraction maxima at 25°, 27°, 33°, 44°, 50° and 56° could be observed in 0.75 DOX-BG ceramic nanoparticles which gradually decreased in intensity or

disappeared in the 0.50 and 0.25 DOX-BG ceramic nanoparticles. The reported diffraction maxima correspond to $Ca_4Na_2O_{12}P_2Si$ (JCPDS 00-032-1053). The presence of higher amount of organic molecule (DOX in this case) regularizes the orientation of bioactive glass ceramic network leading to semi-crystalline nature of the DOX-BG ceramic nanoparticles [37]. As such we refer to DOX-BG nanoparticles also as BG-ceramic nanoparticles in this study.

Although DOX is a crystalline compound, the encapsulation of the same in the narrow spaces in the bioactive glass-ceramic architecture may have led to its amorphousness as no peaks can be observed when compared to reported diffraction pattern of DOX in literature [105]. The missing diffraction pattern of DOX in the DOX-BG ceramic nanoparticles is probably due to almost complete dispersion of the drug in the bioactive glass-ceramic matrix, shielding effect of the bioactive glass ceramic structure or due to the inadequate detection levels of the instrument to detect the presence of lower amount of DOX in the samples. Such phenomenon has been reported earlier in case of crystalline drugs dispersed in mesoporous silica nanoparticles [98,105,119]. Interestingly BG ceramic synthesized without the presence of DOX turn out to be heterogeneously crystalline in nature with peaks that match partially with various crystals (JCPDS: 01-084-0151 $Na_3Ca(SiO_3)(PO_4)$ Sodium Calcium Silicate Phosphate; JCPDS 00-031-0582 $H_2Si_2O_5$, Hydrogen Silicate; JCPDS: 00-024-0033 $Ca_5(PO_4)_3(OH)$, Hydroxy apatite). This can be due to the long time the particles require to be formed in substantial amount during which the additional sodium, calcium and phosphate ions in the solutions deposits on surface of BGs to form nanocrystals.

EDS: Elemental composition of free DOX and DOX-BG ceramic nanoparticles has been presented in Figure 3.4. In case of free DOX, presence of mainly C and O can be observed corresponding to its structure containing carbon chain backbone and terminal OH groups. The elemental composition of 0.25 DOX-BG, 0.50 DOX-BG and 0.75 DOX-BG ceramic consists majorly of Si and O which are the prime components of bioactive glass-ceramic structure.

Presence of O may have been from the O^- in DOX as well from the Si-O-Si bonds or Si- O^- non-bonding oxygen present in the bioactive glass-ceramic structure. Apart from this, elemental peaks of sodium, phosphorous and calcium can further be detected in all DOX-BG ceramic nanoparticles indicating successful integration of the same in the Si-O^- network.

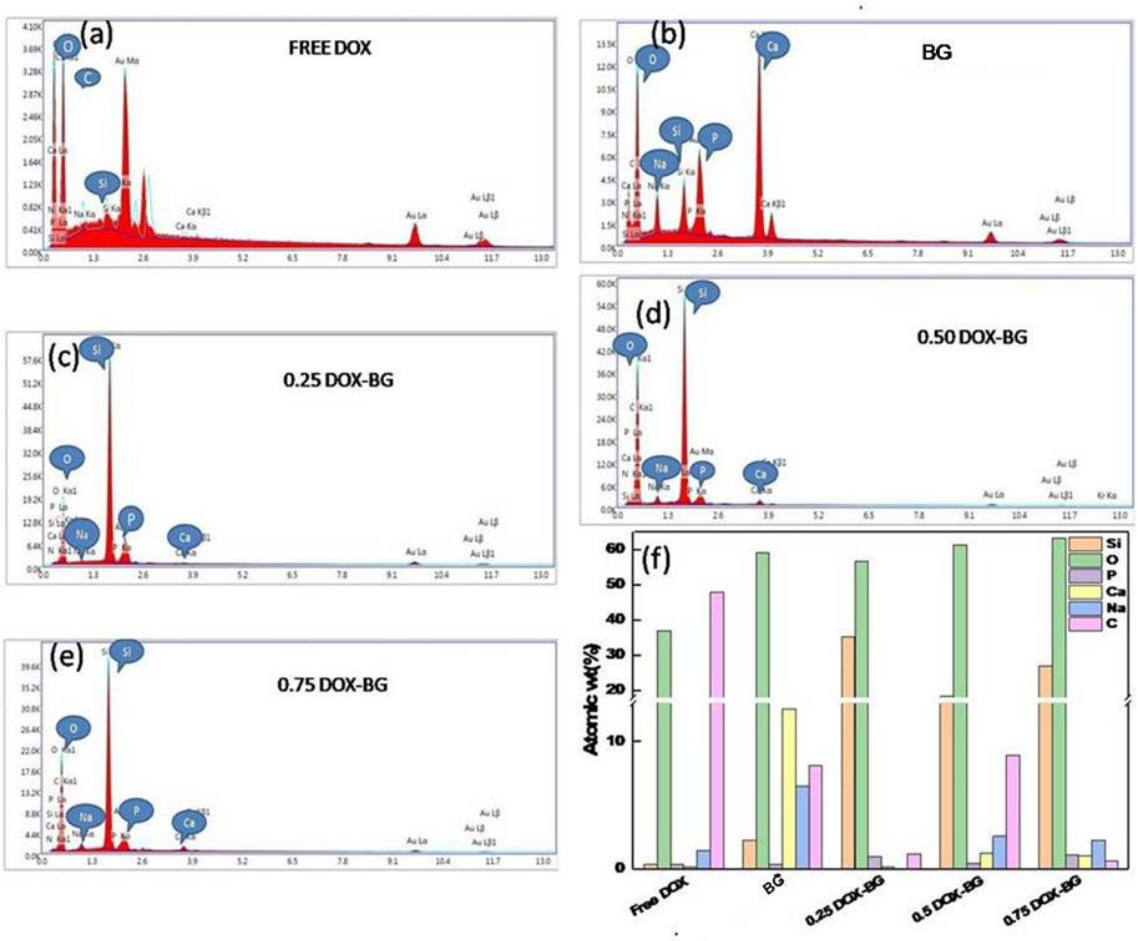

Figure 3.4: Elemental composition as obtained from SEM coupled with EDS of (a) Free DOX,(b) BG ceramic without DOX, (c) 0.25 DOX-BG ceramic, (d) 0.50 DOX-BG ceramic and (e) 0.75 DOX-BG ceramic. (f) Graphical representation of the comparison of atomic wt. (%) of the different elements in each sample.

However, when compared to previous studies, the amount of Ca was seen to be lower possibly due to removal of the salts during the washing steps [87,108,112]. Another reason can be due to compromised interactions of Ca^{2+} ions with the non-bonding O of the Si- O^- groups present in the BG ceramic structure due to the interactions of the latter with DOX. Also, EDS analysis

generally detects components on the surface of materials which in this case is pre-dominantly occupied by DOX. The presence of higher levels of Ca in the template free BG ceramic provides hints towards the same. Further this corroborates the FTIR and XRD data obtained for the same. The presence of Au can be observed for all compositions due to the coating of samples while carrying out SEM coupled with EDS analysis.

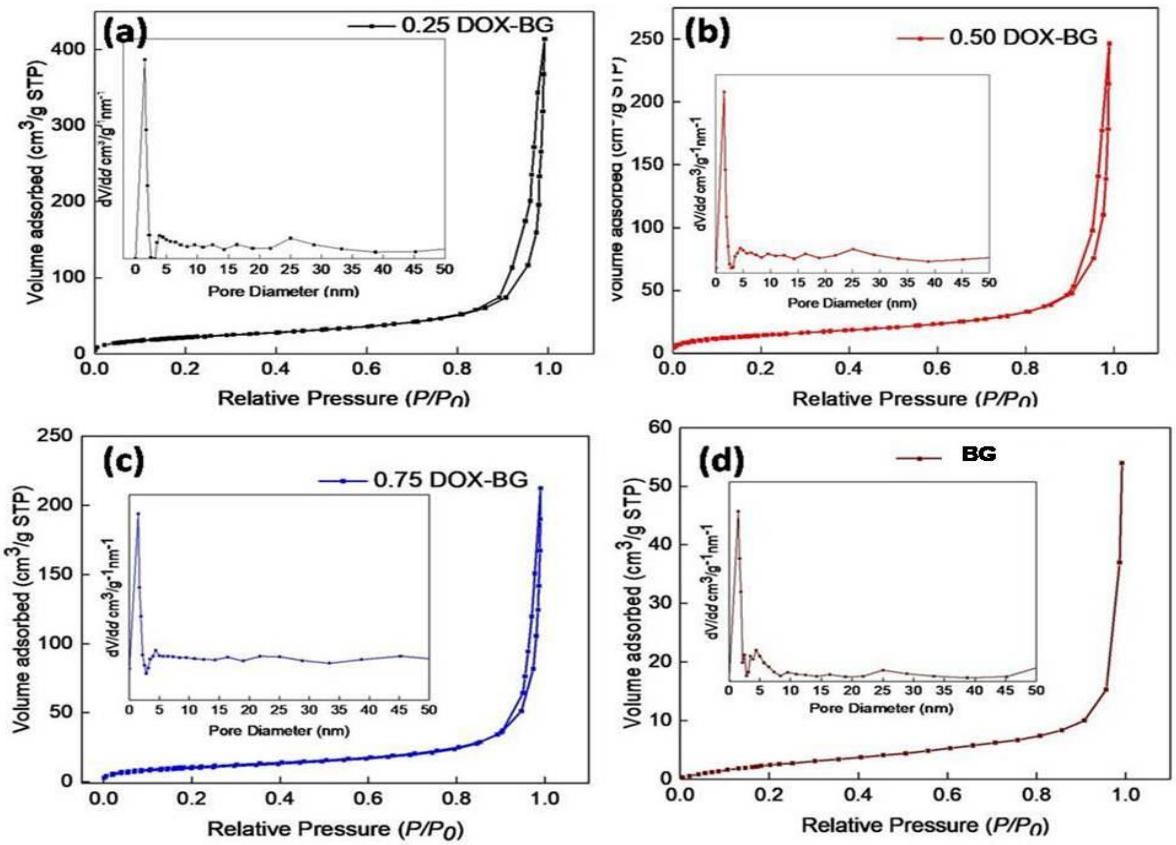

Figure 3.5: Comparison of the nitrogen adsorption-desorption isotherms and respective pore -size distribution of (a) 0.25 DOX-BG,(b) 0.50 DOX-BG, (c) 0.75 DOXBG ceramic and (d) BG ceramic prepared without DOX.

Nitrogen adsoprtion-desorption analysis (BET): Nitrogen adsorption desorption isotherm revealed Type V adsorption-desorption isotherm pattern and Hysteresis Loop 3 for 0.25, 0.50 and 0.75 DOX-BG ceramic nanoparticles indicating slit like pores (Figure 3.5 a, b and c respectively)[120]. No hysteresis loop can be observed for BG prepared without DOX indicating a uniform non-porous structure (Figure 3.5d). All DOX-BG ceramic nanoparticles were observed to be mesoporous in nature with highest pore volume of 0.65 cm^3gm^{-1} and surface area of 113.1 m^2gm^{-1} for 0.25 DOX-BG ceramic nano particles. The specific surface area, pore diameter and pore volume was calculated through the Bennet-Emmett-Teller (BET) and Barrett-Joyner-Halenda (BJH) methods for each sample and have been provided in Table 3.1. Comparative lower pore volume and surface area observed in case of DOX-BG ceramic nanoparticles can be due to lack of surfactant during synthesis and covering of surface of the nanoparticles due to adsorption of DOX.

Pore characterization	**0.25 DOX-BG**	**0.50 DOX-BG**	**0.75 DOX-BG**	**BG without DOX**
BJH surface area (in m^2/g)	113.1	69.39	53	22.22
Average Pore diameter (in nm)	22.9	22.17	23.74	15.38
BJH Cumulative desorption pore volume (in cc/g)	0.65	0.38	0.31	0.085

Table 3.1: Pore characterization of 0.25 DOX-BG, 0.5 DOX-BG, 0.75 DOX and BG synthesized without DOX through Brunauer–Emmett–Teller (BET) analysis

Earlier studies on one-pot DOX-silica nanoparticles synthesis have reported similar pore structure but with larger pore volume and surface area [96]. However, such porosity can only be obtained on removal of the surfactant or the drug from the nanoparticles. In the study by Jiang *et al*, the porosity was obtained through Tween-80/drug micelles and had to be removed through heating for obtaining the porous characteristics (warm-hole like structures) [96]. In our

study, with increase in concentration of template, difference in terms of characteristics Earlier studies on one-pot DOX-silica nanoparticles synthesis have reported similar pore structure but with larger pore volume and surface area [96]. However, such porosity can only be obtained on removal of the surfactant or the drug from the nanoparticles. of mesoporosity like surface area, pore diameter and pore volume could be observed with maximum being observed for 0.25 DOX-BG when compared to 0.50 and 0.75 DOX-BG ceramic nanoparticles probably due to lower drug content in the BG structure [115,121]. We observe porous nature for the DOX-BG ceramic nanoparticles without removal of the drug. This can be due to the irregularities in the bioactive glass-ceramic structure due to presence of non-bonding oxygen and presence of PO_4^{3-}, Ca^{2+}, Na^{+} ions in the silica ring structure acting as network modifiers.

Such an observation has been earlier recorded for bioactive glass-ceramic and other inorganic depositions in case of bio-inspire routes of synthesis in presence of Tris(hydroxymethyl)aminomethane buffers [25,37–39,69,108]. In a study by Lin *et al* on sol-gel synthesis of 70S30C bioactive glass-ceramic particles, the presence of large number of nanopores on 70S30C particles could be detected through nitrogen adsorption-desorption method and was attributed to be derived from interstitial spaces between secondary particles. The pores were further reported to be modified (by lowering of modal pore size) post prolonged sintering at 800°C for a period up to 16 h [92]. BG normally synthesized without templates through melt-quenching methods and traditional Stober's method are generally with limited surface area as it is solid and non-porous in nature and denser than silica nanoparticles due to presence of Ca and other cations [112].

3.3.5 Drug release studies

In-vitro drug release profile of DOX from DOX-BG ceramic nanoparticles was carried out in acidic buffer adjusted to pH 4.8 as the internalized particles in cells are generally trapped in

endosomal or lysosomal pH which is generally acidic in nature [96,114]. It was observed that the DOX-BG ceramic nanoparticles synthesized with increasing DOX concentrations as template could release doxorubicin slowly and steadily within first 24 hours (Figure 3.6a). In fact, the absolute amount of DOX being highest in 0.75 DOX-BG ceramic nanoparticles (as observed from loading studies) established highest release (~40–48%) when compared to 0.25 and 0.50 DOX-BG ceramic nanoparticles (10–25 %)[90,114]. Drug release was also checked in neutral pH 7(Figure 3.6b). However, small amount of drug release (~11%) could be observed which reached a plateau stage by 4 h. This is a significant observation as it provides control over release site of DOX. It prevents premature release of drug when in circulation and will significantly start releasing drug only when in presence of acidic environment generally encountered in intra-cellular compartments like lysosomes or late endosomes.

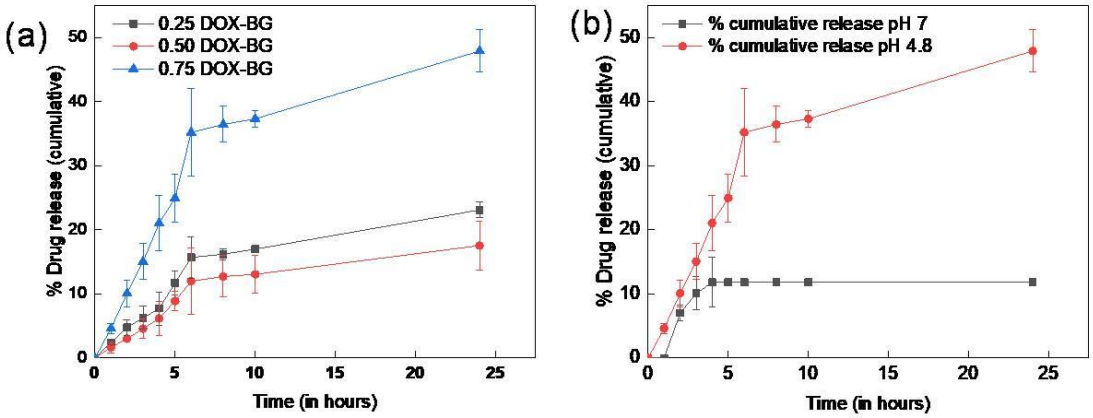

Figure 3.6: % cumulative drug release from DOX-BG ceramic nanoparticles; (a) drug release profile from 0.25 DOX-BG, 0.50 DOX-BG and 0.75 DOX-BG ceramic nanoparticles at pH 4.8 and (b) comparison of % cumulative drug release profile of 0.75 DOX-BG ceramic nanoparticles at pH 4.8 and pH 7.

The period of drug release was observed for 24 h keeping in mind cellular *in-vitro* studies where cytotoxic effect of the DOX-BG ceramic nanoparticles was observed for 24 h. Drug release was observed to be above LD50 values obtained from cyto-toxicity studies. Higher and

sustained drug release profile for DOX-BG ceramic in acidic environment when compared to that at neutral pH can be due to the weakening of the electrostatic interaction of protonated DOX with the ionized silanol in the Bioglass® structure [96,101,114,122]. Also, DOX is reported to be more stable in acidic environment due to enhanced hydrophilicity which further leads to better release in acidic pH [97]. Further, comparatively slower and steady dissolution of the compact bioactive glass-ceramic matrix in DOX-BG ceramic nanoparticles in presence of acidic pH may contribute to the slow and sustained drug release [96]. The initial drug release can also be due to DOX bound to the outer surface of the DOX-BG ceramic nanoparticles. As DOX was added during the formation and growth of the bioactive glass-ceramic nanoparticles rather than external loading, the release may have been slower as the penetration of the release media may have been limited deeper in the complex [123]. In case of neutral pH, the dissolution of the bioactive glass-ceramic structure is slower (due to higher stability of the bioactive glass-ceramic matrix) thus accounting for the lower release observed. The drug release observed in this case in the first few hours may have been due to release of the drug bound to the external surface of the bioactive glass ceramic structure [100].

3.3.6 Bioactivity studies for DOX-BG nanoparticles

FESEM/TEM: In order to carry out bioactivity or *in-vitro* hydroxyapatite forming ability of the DOX-BG ceramic nanoparticles, the nanoparticles were immersed in SBF for period of 7 days. Post immersion period, the particles obtained were observed for change in morphology through FE-SEM (Figure 3.7a). While round shaped nanoparticles could be observed prior to immersion of the particles in SBF, incubation of the nanoparticles in presence of SBF lead to change in morphology. As observed, the round shape of the particles was converted to spiky or worm like morphology depicting formation of crystalline apatite formation. This observation is similar to studies reporting hydroxyapatite deposition on bioactive glass- ceramic materials in literature when incubated in presence of SBF thus depicting bioactivity of the nanoparticles

[88]. TEM images of BG ceramic indicate unchanged morphology (Figure 3.7b) as the particles already have deposited hydroxyapatite nanocrystals on its surface when extracted from reaction medium after 7 days.

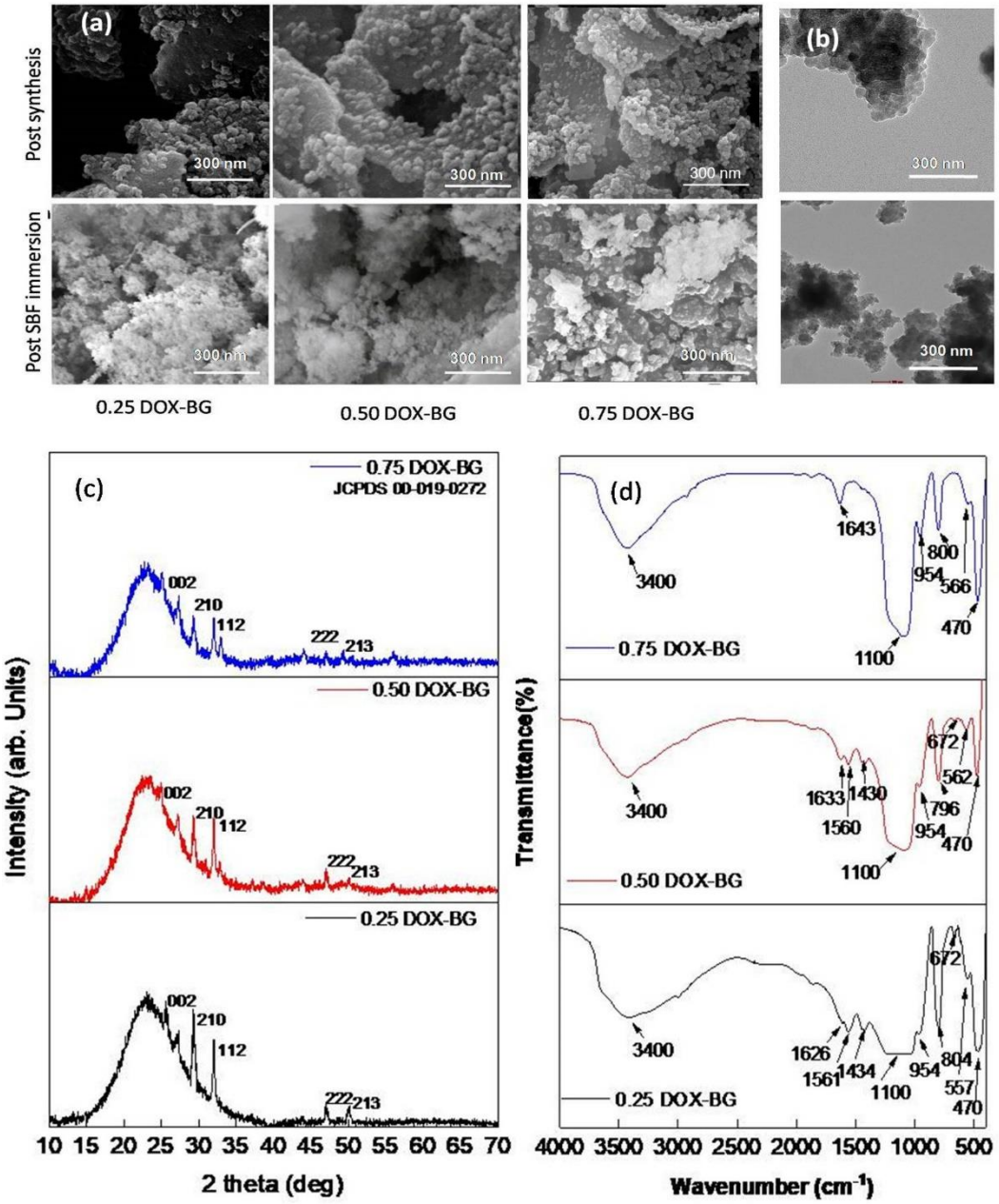

Figure 3.7: (a) Morphology of 0.25, 0.50 and 0.75 DOX-BG ceramic nanoparticles before (upper pane) and after immersion (lower pane) in SBF for 7 days observed through FE-SEM; image scale-0.3 μm, (b)TEM images of BG before (up) and after immersion (below) in SBF, (c) XRD and (d) FTIR of 0.25, 0.50 and 0.75 DOX-BG ceramic nanoparticles post immersion.

Apart from SEM; FTIR and XRD analysis was carried out to evaluate the bioactivity of the DOX-BG ceramic nanoparticles (Figure 3.7b and 3.7c).

FTIR: For FTIR, bonds centered at ~670 cm^{-1} and 560 cm^{-1} may appear as a result of formation of crystalline calcium phosphate [88]. The peaks pertain to the P-O vibrations in the crystalline phosphate group [89]. Peaks at 3400 cm^{-1} and 1640 cm^{-1} indicate O-H from hydroxycarbonate apatite (HCA) deposition [90]. Peaks in the range of 1600 to 1400 cm^{-1} correspond to various carbonate bonds [124] and can be a result of the formation of carbonate apatite. However, peaks in this range and corresponding to C=C/C-N bonding may also appear as a result of presence of doxorubicin. Broad peak at ~1100 cm^{-1} while a sharp peak at 790 cm^{-1} to 800 cm^{-1} along with shoulder at 954 cm^{-1} and 569 cm^{-1} correspond to phosphate group [38]. Presence of phosphate, carbonate and hydroxyl groups indicate successful formation of HCA on the DOX-BG ceramic nanoparticles. When compared to FTIR peaks of normal DOX-BG ceramic samples (Figure 3.4) the peaks corresponding to P-O vibrations (especially ~570 cm^{-1}) appeared to increase in intensity in the samples immersed in SBF thus indicating presence of greater number of phosphate groups. As observed for 0.50 and 0.25 DOX-BG ceramic samples, appearance of peak at ~670 cm^{-1} indicates vibrations of phosphate groups in the SBF incubated samples. The presence of lower amount of loaded DOX in the 0.50 DOX-BG and 0.25 DOX-BG ceramic may have added slight advantage for formation of hydroxyapatite. In case of XRD, the amorphous nature of the DOX-BG ceramic nanoparticles could be characterized through the typical broad diffraction maxima in the range of 15 to 30°. On immersion in SBF, diffraction maxima (002), (210), (112), (222) and (213) [89] could be observed corresponding to HCA ($Ca_{10}(PO_4)_3(CO_3)_3(OH)_2$) phase [JCPDS00- 019-0272] at 2θ values of 25°, 29°, 32°, 47° and 49° respectively [38,90,105]. The intensity of the diffraction maxima appears to increase with decrease in drug content in SBF suggesting formation of HA on the DOX-BG ceramic surface.

The peaks appear prominent in case of 0.25 DOX-BG but decreases gradually for 0.50 and 0.75 DOX-BG. This is probably due to limited Si-OH groups on surface of 0.75 DOX-BG compared to 0.50 and 0.25 DOX-BG. When in presence of SBF, due to exchange of Na^+ and Ca^{2+} of bioactive glass-ceramic with H^+ and H_3O^+ in the surrounding solution, the Si-O-Si linkages present in bioactive glass ceramic structure hydrolyze leading to formation of silanol groups at the silica-solution interface. This results in release of $Si(OH)_4$ in the solution as a result of dissolution of the bioactive glass-ceramic network. The $Si(OH)_4$ groups in solution undergo condensation and re-polymerization with the available silanol groups on the bioactive glass-ceramic structure thus forming SiO_2 gel layer which acts as heterogeneous nucleation site for diffused Ca-P deposition from the solution. Subsequent deposition of calcium and phosphate from the surrounding SBF solution results in $CaO\text{-}P_2O_5$ gel-like layer. This gel like layer subsequently develops into amorphous $CaO\text{-}P_2O_5$ layer on the SiO_2 gel layer and with time forms crystalline HCA on the bioactive glass-ceramic surface through interaction with OH^- and CO_3^{2-} anions from the SBF solution [91]. The HCA crystals formed on the bioactive glass-ceramic nanoparticles allows binding of the nanoparticles in bones and acts as substrates for bone growth and regeneration. It also plays significant role in bone wound healing.

3.3.7 Cytotoxicity and cellular uptake of DOX-BG nanoparticles towards normal and cancer cell lines

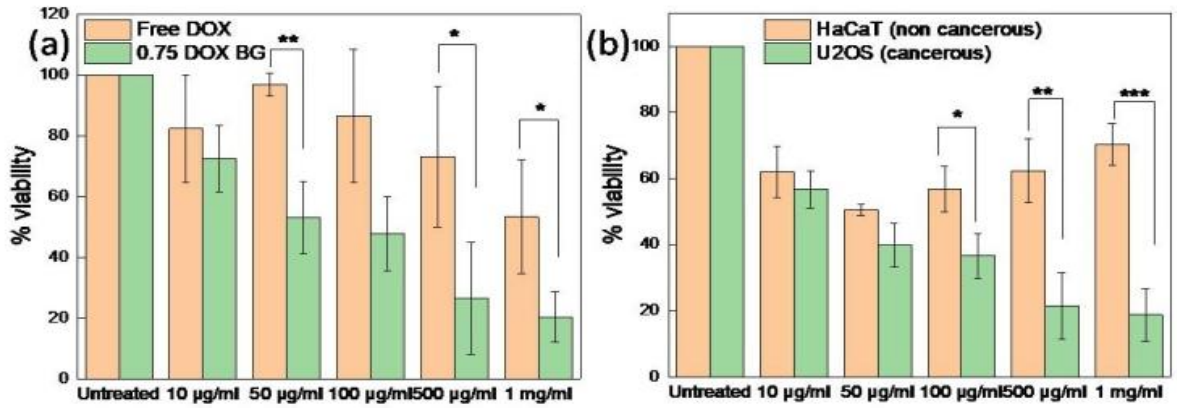

Figure 3.8: *In-vitro* cytotoxicity analysis through MTT assay of (a) 0.75 DOX-BG ceramic nanoparticles and equivalent free drug on U2OS cell line, (b) comparative cytotoxicity profile of 0.75 DOX-BG ceramic nanoparticles on U2OS (cancerous) and HaCaT (non-cancerous) cell line. Statistical significance is obtained as p values ≤ 0.05. LD50 for 0.75 DOX-BG is observed at 50 μg/ml.

MTT assay:

In-vitro cytotoxicity of the DOX-BG ceramic nanoparticles along with free DOX was carried out on human osteoblast like osteosarcoma cell line (U2OS) through MTT assay (Figure 3.8a). MTT provides an estimation of cellular viability through measuring mitochondrial activity which reduces the tetrazolium component of MTT into solid formazan crystals which remain deposited in the wells. The biocompatibility of native bioactive glass-ceramic nanoparticles without anti-cancer drugs have been proven in earlier studies [37,108]. Due to superior loading and release properties of 0.75 DOX-BG ceramic nanoparticles when compared to 0.25 and 0.50 DOX-BG ceramic nanoparticles, 0.75 DOX-BG ceramic nanoparticles have been mainly reported for studying cytotoxicity activity. With increasing concentration of 0.75 DOX-BG ceramic nanoparticles (10 μg/ml to 1 mg/ml), cytotoxicity was observed to have increased in a dose dependent manner [87,88,114]. It was observed that the loading efficiency of DOX is about 25% of the weight of the DOX-BG ceramic nanoparticles. As such, in order to compare the efficacy of the DOX-BG ceramic nanoparticles with equivalent free drug (i.e., 25% wt/wt of free drug of each concentration of DOX-BG), MTT assay for free drug concentrations were compared to corresponding DOX-BG concentrations. It was observed that the DOX-BG ceramic nanoparticles performed better in terms of cell killing of osteosarcoma cells when compared to free drug. Statistically significant difference ($p < 0.05$) could be observed in cell killing between free drug and corresponding DOX-BG ceramic nanoparticles for multiple concentrations. In order to check for specificity of cell killing when compared to non-cancerous cells, a comparative study was carried out for cytotoxicity of DOX-BG ceramic nanoparticles on HaCaT cells and was compared with U2OS cells (Figure 3.8b). As observed, the DOX-BG

ceramic nanoparticles were more toxic to cancer cell lines when compared to non-cancer cell line like HaCaT. The effect seems to be more pronounced when treatment is given at higher concentrations. Although there was also killing of HaCaT cells which are known to be vulnerable to cytotoxic effects of DOX, the killing is seen to be more in cancer cell line. The reason can be since increased reactive oxygen species (ROS) production in cancer cells leads to low oxygen concentration in the intracellular spaces and hence is characterized by higher acidic environments. These may have prompted a better drug release in case of U2OS cells containing the endocytosed DOX-BG ceramic nanoparticles [96].

Cellular uptake:

On entry through endocytosis, the DOX-BG ceramic nanoparticles once inside the cell can escape the endo-lysosomal compartments resulting in sustained drug release and uninhibited distribution in nucleus and cytosol [122,125].This indicates that the DOX-BG ceramic nanoparticles can be an attractive formulation strategy for doxorubicin related treatment regimes. It indicates that lowering of dosage of doxorubicin may result in management of its side effects. Indeed, we have checked with free DOX concentrations equal in weight to complete formulation (wt/wt). For instance, 1 mg/ml of free doxorubicin generated similar cytotoxicity to 1 mg/ml DOX-BG ceramic formulation which in original contains ~1/4th wt/wt of drug content.

In order to estimate the cellular uptake behavior of the nanoparticles, we tagged the 0.75 DOX-BG ceramic nanoparticles with FITC. Although DOX is itself fluorescent in nature, FITC tagging of the DOX-BG ceramic nanoparticles were carried out to confirm entry of the nanoparticles into the cells in place of free DOX or prematurely released doxorubicin. The fluorescent tagged particles were then added to U2OS cells in presence of media at concentrations like that considered for cytotoxicity assays. Post 4 h of incubation, fluorescent microscopy demonstrated DOX-BG ceramic particles distributed throughout the cells even at

lower concentrations (Figure 3.39). In fact, the intensity of fluorescence was observed to increase with increase in concentration of the DOX-BG ceramic particles (Figure 3.9a). In order to quantify the number of nanoparticles present in cells, FACS based estimation was carried out and results have been provided in Figure 3.9b. As observed, DOX-BG ceramic nanoparticles were delivered to the cells effectively even at lower concentrations (delivery to ~45% cells at lowest considered concentration (10 μg/ml)). Cellular uptake increased significantly (p<0.05) with increase in concentration of DOX-BG ceramic treatment when compared to lower concentrations.

Such high cellular uptake has been reported in earlier studies as well for DOX-silica nanoparticles[96,101] and can be attributed to uptake through cellular endocytosis mechanism [125]. In fact, both silica and bioactive glass-ceramic nanoparticles have high binding affinity towards cancer cells lines. This may account for high uptake of the DOX-BG ceramic nanoparticles and the corresponding high cytotoxicity observed for most concentrations [96,125,126].

3.3.8 Conclusion

In this study, we report a one-pot synthesis method for DOX-BG ceramic nanoparticles through a bio-inspired method. Due to no calcination, the bioactive glass-ceramic nanoparticles can retain the DOX while being mesoporous at the same time. Besides, the DOX-BG ceramic nanoparticles can exhibit higher and sustained drug release at acidic pH when compared to neutral pH. The bioactive DOX-BG ceramic nanoparticles show superior activity against osteosarcoma cell lines when compared to free DOX probably due to endocytosis mediated cellular uptake of the nanoparticles when compared to diffusion meditated entry of free DOX. The DOX-BG ceramic nanoparticles promote higher cytotoxicity in cancer cells when compared to non-cancerous cell line. We are currently involved in exploring the mesoporosity of the DOX-BG ceramic nanoparticles for further encapsulation of different drugs externally so as to develop multi-drug nano-platforms or to carry out further functionalizations for active

targeting for enhanced specificity. This should allow lowering of the side effects observed in case of non-specific accumulation of DOX as well as broaden its narrow therapeutic index while enhancing its bio-availability.

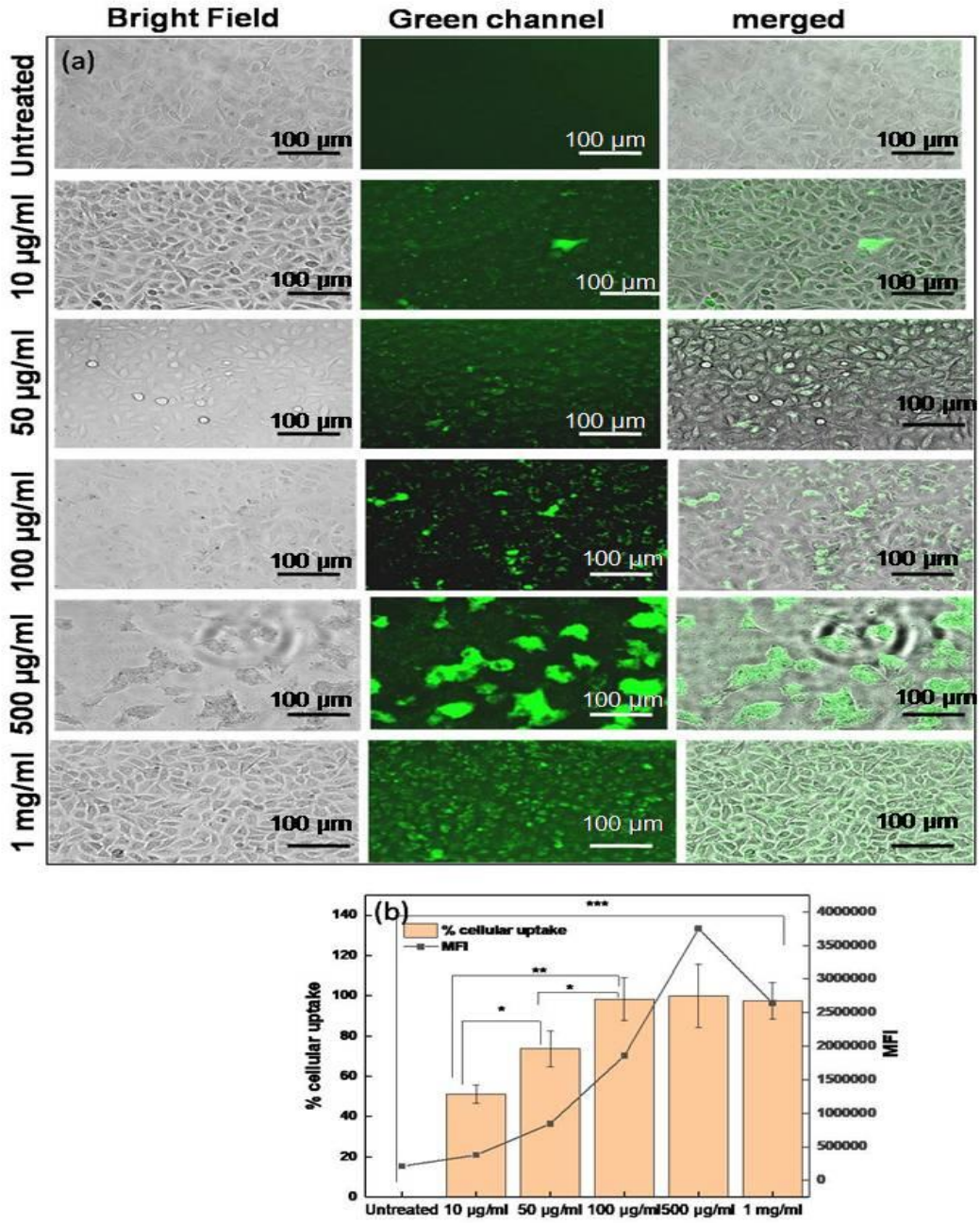

Figure 3.9: Cellular uptake studies of 0.75 DOX-BG ceramic nanoparticles on U2OS cell line through fluorescent microscopy, image scale- 100 µm (a) and quantitative uptake analysis through FACS (MFI-Mean Fluorescent Intensity) (b). Statistical significance is obtained as p-values ≤ 0.05.

CHAPTER 4

Bioinspired synthesis of bioactive glass nanocomposites for hyaluronic acid delivery to bone and skin

4.1 Introduction

Hyaluronic acid (HA) finds widespread applications in pharmaceutical, medical, cosmetic and nutritional industries [127]. Its applications range from ophthalmology, arthritis, skin diseases, wound healing, bone growth, and wound repair in medicine to being a key ingredient in skin-based applications for maintaining skin elasticity, hydration and smoothness[127]. Therefore, it is commonly found in skin serums, creams, shampoos, conditioners and other products. HA can vary in molecular weight from kilo to mega Daltons (kDa to MDa), and its application varies across multiple fields based on its size. However, the majority of formulations consists of high molecular weight HA, which is expected to have a market value of approximately USD 15.48 billion by 2027 [128].

One limitation of using high molecular weight hyaluronic acid (HMW-HA) (>600 kDa) for non-invasive topical and transdermal applications is its large size [129]. HA is composed of linear repeating disaccharide units of β-1,3-N-acetyl glucosamine and β -1,4- glucuronic acid, and is densely packed with hydroxyl, carboxyl and amide groups [127]. Several studies have attempted to deliver HA as cargo topically across a range of molecular weights using techniques such as reverse micelle formation [130], transferosomes, nanocomposites [131], liposomes [132], ionic liquids [133], peptides [134], and polyion complexes [135] as well as physical methods like iontophoresis, ultrasound, microneedles, and CO_2 laser. Various mechanisms for delivering HA to the skin, such as hydration of skin barriers, hydrophobic interactions, receptor-mediated uptake, and induced viscoelasticity [129], have been reported.

However, most delivery approaches rarely use high molecular HA for non-invasive delivery to normal untreated skin. Thus, there is a constant need to deliver high molecular weight HA non-invasively which can penetrate the layers of the skin or be delivered systemically through access to blood vessels below the dermis. One approach to delivering HA is by developing various nanocomposites. Bioactive glass (BG) is an attractive biomaterial due to its biocompatibility, biodegradability, and regenerative properties for hard and soft tissues [25,75,136–139]. Developed by Hench in the 1960s [140], bulk Bioglass® 45S5 is an FDA-approved biomaterial that has demonstrated osteo-integrative and osteo-regenerative properties, as well as applications in soft tissue [141]. Additionally, nano-sized BG can serve as a potential delivery vehicle for systemic administration and as an integrative material in implants [25,142]. Components of BG generally include silicon dioxide (SiO_2), calcium oxide (CaO), sodium oxide (Na_2O) and phosphorous pentoxide (P_2O_5). Due to its unique properties such as hollow/mesoporous pore structure, sustained drug release, and the ability to deposit bone-like hydroxycarbonate apatite (HCA) nano-crystals, BG nanocomposites have gained significant research attention for systemic delivery of a range of drugs and biomolecules [52,80,143,144].

The synthesis of BG using HA as template (BGHA) was carried out using a bio-inspired route. This novel approach allows synthesis of BGHA nanocomposites without altering the structure of HA. Traditional methods for BG nanoparticle synthesis, such as the sol-gel approach, often involve non-green solvents and high-temperature calcination (>600°C). These methods pose challenges when incorporating temperature-sensitive molecules like HA in BG and maintaining their stability [145,146]. In contrast, the bioinspired method uses Tris buffer as a green alternative, enabling the inclusion of biological molecules like HA during synthesis in a one-step one-pot process. This method efficiently produces mesoporous bioactive glass and avoids thermal stress on HA within the resulting BGHA nanocomposite. In this bio-inspired reaction, the hydrolysis and condensation of Tetraethyl orthosilicate (TEOS), the primary precursor of

BG, are induced by Tris buffer in the presence of HA. HA , with its dense hydroxyl and carboxylic acid groups, present in HA, provides multiple nucleation sites for the hydrolyzed precursors of BG, facilitating the formulation of BGHA nanocomposites [38,147]. Once the BGHA nanocomposites are successfully formed, another formulation is designed with surface-functionalized HA through covalent linkage, referred to as HA-BGHA. This formulation aims to demonstrate the function of the mesoporous BGHA nanocomposites as a delivery device for chemically conjugated high molecular weight cargo. In this case, externally conjugated HA acts as the cargo validating BGHA as a delivery device.

We report detailed physico-chemical characterization of BGHA and HA-BGHA nanocomposites, as well as studies focused on delivery across biologic barriers such as cellular and trans-cellular barriers, with a particular emphasis on an artificial skin membrane that mimics human skin architecture. These studies include *in-vitro* cellular uptake studies and a simplified model for studying transcellular movement of BGHA nanocomposites through keratinocytes which constitute 90% of the viable epidermis, in a transwell chamber. The effective retention and penetration of BGHA nanocomposites were also studied using an artificial skin membrane (StratM®) through a Franz-diffusion technique. The StratM® membrane replicates the structure of the stratum corneum (SC), dermis and subcutaneous tissue of the skin. The diffusion rates of compounds across StratM® are similar to those observed for human skin. The results of transdermal delivery vary widely depending on the study design and the type of skin membrane used (excised, live animal, chemically-stripped, or synthetic mimics). For example, there is evidence both supporting [148,149] and contradicting [150] transdermal delivery of SiO_2 nanocomposites. Recently, mesoporous silica nanocomposites were reported to exhibit skin penetration ability using deep eutectic solvents [151]. However, the ability nanocomposites to traverse both *in-vitro* and *ex-vivo* barriers of the skin and the viable

epidermis is highly desirable for candidates intended for topical and transdermal applications [134,152]

Prior to this study, there were limited investigations on the use of BGHA nanocomposites for delivering HA. Additionally, the bio-inspired method has not been utilized before for synthesis of BGHA nanocomposites nor have studies like transwell or Franz diffusion chamber assays been done for such composites. Overall, this proof-of-concept study establishes the ability of the BGHA nanocomposites to penetrate across experimental cellular and skin tissue barriers. Most studies that combine HA and BG focus on using HA as a targeting mechanism for anti-cancer therapies [153] or as scaffolds for tissue engineering applications [154]. This leaves room for studying the potential of BGHA nanocomposites for delivering HA in a minimally invasive manner.

4.2. Materials and methods:

4.2.1 Materials:

For the synthesis of bioactive glass (BG), hyaluronic acid (HA) (750-1000 KDa) (Sigma, CAS no. 53163) and Bioglass® precursors, namely tetraethyl orthosilicate (TEOS), triethyl phosphate (TEP), sodium acetate (NaAc), and calcium acetate monohydrate (CaAc), were obtained from Sigma-Aldrich, USA. Hank's Balanced Salt solution (used as simulated body fluid (SBF)) was purchased from Sigma-Aldrich, USA and used for *in-vitro* bioactivity test. For all experimental work, Milli-Q water was used. For fluorescent tagging, FITC (Sigma) was used while FITC-HA was procured from Sigma.

Preparation of buffer solutions: Reactions were carried out in 30 mM TRIZMA® buffer (pH 8.5) containing 1.82 g/l TRIZMA® HCl and 2.22 g/l TRIZMA® base dissolved in Milli-Q water. All cellular experiments were carried out using a PBS solution (pH 7.4) containing 1.78 g/l sodium hydrogen phosphate and 0.27g/l of sodium dihydrogen phosphate dissolved in Milli-Q water.

Cell culture: Human Osteoblast like Osteosarcoma cell line (U2OS) was obtained from Nation Centre for Cell Science (NCCS) Pune, India and immortalized human keratinocytes (HaCaT) were a kind gift from Dr. T.N. Vivek (CSIR-IGIB, New Delhi, India). Cell culture media DMEM-F12 and fetal bovine serum (FBS) were procured from Sigma and Invitrogen, respectively.

4.2.2 Method:

Preparation of the bioactive glass nanocomposites (BGHA): HMW-HA was added to a 30 mM TRIZMA® buffer solution at pH 8.5 (10 mM) to obtain a template concentration of 0.25 mg/ml to 1 mg/ml (0.25 mg/ml, 0.5 mg/ml, 0.75 mg/ml, 1 mg/ml separately). The solution was placed on a magnetic stirrer set at 500 rpm and at 37 °C. Once the HA is completely dissolved, precursors of bioactive glass, such as TEOS (486.5 mg) for silica, TEP (50 mg) for phosphate, NaAc (318 mg) for Na, and CaAc (250.5 mg) for Ca, were added stepwise at an interval of 30 minutes. After overnight incubation on a magnetic stirrer (500 rpm, 37 ºC), the composites were extracted through centrifugation at 13000 rpm for 5 min. The obtained particles were washed with Milli-Q water and dried in an incubator set at 37 °C. Once dried, the particles were stored in desiccators. We have named BGHA particles as 0.25 BGHA, 0.5 BGHA, 0.75 BGHA and 1.0 BGHA according to the concentration of HA used as a template in the reaction mixture (0.25 mg/ml, 0.5 mg/ml, 0.75 mg/ml and 1.0 mg/ml respectively). In this manuscript, for most studies (except thermal stability (Thermogravimetric Analysis, TGA), porosity (Brunauer-Emmett-Teller, BET) and rheology experiments), 0.25 BGHA has been used unless otherwise mentioned. Hence, 0.25 BGHA has been mentioned as BGHA by default throughout the manuscript. In the case of template-free bioactive glass nanoparticle synthesis, a similar protocol was applied except for the presence of template HA. We observed a delay in reaction time for the formation of template-free bioactive glass particles.

Preparation of Fluorescent BGHA (FITC-BGHA) and FITC-HA externally conjugated to BGHA nanocomposites (FITC-HA-BGHA): For cellular study involving microscopy, we used two fluorescent systems (a) FITC tagged BGHA (*FITC-BGHA*) and (b) Fluorescent HA conjugated to BGHA externally *(FITC-HA*-BGHA)

(a) FITC tagging of synthesized BGHA nanocomposites (*FITC*-BGHA): To carry out fluorescent tagging, amination of BGHA nanocomposites was performed. Functionalized NH_2 groups were obtained through drop-wise addition of aminated organosilicate (3-Aminopropyl)triethoxysilane, APTES, Sigma-CAS No. 440140) (45 µL) and a small amount of TEOS (15 µL) in a reaction volume of 10 ml TRIZMA buffer with 100 mg BGHA nanocomposites at 500 rpm and 37 °C on a magnetic stirrer. The particles were obtained through centrifugation after overnight incubation. Post drying, particles were mixed with FITC in PBS (pH 7.4) under constant stirring conditions. Post overnight incubation of the particles under stirring in the dark, particles were extracted through centrifugation at 13000 rpm for 5 min, washed with Milli-Q repeatedly, and centrifuged cyclically until clear supernatant is observed. Obtained FITC tagged BGHA (*FITC*-BGHA) nanocomposites are dried in a solid bath set at 37 °C and stored in desiccators in dark conditions.

(b) Covalent conjugation of FITC-HA to BGHA nanocomposites (*FITC HA*-BGHA): This is carried out in a two-step manner:

Step 1: Amination of the synthesized BGHA bioactive glass: The method is like that mentioned for *FITC*-BGHA. The particles were checked for surface charge through zeta potential analysis for confirmation of amination.

Step 2: Conjugation of Fluorescent HA (FITC-HA) to BGHA nanocomposites: The aminated bioactive glass nanocomposites were conjugated through EDC-NHS based linkage. Briefly, 50 mg of BG-NH_2 particles were dispersed in an aqueous solution through probe sonication and

added with 200 µL of 5 mg/ml FITC-HA in a total reaction volume of 5 ml under constant stirring conditions (500 rpm). To this solution, 0.4 mg EDS and 0.6 mg NHS were added and reacted overnight under dark conditions. Particles were extracted through centrifugation, washed thoroughly with Milli-Q, and dried at RT. All steps were carried out in the dark.

4.2.3 Characterizations of the bioactive glass nanocomposites:

Once particles were formed, their size, surface charge and particle morphology were analyzed using various techniques such as *transmission electron microscopy* (TEM), *atomic force microscopy* (AFM), *dynamic light scattering* (DLS), zeta potential (net surface charge) analysis etc.

Morphological Studies: The surface morphology of both BGHA and HA-BGHA was examined using a field emission *scanning electron microscope* (FE-SEM) (Model FEI Quanta 200 F SEM, FEI company, Netherlands). All samples (0.1 mg/ml) were coated with gold and observed in the FE-SEM at an accelerating voltage of 5 kV at the required magnifications. The bioactive glass particles that formed were also visualized using a *transmission electron microscope* (TEM) (Model TALOS S, Thermo Scientific, USA) operating at an accelerating voltage of 200 kV.

Atomic Force Microscopy (AFM): The size and surface morphology of the BGHA nanocomposites were examined using an AFM (Keysight SPM5500). The nanocomposites were prepared at a concentration of 0.5 mg/ml, and 5 µl of the solution was placed on sheets of mica. The sample solution was allowed to dry at room temperature, after which imaging was performed in acoustic-AC mode using a silicon cantilever with a resonance frequency of 300 KHz and a constant force of 40 N/m. The scanning speed of the samples was set at 1 line/sec.

DLS measurements: The particle size (or hydrodynamic radius) and net surface charge (*zeta potential*) were measured using a ZetasizerNanoZS (Malvern Instrument, UK) at 25 °C, with

Milli-Q water used as the dispersant. For both assessments, the particle concentration was 0.5 mg/ml.

Zeta potential Measurement: Zeta potential (net surface charge) of HA (0.5 mg/ml), BGHA (0.5 mg/ml), HA-BGHA (0.5 mg/ml) and BGHA-NH_2 (0.5 mg/ml) was monitored using a ZetasizerNano ZS (Malvern Instruments, UK) instrument in the presence of water as the dispersing media.

Physico-chemical characterization of BGHA and HA-BGHA was carried out through FTIR, XRD, EDS, TGA, BET etc.

Fourier Transform Infrared Spectroscopy (FTIR): After synthesizing the nano-assemblies, FTIR spectra were recorded to confirm the formation of a bioactive glass network from its precursors, using a Perkin Elmer (Model Spectrum 2) spectrometer (range 4000–600 cm^{-1}, resolution 1 cm^{-1}). The FTIR analysis of BGHA (5 mg), HA (5mg), and HA-BGHA (5 mg) was carried out by pelleting with potassium bromide (KBr) in a 1:100 ratio. Template-free BG was also included in the FTIR study.

X-ray diffraction (XRD): Powder X-ray diffraction experiments were carried out on HA, BGHA, and template-free BG particles using a Bruker D4 X-ray diffractometer operating at 30 kV and 15 mA with CuKα radiation. Around 500 mg of sample was taken for all XRD studies. XRD patterns were collected in the 2θ range of 10° to 70°, with step sizes of 0.02° and a counting time of 6 s per step.

Thermogravimetric Analysis (TGA): Thermal stability of BGHA (5 mg) and HA-BGHA (5 mg) was analyzed using a Perkin Elmer thermogravimetric analyzer (Model TGA 4000). During analysis, the samples were heated from room temperature to 800 °C at a heating rate of 10 °C/min under a nitrogen atmosphere, with a nitrogen flow rate of 20 ml/min.

Energy dispersive X-ray spectroscopy (EDS): EDS, coupled with SEM set at an operating voltage of 12 kV (ZEISS EVO MA15), was used to analyze the elemental composition of

BGHA and template-free BG nanocomposites (0.1 mg). Data was reported for the average relative atomic% of Si, P, Ca, Na and C from three representative surfaces.

Brunauer–Emmett–Teller (BET) Analysis: The porosity of various BGHA nanocomposites (500 mg) was determined by nitrogen adsorption-desorption analysis at -196 °C using Microtrac BEL (Model BELSORP-max), Japan, with nitrogen as the adsorptive gas (N_2, cross-sectional area 0.162 nm^2). Before analysis, 0.25 BGHA, 0.75 BGHA, 1.0 BGHA, and template-free BG were degassed under vacuum at 200 °C for 2 h, according to the standard BET protocol. The surface area was determined using the Brunauer–Emmett–Teller (BET) equation applied to the nitrogen adsorption data obtained. The pore-size distribution was determined by the Barrett–Joyner–Halenda (BJH) method applied to the desorption branch of the isotherm.

Measurement of viscosity: A slurry of BGHA nanocomposites prepared with varying concentrations of template HA (0.25, 0.75, and 1 mg/ml) was subjected to characterization for viscosity using a stress-controlled Anton Paar Rheometer (Model MCR 702), Austria equipped with parallel-plate geometry (40 mm). Around 100 mg of each sample was used for slurry preparation. Rheology experiments were performed to map the viscosity profiles of the nanocomposites in the form of slurry with PBS (pH 7.4).

DMMB assay to determine HA amount in BGHA nanocomposites: In order to carry out the Dimethylmethylene blue (DMMB) assay, 1 mg/ml of 0.25, 0.75 and 1.0 BGHA prepared (with template(HA) concentration 0.25, 0.75 and 1 mg/ml) was suspended separately in PBS. 20 µl of the suspension was added with 200 µl of DMMB solution. The DMMB solution was prepared as reported in literature[155]. Absorbance readings were carried out using a TECAN multi-well reader (TECAN infinite M200) with a range of 450-700 nm to quantify the change in color of the added DMMB dye. The absorbance spectra were recorded and have been reported for all 3 compounds.

Bioactivity Test: In-vitro bioactivity of BGHA nanocomposites was evaluated by monitoring the formation of hydroxyapatite on the bioactive glass surface using a procedure developed by Kokubo *et al* [70]. BGHA nanocomposites were added to simulated body fluid (SBF) at a concentration of 1 mg/ml under constant shaking in an incubator set at 37 °C. The SBF solution was changed every 3 days to maintain its cationic concentration, which could otherwise decrease and hinder hydroxyapatite formation. After a pre-determined time interval, the samples were extracted through centrifugation (13000 rpm, 5 min), washed three times with Milli-Q water, and dried in an air oven at 40 °C. They were further characterized using FTIR, XRD, and FESEM analysis.

4.2.4 Cellular studies:

All cellular studies were carried out in Human osteoblast-like osteosarcoma (U2OS) and Human keratinocytes (HaCaT) as model bone and skin cell lines, respectively. Cells were cultured in DMEM-F12 media with 10% FBS and stored in a 5% CO_2 incubator at 37°C.

Cellular bio-compatibility: The *in-vitro* cytotoxicity of BGHA nanocomposites was assessed using model bone (U2OS) and skin (HaCaT) cells by performing the MTT assay at various concentrations. Both cell lines were seeded separately in 96 well-plates (*Corning*) at 10,000 cells per well. Once they reached 70% confluency, the cells were treated with increasing concentrations (10 µg/ml to 1 mg/ml) of BGHA nanocomposite suspensions prepared using sterile phosphate buffer saline (PBS). After 24 h treatment, the media was removed, and each well was washed with PBS to remove any remaining sample. To carry out the MTT assay, 3-(4,5- dimethylthiazol-2-yl)-2,5-diphenyltetrazolium bromide (MTT) was prepared in *opti-MEM* (Invitrogen) (5 mg/ml) and added to each well to obtain a predetermined concentration of 0.5 mg/ml. The plates with MTT were incubated in a humidified incubator at 37°C for 1-2 h until purple crystals could be observed through an optical microscope. Once crystals were formed, MTT was removed from each well, and dimethyl sulfoxide (DMSO) was added (100

µl/well (96-well plate)) to dissolve the formazan crystals formed as a result of MTT addition. After an hour of mixing on a dancing shaker, the solution was measured for absorbance at a wavelength of 570 nm using a multiplate reader (TECAN, Infinite® 200 microplate reader).

Cellular viability is calculated as

$$\frac{(\text{OD of the experimental samples})}{(\text{OD of the control})} \times 100$$

Untreated wells were considered as control while treated wells were referred to as experimental samples (OD-Optical density).

Cellular uptake studies: Cellular uptake studies for *FITC*-BGHA and *FITC-HA*-BGHA were carried out at increasing concentrations (10 µg/ml to 1 mg/ml) on both HaCaT and U2OS cell lines. Briefly, both cell lines were plated at approximately 20,000 cells per well in 24 well plates (*Corning*). The following day, particles were prepared in 1X PBS (pH 7.4) and added to each well for 24 h. After the incubation period, the media was removed, the wells were washed with 1X PBS, and viewed under a fluorescent microscope under bright field and green channels (*Floid* cell imaging station). For quantitative analysis, both cell lines were detached from the plates through trypsinization post 24 h treatment and analyzed through FACS (BD *accuri* C6).

Confocal microscopy: Cells (both HaCaT and U2OS) were grown on coverslips for observation of cellular uptake through a confocal laser scanning microscope (CLSM). After treating the cells with *FITC*-BGHA and *FITC-HA*-BGHA for 24 hours, the media was removed and the coverslips were washed with PBS to remove unbound samples. The coverslips were then stained with DAPI (Sigma) for visualization of the nucleus. Each coverslip was fixed with (2-4%) paraformaldehyde (PFA), and observed through confocal microscopy (*Leica* Instruments). Images were processed through LAS-X software for Windows.

4.2.4 *Transwell studies*

To carry out transwell experiments, non-coated transwells from *Corning* were seeded with HaCaT (keratinocytes) cells to form a cellular layer for determining uptake and penetration of the nanocomposites through the keratinocyte layer. Large numbers of HaCaT cells were plated in the transwells at >50,000 cells/well. The cells were allowed to grow on the transwell for two to three days until a uniform distribution of the cells could be observed under the microscope. U2OS cells were grown as a model cell line to study the uptake of BGHA nanocomposites that penetrated through the keratinocyte layers. Afterward, treatment of both classes of nanocomposites was provided to transwell chambers (10 µg to 1 mg/ml). After 24 h of incubation, samples were removed, and both HaCaT grown in the transwell chamber and U2OS cells growing in the receptor chamber were assessed qualitatively and quantitatively for cellular uptake of the nanocomposites through fluorescence microscopy and FACS, respectively. Additionally, the efficiency or robustness of the barrier was tested through the application of FITC-Dextran (100 µg/ml) which is generally impermeable to keratinocyte layers. The transwell arrangement was a proof-of-concept study to examine the penetration of *FITC*-BGHA and *FITC-HA*-BGHA through corneocyte layers of the stratum corneum in the skin.

4.2.5 Permeation study

To carry out permeability studies, both FITC-BGHA and FITC-HA-BGHA were prepared at concentrations of 1 mg/ml. The samples were applied (four periodic applications of 100 µl each) to Strat-M® membrane placed with the shiny side in contact with the donor compartment and mounted on Franz diffusion cells with a donor area of 0.64 cm^2 and a receptor volume of 5.0 ml. Strat-M® membrane (EMD Millipore, MA, USA) does not require any pre-treatment and thus was used immediately after removing it from the packaging. The membrane was placed in the Franz cells, and the receptor compartment of each cell was filled with filtered PBS (pH 7.4) and maintained at 37 °C under synchronous continuous stirring using magnetic stirrers at 500 rpm. The diffusion cells were allowed to equilibrate at 37 °C for 15 minutes.

Then, at time zero,100 µl of the formulation prepared in PBS (pH 7.4) was added to the donor compartment of each Franz diffusion cell either at once, comprising the full dose, or the dose was divided into multiple applications. Multiple applications were carried out to avoid saturating the membrane with high doses at once, and a comparison was made between the two modes of application after completion of the incubation period (24 hours). Post-incubation, the membrane was extracted from the Franz cell, washed with PBS, and digested using dimethylformamide (DMF), referring to it as the membrane solution. Fluorescence intensities of all solutions (wash solution, membrane solution, and receptor solution) were recorded at an excitation wavelength of 490 nm and an emission wavelength of 520 nm corresponding to FITC-HA-BGHA or BGHA-FITC fluorescence.

4.2.6 Statistical analysis

Statistical analysis involved conducting unpaired t-tests to compare the control and treatment groups, with significance denoted by a *p*-value exceeding 0.05 (95% confidence interval). Graphs were generated using Origin® software, and Graphpad Prism® for Windows was employed to perform the statistical analysis.

4.3 Results and discussion:

4.3.1 Preparation of the hyaluronic acid-bioactive glass (BGHA) nanocomposites:

A detailed description of the design and synthesis of the BGHA nanocomposites is provided in section 2.2 of the materials and methods. It is worth mentioning that BGHA was synthesized in the presence of multiple concentrations of HA (0.25mg/ml, 0.5 mg/ml, 0.75 mg/ml and 1 mg/ml) in TRIZMA buffer. However, we found that BGHA synthesized with 0.25 mg/ml HA had physico-chemical and biological properties that were ideal for our studies. Therefore, we have primarily used 0.25 BGHA in most studies unless otherwise mentioned and has been mentioned as BGHA by default throughout the manuscript. Particles that were synthesized

without the presence of HA have been referred to as template-free BG throughout the manuscript.

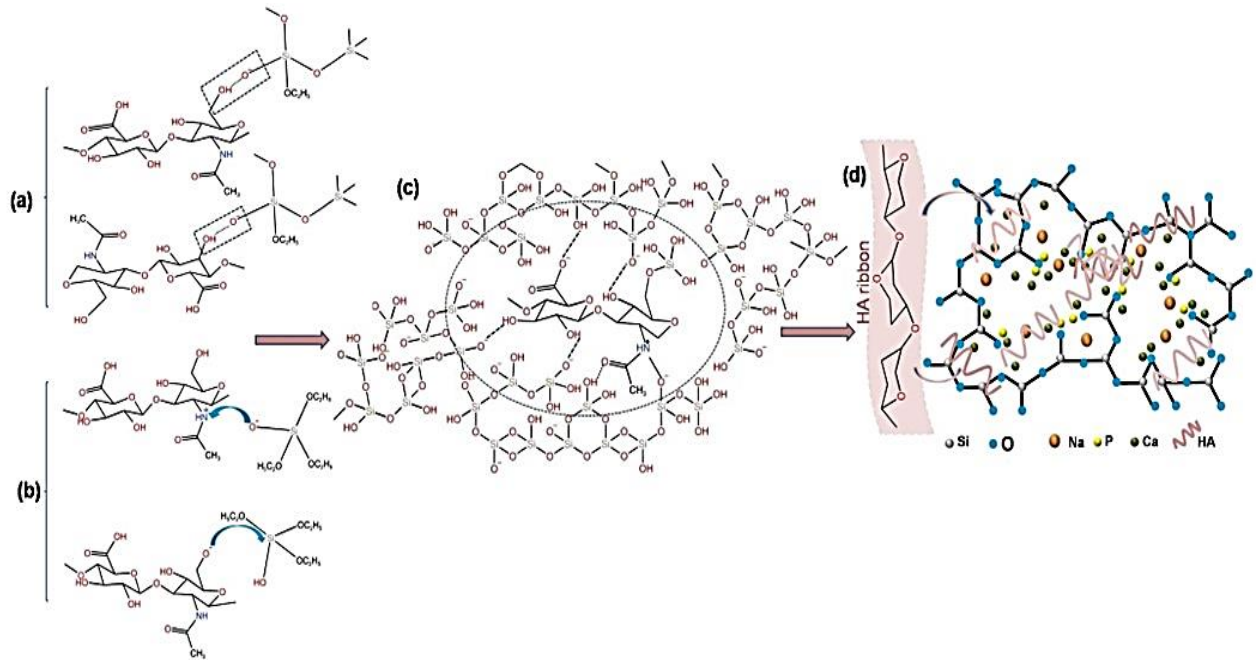

Figure 4.1: Possible mechanisms of interaction of HA with BG network through (a) Hydrogen bonding and (b) chemical bonding. (c) Overall interaction of HA with silica network and (d) formation of BG network structure bridged with HA.

In aqueous solutions, HA adopts a β-sheet tertiary conformation through a combination of intra- or inter-molecular hydrophobic and hydrogen bond interactions. These interactions facilitate the formation (aggregation) of HA networks, which are considered essential for assembling nanosystems. Furthermore, HA acts as a backbone and binding factor during the process of self-assembly [127,156].

Interactions between HA and TEOS include covalent bonding, H-bonding, ionic interactions and van der Waals forces (Figure 4.1). Due to these physicochemical interactions, primary silica particles nucleate on HA chains, leading to the formation of dense silica clusters. Chemical bonding may occur due to the interaction of deprotonated silane with amino functional sites (-N<) on the HA molecule (Figure 4.1b). In such interactions, deprotonated silane acts as a nucleophile and initiates a controlled silica network chain reaction for the

assembly of other silane molecules (Figure 4.1c). Protonated silica may also act as an electrophile, leading to the assembly of other silane molecules (Figure 4.1c).These processes lead to the formation of secondary and tertiary nano-assemblies, which can accommodate phosphates and metal cations (Ca^{2+} and Na^{+}) upon the addition of TEP, CaAc, and NaAc, respectively, into the network via electrostatic and coordinate bonding interactions. The presence of these additives acts as network-formers and modifiers in the final BGHA structure (Figure 4.1d). In nature, silicon is observed to be associated with glycosaminoglycans through ether or ester-like linkages (C-O-Si or C-O-Si-O-Si) bonds. The C-O-Si bond has also been reported in the presence of Tris buffer during the initiation of condensation and hydrolysis of alkoxysilanes (TEOS) in bio-inspired studies [157,158]. Additionally, the presence of glycopyranose rings in HA may lead to interactions with silica oligomers through polar or hydrogen bonding interactions. The entrapment of HA in the bioactive glass network acts as a bridge between silicon oxides in the complex [158]. Although it seems pertinent to state that the charged moieties in HA predominantly lead to the condensation of BG precursors, the role of negatively or neutrally charged groups in the process is yet to be fully understood.

4.3.2 Size and morphology characterization of BGHA nanocomposites

The particles were reported to have an average hydrodynamic radius of 190 ± 27.19 nm through DLS analysis (Fig 2a). However, the size histogram indicated that most particles were in the range of <100 nm. The PDI (polydispersity index) was relatively high, suggesting possible agglomeration in the solution. TEM, AFM, and SEM images showed that particles were spherical and below 100 nm in size (Figure 4.2b, c, d). The size and morphology of the particles in the bio-inspired route depended on various factors, such as the concentration of precursors (mainly TEOS and CaAc), reaction time, and the nature of the template[159]. Other factors that could affect the process include the presence of Tris buffer and the pH of the solution [28,157,158].The presence of the template reduced the time required for particle formation.

(particles prepared without a template typically showed little deposition after overnight incubation). All primary studies and characterizations were reported for BGHA prepared at an HA concentration of 0.25 mg/ml (0.25 BGHA) unless otherwise mentioned. The particle yield increased with increasing HA concentration as a template.

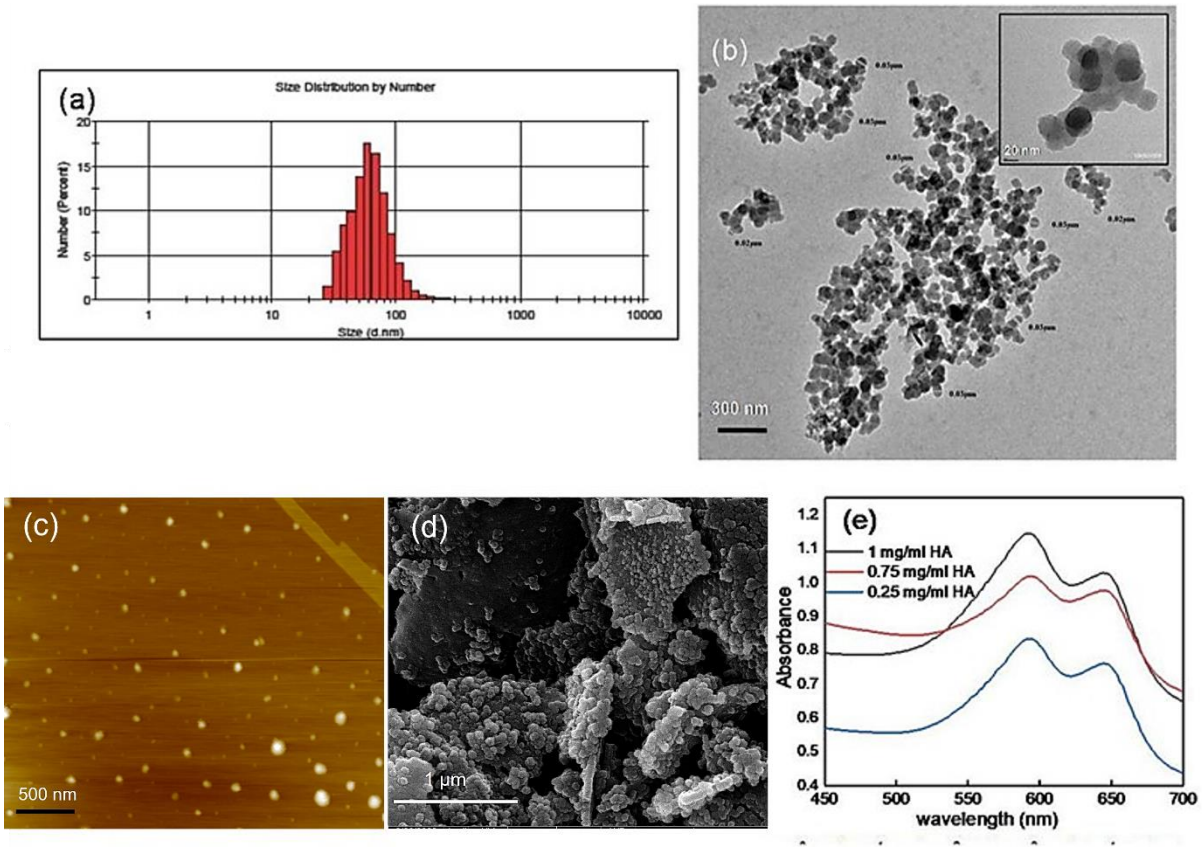

Figure 4.2: BGHA size and morphology through (a) DLS, (b) TEM, (c) AFM, and (d) FE-SEM; Presence of HA in BGHA synthesized with increasing HA concentration as template detection through (e) DMMB assay

The presence of hyaluronic acid in the BGHA nanocomposites was assessed using the DMMB assay. Although DMMB is known to predominantly bind to sulfated GAGs, it can also bind to glycosaminoglycans with low sulfation [160]. It was observed that the presence of hyaluronic acid in the BGHA complexes increased with an increase in template concentration in the range of 0.25 to 1 mg/ml, suggesting possible template retention based on the initial concentration of

the template (Fig 2e). Similar effects have been observed in our method for other templates [41,161].

4.3.3 Physico-chemical characterization of BGHA nanocomposites

FTIR: FTIR analysis was conducted on template-free BG, native HA and BGHA nanocomposites, and the resulting graph is presented in Fig 3a. The purpose of synthesizing particles without the presence of template HA was to observe the effect of HA on the physical characteristics of BG when compared with BGHA. For template-free BG, a broad peak at 3400 cm^{-1} indicated O-H stretching and bending from bound water molecules. Two sharp peaks were visible at 1408 and 1548 cm^{-1}, corresponding to C-H bending from half-hydrated or monohydrated TEOS or from CaAc and anti-symmetric C-O stretching. A peak at 1013 cm^{-1} corresponded to the Si-O-Si bond, indicating the formation of a silica network. However, the intensity of this peak was low, indicating inadequate network formation. The lower presence of silica in template-free BG was also confirmed through EDS analysis (Fig 4). Peaks at about 460, 468, 612, and 650 cm^{-1} could correspond to either SiO_4^- or PO_4^{3-}. The FTIR graph of template-free BG resembled that of highly mineralized glass structures with a heterogeneous nucleation point for crystallization. The long-term presence in Tris buffer may have also led to the formation of hydroxyapatite crystals in template-free BG.

When analyzing the FTIR peaks of free HA, a broad absorption peak at 3400 cm^{-1} indicated -OH and -NH stretching, while a small doublet at 2900 and 2885 cm^{-1} suggested asymmetric and symmetric $-CH_2$ vibrations. The peaks at 1157 and 1043 cm^{-1} corresponded to typical carbohydrate groups.

The FTIR graph for BGHA displayed peaks at 3426, 2906, and 2836 cm^{-1}, which may result from the presence of -OH bonds in the nanocomposites (or from $Si\text{-}OH^-$ on its surface), the template, or different modes of water. Significantly, the bands at 2906 and 2836 cm^{-1} (antisymmetric and symmetric vibrations of $-CH_2$, respectively) could correspond to HA

entrapment in the assembly. Furthermore, the peak at 1634 cm^{-1} (COO^- stretching of amide I) had shifted 20 cm^{-1} compared to native HA, indicating chemical bond formation between HA and TEOS. The peak at 1408 cm^{-1} (carbonate group from HA (δCH and δOH) may have also appeared due to the retention of the template HA. BG's characteristic peaks at 1094 cm^{-1} and 948 cm^{-1}, corresponding to signature Si-O-Si asymmetric stretching and bending vibrations, respectively, were also observable in BGHA [39].The peak at 800 cm^{-1} corresponded to $Si-O^-$ interaction and the presence of non-bonding oxygen or Si-O-Ca interaction [162]. The peaks in the 450 to 550 cm^{-1} range corresponded to Si-O bending vibration and the vibration from the presence of cations like Na^+ or Ca^{2+} in BGHA. Additional bands in this region also corresponded to PO_4^{3-} vibrations present in the BG structure. Based on the FTIR analysis, we observed the possible existence of both physical and chemical interactions of BG with HA, as described in Figure 4.1.

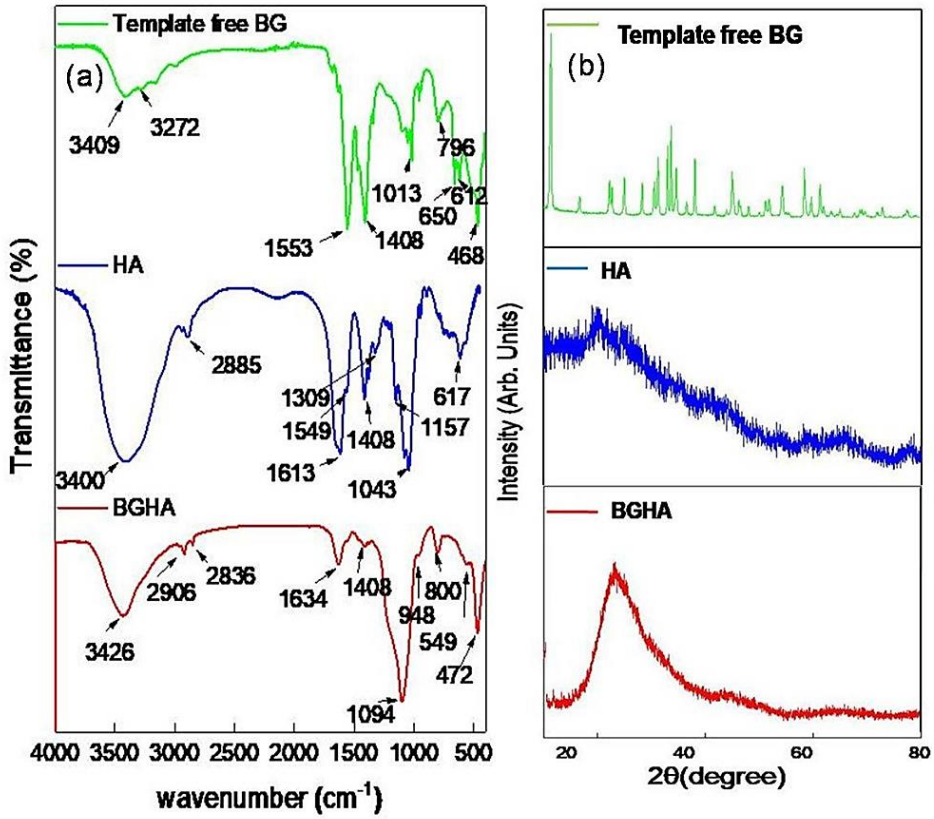

Figure 4.3 : (a) FTIR spectra and (b) XRD patterns of template free BG, native HA and BGHA nanocomposites

XRD: The XRD diffractogram for template-free BG (as shown in Figure 4.3b) displays multiple diffraction maxima at various *2θ* degrees, suggesting a crystalline nature. Upon checking against the JCPDS directory, it was found that the sample contained a mixture of two or more crystals (including JCPDS: 01-084-0151 $Na_3Ca(SiO_3)(PO_4)$ Sodium Calcium Silicate Phosphate; JCPDS 00-031-0582 $H_2Si_2O_5$, Hydrogen Silicate; JCPDS: 00-024-0033 $Ca_5(PO_4)_3(OH)$, Hydroxyapatite).The absence of HA leads to nucleation and formation of silica nanospheres through self-condensation of TEOS in the presence of Tris buffer. However, due to the lack of sufficient nucleating points, particle formation is delayed, and the existence of other cations (Ca^{2+}, Na^{+}) and phosphate ions from other precursor molecules (TEP) during the reaction leads to heavy mineralization of the primary or secondary particles. Consequently, we observed various diffraction patterns corresponding to multiple crystal structures of Si, Ca, P, and Na.

In contrast, both HA and BGHA are amorphous in nature, as indicated by the lack of distinct diffraction maxima in both samples. HA is a carbohydrate polymer of glycosaminoglycans (GAGs) and is naturally non-crystalline [163]. The broad diffraction maxima between 15 to 35 *2θ* degrees is a characteristic pattern observed in amorphous bioactive glass [41,76]. From the XRD analysis, it can be understood that the presence of a template like HA in BGHA may have led to the randomized deposition of precursors of bioactive glass along with the presence of network modifiers (cations and phosphates), resulting in the formation of an amorphous BGHA composite [38,40,41]. Moreover, sodium hyaluronate has been reported in the past to act as a template for temporarily stabilizing bioactive amorphous calcium phosphate [164]. The amorphous nature of BG- based composites is highly desirable for biologic applications, as it is safer and more biodegradable when administered in the body. Additionally, amorphous BG has been reported to demonstrate better bioactivity than crystalline Bioglass® [165].

EDS: Comparison of the elemental composition between template-free BG and BGHA has been provided in Figure 4.4. In the case of BGHA, the analysis using EDS indicates the presence of all constituents of BG, namely Si, O, Ca, P, and Na. The higher atomic weight percentage of Si and O in BGHA suggests the formation of Si-O-Si or $Si\text{-}O^-$ groups, which mainly constitute the BG network. The binding of cations, such as Ca^+ and Na^+, in BG mostly occurs through ionic interactions with negatively charged Non-Bonding Oxygens (NBOs) in the silica structure. The presence of PO_4^{3-} is dependent on coordinate linkages with $Si\text{-}O^-$ groups. The lower presence of Na^+ and Ca^{2+} in BGHA when compared to template-free BG may be due to the possible removal of the salts during washing steps [166]. Additionally, the presence of HA during the inception and growth of the BG nanocomposites may have occupied NBO sites, hindering the retention of cations through H-bonding interactions with protonated hydroxyl and carboxylic groups of HA. Furthermore, if the surface of BGHA is coated with excess HA from the surrounding reaction media, it can shield signals from underlying components of BG.

A higher proportion of cations could be observed in the case of template-free BG. However, the amount of silica was lower than all other constituents in template-free BG, indicating inadequate formation of the silica network in the Tris buffer in the absence of HA prior to the addition of TEP, CaAc, and NaAc. Moreover, a longer reaction time led to increased mineralization of the silica structures, resulting in comparatively higher amounts of Ca, Na, and P in template-free BG. These findings are consistent with the observed FTIR and XRD outcomes.

TGA: The TGA thermogram indicated that BGHA is thermally stable across the range of temperatures applied (0 to 800 °C) (Figure 4.4d). In 0.25 BGHA samples, an initial weight loss is observed until 100°C, which may be attributed to dehydroxylation of the Si-OH groups on the surface of silica, loss of bound water, and degradation of template HA.

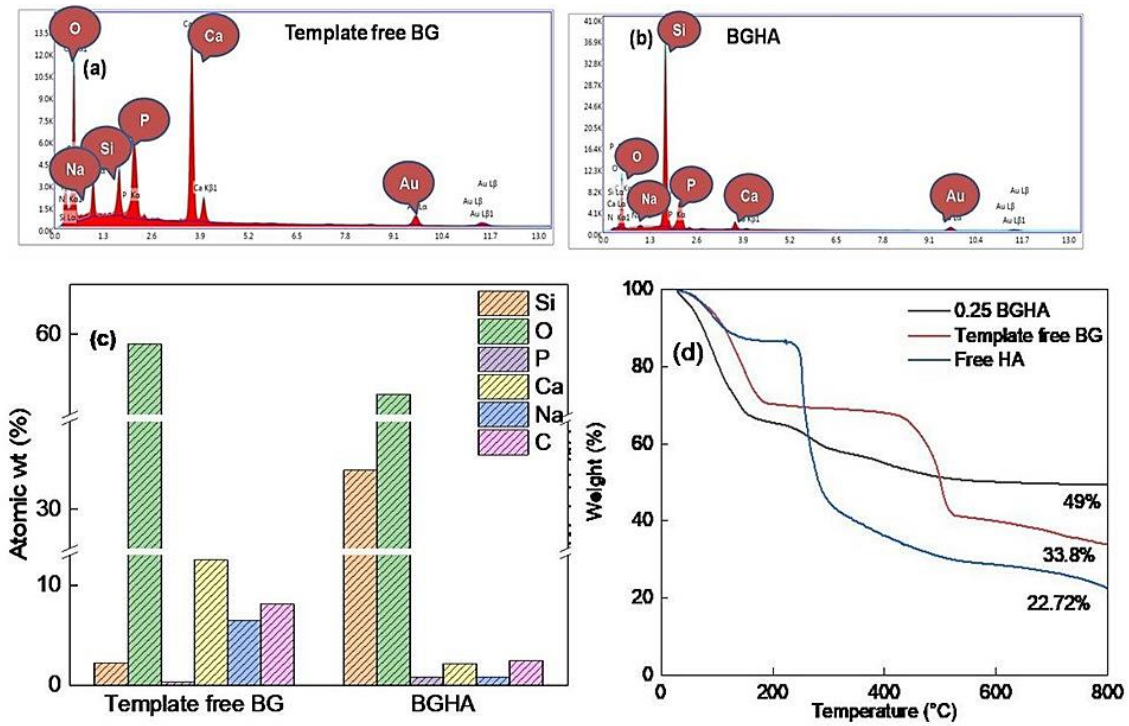

Figure 4.4 : (a, b) EDS, (c) relative atomic wt. (%) and (d) TGA thermograms for template free BG and BGHA.

The wide weight loss curve observed in BGHA from 200 to 400 °C is mainly due to the thermal decomposition of HA (which exhibits an exothermic peak at 240°C in DSC as shown in the literature[163]) into fragmented carbonized residues. Upon closer observation of the curve, two stages of weight loss (190 °C to 260°C; and 270 °C to 400°C) characteristic of two-step disaccharide degradation within this temperature range[167] are revealed. The weight losses observed in these stages are lower than those of HA in its natural state [163]. This can be attributed to the shielding effect of the bioactive glass network to the entrapped HA. The characteristic pattern observed in the BGHA TGA curve indicates successful hybridization of the BG network with HA. The majority of BG synthesized through the bio-inspired route exhibit thermal stability until 800°C. For template-free BG, gradual weight loss observed until 200°C can be attributed to the evaporation of adsorbed water, while a rapid weight loss could be observed at 500-600°C indicating shrinking due to the glass transition (which occurs at 550°C for Bioglass®)[168] or decomposition of crystalline calcium silicate-based minerals (also

observed in XRD) [169]. In both cases, the remnant weight (wt. (%)) is due to the presence of inorganic minerals and organic carbon.

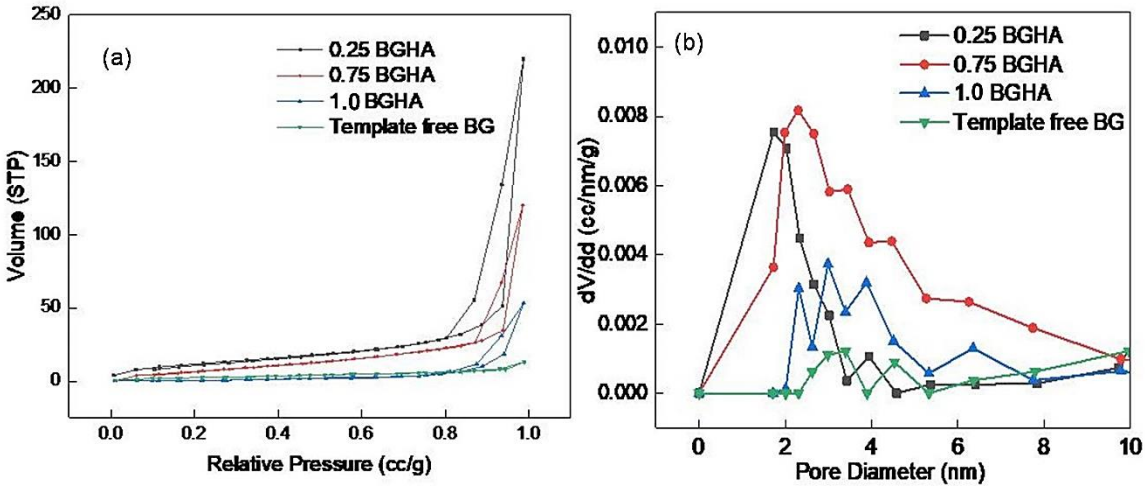

Figure 4.5 : (a) Nitrogen adsorption-desorption isotherm and (b) graph for pore size distribution of template free BG and BGHA prepared with increasing template concentrations.

BET: N2 adsorption/desorption analysis was used to characterize the particle surface of BGHA and template-free BG. The effect of HA on the pore structure of BGHA was observed by synthesizing particles with increasing concentrations of the template (0.25, 0.75, and 1 mg/ml). All BGHA particles exhibited a mesoporous nature, characterized by a type V isotherm and hysteresis loop 3 (Figure 4.5a). This is typical of micro-mesoporous systems and reveals the slit-like mesoporous nature of the nano-assembly shell. The presence of a type V isotherm indicates the formation of an irregular network due to nanoclusters of BG formed on the HA backbone as a result of controlled hydrolysis of TEOS at pH 8.5 [37].

As the concentration of HA increased, the extended HA network resulted in fewer clusters in proximity to each other, leading to a decrease in interconnected mesoporous channels in the formed particles (Table 4.1). Moreover, the decrease in surface area and pore volume with increasing template concentration indicated that HA was not only present entrapped within the nanoparticle but also on the surface of the nanoparticle as an external layer [170]. The probability of the latter is high because the surface of the BG nanocomposites is rich in different types of

silanol groups, including isolated (-Si−OH), vicinal (HO−Si−O−Si−OH), and geminal (-$Si(OH)_2$) silanols. Silanols can serve as both hydrogen bond donors and acceptors, facilitating hydrogen bonding with molecules like HA [171].

Pore characterization	0.25 BGHA	0.75 BGHA	1.0 BGHA	Template free BG
Pore Volume (cc/g)	0.351	0.198	0.09	0.022
Surface area (m^2/g)	62.208	50.698	14.682	11.527
Pore Diameter (nm)	23.846	2.298	23.96	2.987

Table 4.1: Surface characterization of BGHA and template free BG nanoparticles through Brunauer–Emmett–Teller (BET) analysis

The co-condensation of silica nanocomposites in the presence of drugs or biomolecules has previously been observed to affect the pore volume and surface area of the formed nanocomposites, similar to this case [37,108,161]. Lowering of pore volume and surface area has been observed to occur with an increase in template or associated biomolecule concentration in such reactions [172].

Measurement of viscosity of slurry of BGHA: To investigate the viscosity of BGHA nanocomposites, we synthesized particles with increasing concentrations of HA (0.25 mg/ml, 0.75 mg/ml, and 1 mg/ml). After preparation and drying, we created a slurry of 5-10 mg of nanocomposites using PBS (pH 7.4). Figure 4.6b shows that the viscosity decreases with increasing shear rates for all samples. However, the degree of viscosity loss is inversely proportional to the concentration of the template (HA) in the nanocomposite. The decrease in viscosity with increasing shear rate indicates the breakage of intermolecular hydrogen bonds of HA and deformation of HA molecular chains [173]. Moreover, the decrease in viscosity is reversible when the shear rate is decreased. The shear stress vs. shear rate graph (Figure 4.6c)

demonstrates greater shear thinning property for BG nanocomposites prepared using HA at various template concentrations [174].

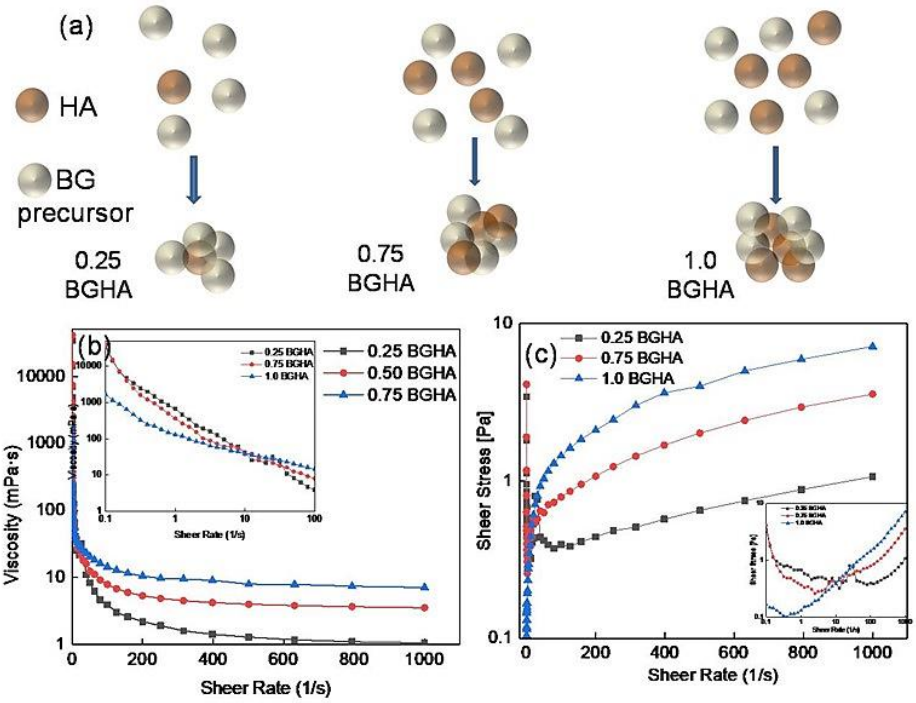

Figure 4.6 : (a) Graphical representation, (b) measurement of viscosity with increasing shear rate and (c) shear stress with increasing shear rate of BGHA nanocomposites prepared with increasing HA concentration (0.25, 0.75 and 1 mg/ml) (insets shows point of intersection for all three samples from 0.1 to 100 sheer rate (b) and 0.1 to 1000 sheer rate (c))

The viscosity properties of BGHA nanoparticles at the highest template (HA) concentration may be attributed to intermolecular interactions among HA polymers hanging from nanocomposites in the slurry. Shear thinning properties are essential for the injectability of formulations during viscosupplementation. It is possible that an excess amount of HA on the surface of BGHA could have led to further enhancement of the viscosity of the nanocomposites. Moreover, the increase in shear stress with an increase in stress rate suggests possible network formation, corroborating the presence of increasing HA on the particle surface. Evidence of surface HA in the case of BGHA can already be observed in DMMB (Figure 4.2e), TGA (Figure 4.4d), EDS (Figure 4.4) and BET (Figure 4.5) analyses.

HA-based compositions are widely used as viscosupplements in the treatment of osteoarthritis [174]. It has also been suggested that compacting HA in nanocomposites leads to an increase in HA concentration but a decrease in viscosity compared to free HA formulations [175]. Shear stress was observed to increase linearly with shear strain for all compounds. Nanocomposites with viscosity in solution offer several advantages, including providing lubricating properties to (a) hydrogels reinforced with them, (b) enhanced penetration across various biologic barriers, and (c) treating various diseases.

4.3.4 Surface grafting of HMW FITC-HA on the surface of BGHA nanocomposites (FITC-HA-BGHA) for assessment as a delivery device

During the one-pot co-condensation method for HA like the bio-inspired reaction described in this study, there is a possibility of condensation or retention of fragmented HA from the solution in the formed nanocomposites, which may exhibit effects different from those of native HA[174]. Therefore, we externally grafted the nanocomposites with full-length HA (FITC tagged). The reaction involved the formation of an amide bond between the amine groups of aminated BGHA and the carboxylic groups of native HA [170].

To characterize the BGHA nanoparticles conjugated with HA externally, multiple techniques such as TEM, DLS, Zetasizer, TGA, etc., were employed, and the results are presented in Figure 4.7. Although no significant increase in the size of the nanocomposites could be observed from TEM images, the appearance of an amorphous-like external layer may indicate the formation of a coating of HA [170]. DLS results indicated an increase in the hydrodynamic radius of HA-BGHA (479.6 ± 14.93 nm) compared to BGHA (Figure 4.7c), which can be attributed to the water retention property of HA coated on the nanoparticle surface.

The change in the net surface charge of the BGHA nanocomposites was recorded during each step of the synthesis process of HA-BGHA (190 ± 27.19 nm) (Figure 4.7d). It was observed that while BGHA nanocomposites had a surface charge of -21 mV, the amination of the BGHA

led to a positive surface charge of 12 mV. The conjugation of HA onto the surface of the aminated BGHA nanocomposites was confirmed through the reversal of surface charge to -19 mV. Compared to native BGHA, the surface charge for HA conjugated BGHA is lower, probably due to remnant non-conjugated -NH_2 groups on the surface.

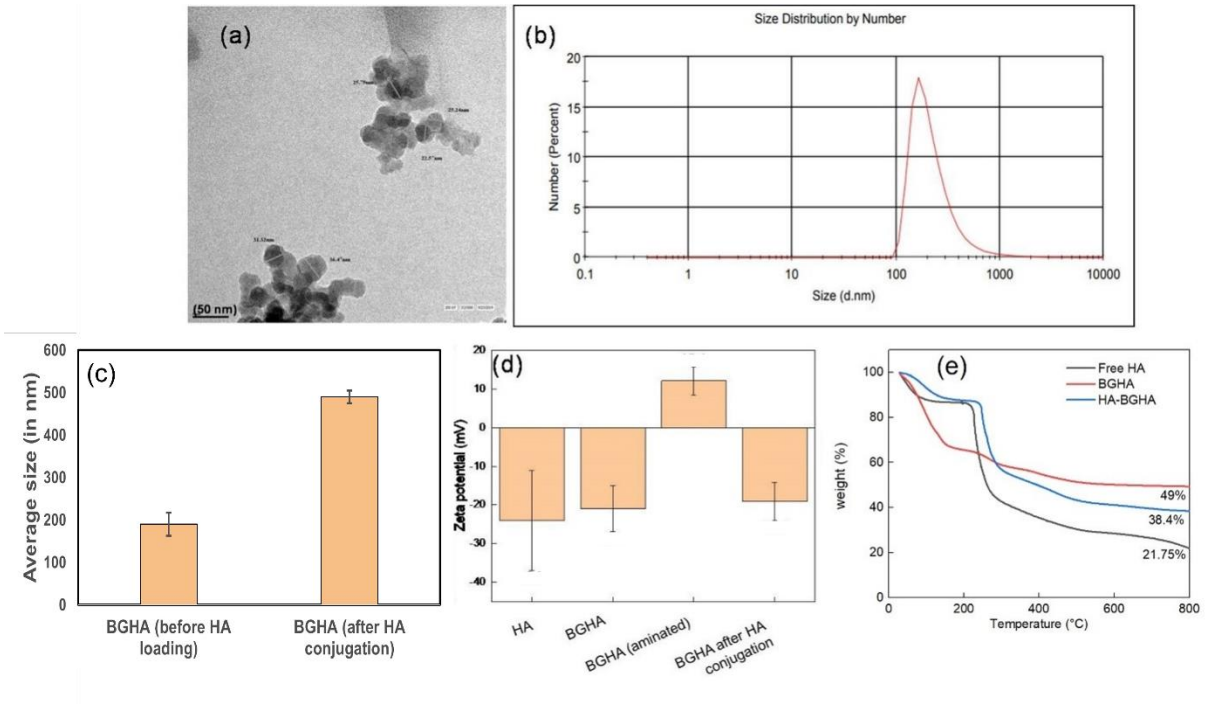

Figure 4.7 : (a)TEM (b, c) DLS; (d) zeta potential and (e) TGA of BGHA nano-composites conjugated externally with HA.

TGA of HA-BGHA demonstrated lesser shielding of HA to thermal stress when compared to BGHA, apparently due to its presence on the surface of the particle (Figure 4.7e). Since HA is hydrophilic in nature, the conjugation of HA is typically carried out in aqueous media[127]. As such purification steps can be minimized.

4.3.5 Bioactivity of native BGHA nanocomposites

The bioactivity of BGHA nanocomposites was evaluated by immersing them in simulated body fluid (SBF) for predetermined periods to induce the deposition of hydroxycarbonate apatite (HCA) on their surface. The affinity of BG to bone tissue can be attributed to the similarity between HCA and hydroxyapatite found in bone and teeth. After immersion in SBF for 7 days, samples were collected on days 1, 5, and 7 for characterization using FTIR, XRD,

and SEM techniques (Figure 4.8a-c). SEM images showed a noticeable change in the morphology of the BGHA nanocomposites by day 7, with the formation of HCA crystals observed on the surface.

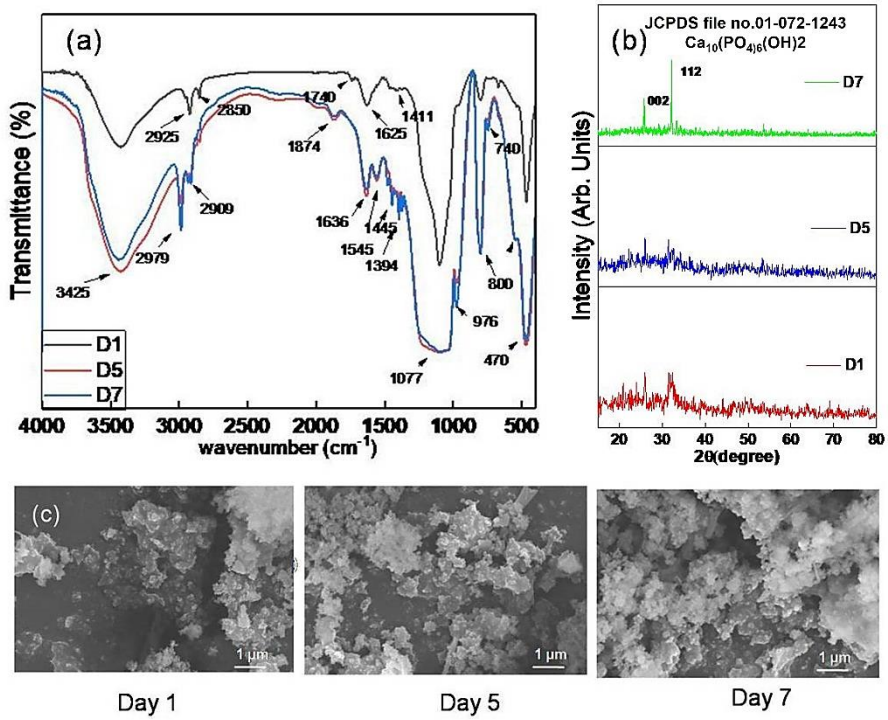

Figure 4.8 : Analysis of bioactivity of BGHA particles through (a) FTIR, (b) XRD and (c) SEM

The FTIR spectra revealed a peak at 1636 cm^{-1}, indicating the presence of an amide I group, likely due to the retention of HA. The peak at 976 $cm^{-1}$was intensified, indicating the symmetric stretching vibration of phosphate groups (PO_4^{3-}). The broadening of the peak at 1074 cm^{-1} and the sharpening of the peak at 800 cm^{-1} on days 5 and 7, respectively, were due to the asymmetric stretching of the phosphate group and indicated the formation of hydroxyapatite. The broad peak at 3400 cm^{-1}, which became magnified on days 5 and 7, provided evidence of an increase in the -OH group, which could be from absorbed water molecules [164] or deposited hydroxyapatite. The presence of peaks at 1545 and 1445 cm^{-1} indicated the asymmetric stretching of carbonate (CO_3^{2-}), while the presence of a peak at 630 cm^{-1} confirmed the formation of hydroxyapatite.

The XRD diffractogram of the samples recovered after incubation in SBF revealed characteristic diffraction maxima at 22.8° (111), 31.7°(211) and 46.6°(222) along with a broad bump in the *2Θ* range of 15° to 30°, representing the semi-amorphous character of the sample. These peaks were in agreement with JCPDS file no.01-072-1243 corresponding to $Ca_{10}(PO_{4)6}(OH)2$, suggesting the formation of hexagonal hydroxyapatite crystals on the surface of the nanocomposites.

The changes that occur in the BGHA nanocomposites when immersed in SBF are due to progressive deposition of a crystalline compound, hydroxyapatite on the surface of BG. These hydroxyapatite depositions resemble bone-like structures and provide mechanical and biologic cues for osteogenesis and osteo-regeneration while reducing adverse immune response to bioactive glass implants and nanoparticles. The emergence of the peaks could be observed as early as day 5, and fully developed peaks could be observed by day 7. Similar observations have been reported for bioactive glass nanoparticles synthesized through the bio-inspired method in various studies [41,55,108,161] . In SBF, the Si-O-Si groups present on the surface undergo hydrolysis to form $Si\text{-}O^-$, resulting in the release of sodium, phosphate, and calcium ions into the solution due to the disruption of the silica network. The calcium and phosphate ions can also be attracted to the $Si\text{-}O^-$ ions of the nanocomposites from the surrounding environment in SBF. These events promote the formation of calcium-phosphate complexes that deposit on the surface of the nanocomposites, resulting in the formation of hydroxyapatite crystals. The mesoporous nature of the nano-assemblies assists in this crystal growth.

Overall, BGHA demonstrated excellent bioactivity and thus has potential for application in bone tissue engineering.

4.3.6 *In-vitro* studies:

Cyto-compatibility of BGHA nanocomposites: The BGHA nanocomposites show significant potential as a versatile drug delivery system for various systemic applications. However, since our specific interest is in developing bioactive glasses for future bone and skin-related treatments, we conducted a cytocompatibility (MTT assay) study using human keratinocytes (HaCaT) and human osteosarcoma cell lines (U2OS). We exposed the cells to different concentrations of the nanocomposites and performed an MTT assay after 24 hours to determine the percentage of viable cells (Figure 4.9a). Our findings demonstrate that the nanocomposites are inherently biocompatible, with more than 70% cell viability observed across all tested concentrations [170,176]. Additionally, multiple studies have previously shown the biocompatible nature of bioactive glass nanoparticles with skin and bone cell lines [55,56,108] This biocompatible nature of the nanoparticles is due to the mesoporous and biodegradable nature of bioactive glass as a material which has led to multiple biologic application of the same in past studies [43,85,177].

Cellular uptake of FITC-BGHA nanocomposites:

Through FACS and fluorescence microscopy: We observed that the BGHA nanocomposites have demonstrated an ability to effectively penetrate cellular barriers, as evidenced by the successful uptake of FITC-BGHA by both skin (HaCaT) and bone (U2OS) cell lines. Using both quantitative (FACS, Figure 4.9b) and qualitative (fluorescence microscopy, Figure 4.9c) analysis, we observed effective penetration and uptake of the BGHA nanocomposites across cell membranes in both skin and bone cell lines. In FACS analysis, the majority of cells effectively took up the BGHA nanocomposites even at the lowest considered concentrations (10 µg/ml); however, the Mean Fluorescence Intensity (MFI) was found to be concentration-dependent.

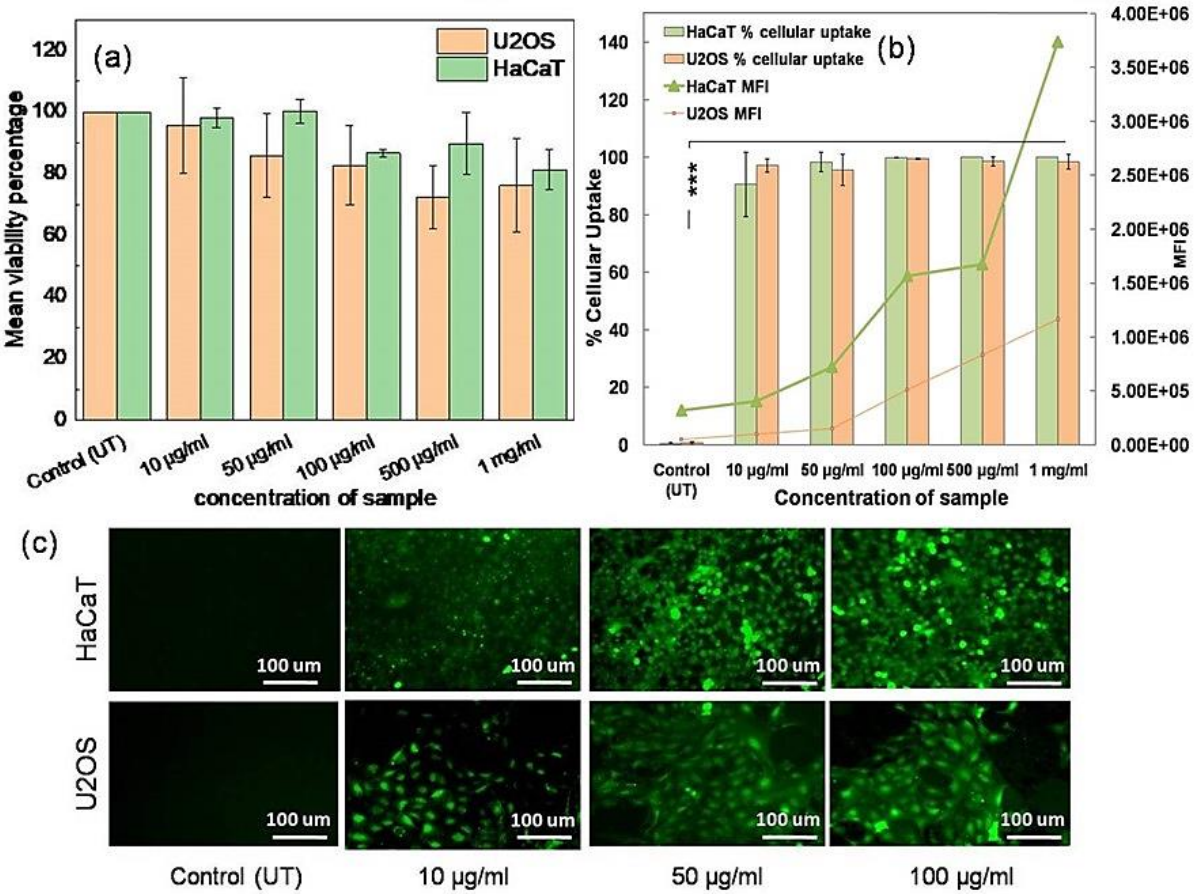

Figure 4.9: (a) Cytotoxicity (MTT) assay for BGHA nanocomposites on U2OS and HaCaT cell line; Cellular uptake of FITC-BGHA on both cell lines through (b) FACS and (c) fluorescence microscopy

Silica and BG nanoparticles have been reported to show high cellular uptake in multiple cell lines [176,178], which have been utilized for various topical and transdermal delivery strategies. Among these, HaCaT cells have been found to be particularly efficient for uptake of cargo in micrometers [179].

Through confocal microscopy: Confocal microscopy was used to observe the internalization of FITC-BGHA, revealing that the particles are possibly taken up through endocytosis and distributed within the cytosol and perinuclear space (Figure 4.10). Aggregated nanocomposites emit signals that increase with the concentration of FITC-BGHA, possibly due to altered particle surface charge and degree of aggregation [178]. It has been reported that HaCaT cells

can internalize silica nanocomposites in smaller aggregates and non-aggregated forms [148,178,180].

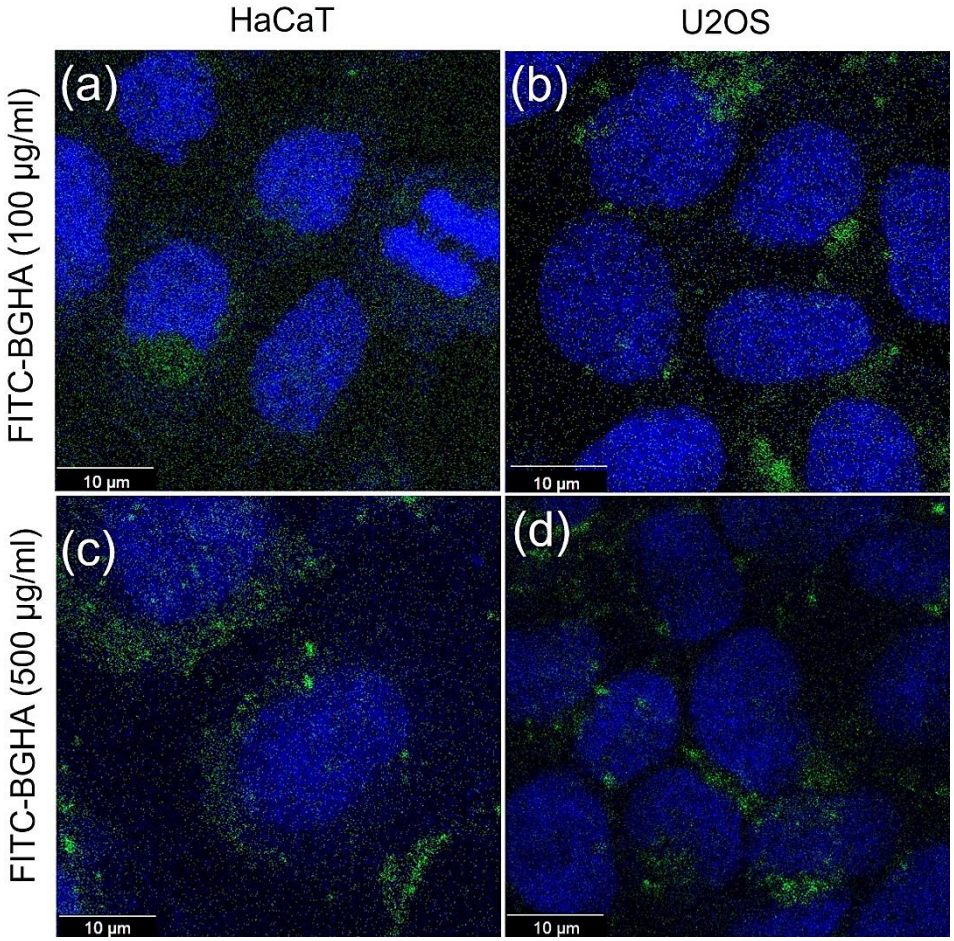

Figure 4.10 : Representative images from confocal microscopy of FITC-BGHA treatment on (a. c) HaCaT and (b, d) U2OS cell lines

Several factors including size (within 200 nm), sample concentration, cell type, and surface functionalization, have been suggested to influence the mechanism of cellular entry, with possible pathways such as macropinocytosis, clathrin-mediated endocytosis, or energy-dependent absorption on the plasma membrane followed by cellular entry [176,178–180]. Additionally, the spherical shape of the nanocomposites may contribute to the reduced time required for the cell membrane to wrap around the sphere when uptake occurs through phagocytosis [176].

Cellular uptake of FITC-HA-BGHA nanocomposites: FITC-HA-BGHA demonstrated efficient cellular uptake in both skin and bone cell lines, similar to the cellular uptake profile observed for FITC-BGHA (Figure 4.11). The fluorescence signal observed in the images through fluorescence microscopy is solely from HA conjugated to non-fluorescent BGHA nanocomposites. Quantitative analysis using FACS confirmed cellular uptake.

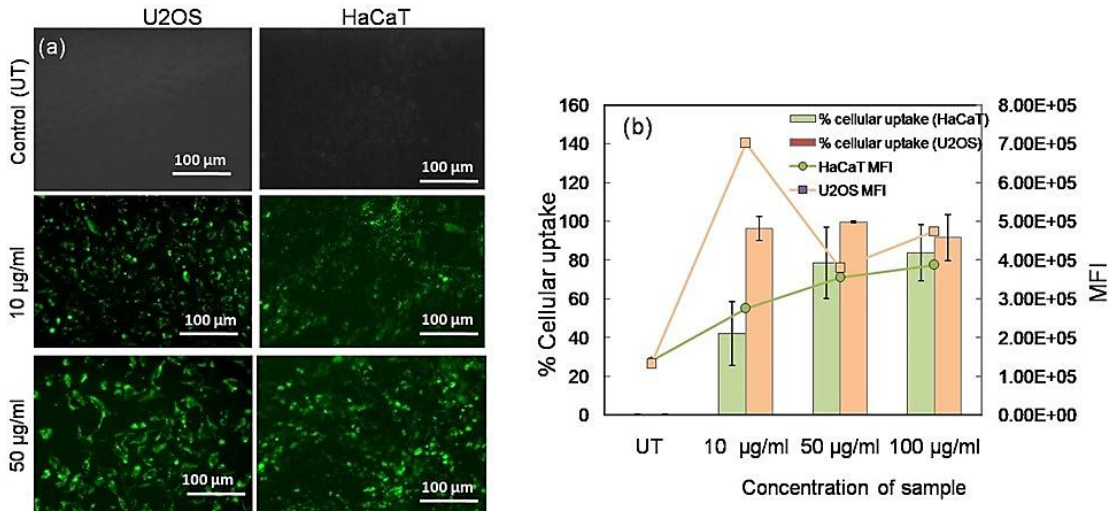

Figure 4.11 : Cellular uptake of BGHA tagged with FITC-HA externally through (a) fluorescence microscopy and (b) FACS

Confocal microscopy revealed the subcellular distribution of FITC-HA-BGHA, with representative images for selected concentrations provided in Figure 4.12. The majority of the green signal from FITC-HA-BGHA was observed in the cytoplasm, with few areas exhibiting signals overlapping with DAPI, indicating attachment to the nucleus or cellular surface [148].

Our FACS-based study showed that both FITC-BGHA and FITC-HA-BGHA exhibited a proportional increase in MFI with increasing concentration, indicating that cellular uptake or movement through cellular barriers could be concentration-dependent.

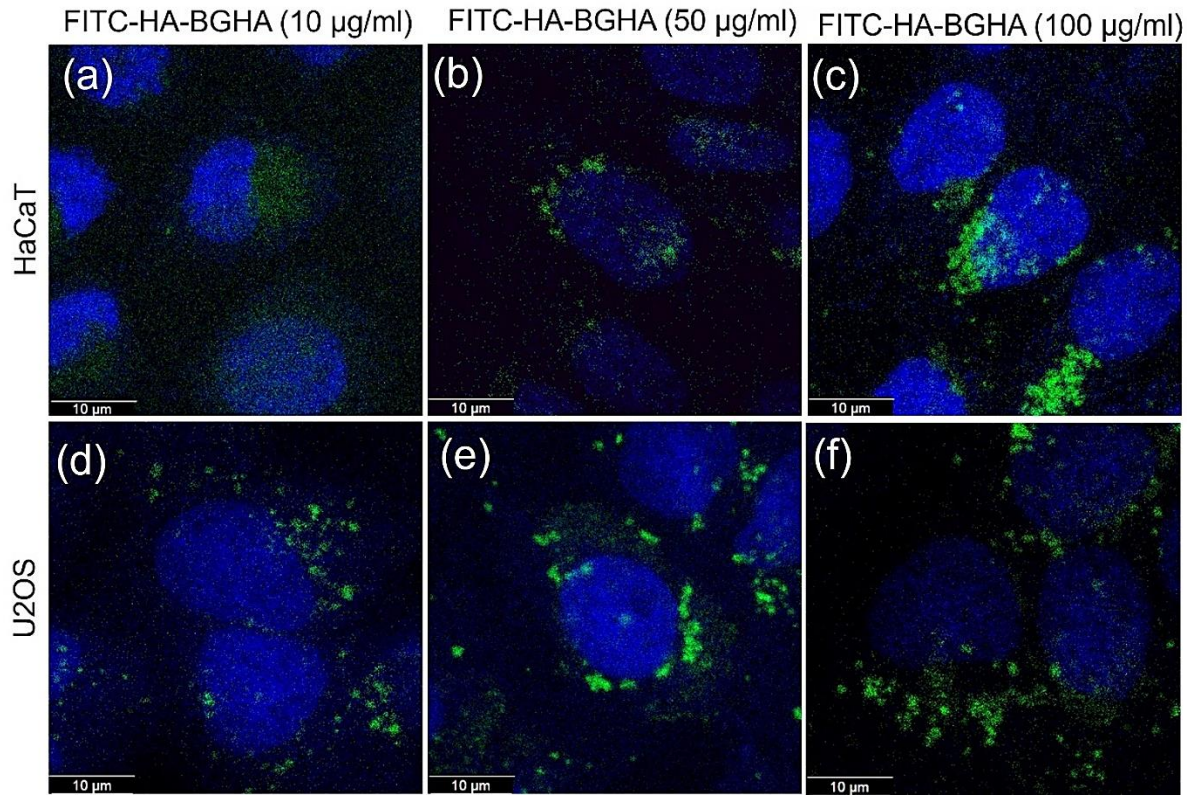

Figure 4.12: Representative images of confocal microscopy of cellular uptake of FITC-HA conjugated to native BGHA nanocomposites on (a, b and c) HaCaT and (d, e and f) U2OS cell lines.

4.4 Transwell-based studies for studying penetration of FITC-BGHA and FITC-HA-BGHA across keratinocyte layer

Transwell-based studies were conducted to investigate the ability of BGHA nanocomposites to penetrate a layer of keratinocytes grown on the membrane in the transwell chamber and reach the osteoblasts in the receptor chamber (Figure 4.13a). Keratinocytes were chosen because they represent 90 percent of the epidermis [178]. The FITC-tagged BGHA nanocomposites were taken up by the U2OS cell lines in the receptor chamber, as observed through fluorescence microscopy (Figure 13b, c) and quantified through FACS (Figure 4.13d). However, uptake in the transwell membrane was much higher than in the cells in the receptor chamber. The movement of particles through keratinocytes in the transwell chamber to the receiver chamber can be through intra-cellular or inter-cellular routes, but further studies are required for confirming the same.

In contrast, externally conjugated fluorescent HA (FITC-HA-BGHA) was only able to enter the HaCaT cells in the transwell chamber and not the U2OS cells in the receptor chamber, possibly due to added bulkiness resulting from external conjugation/grafting of FITC- HA.

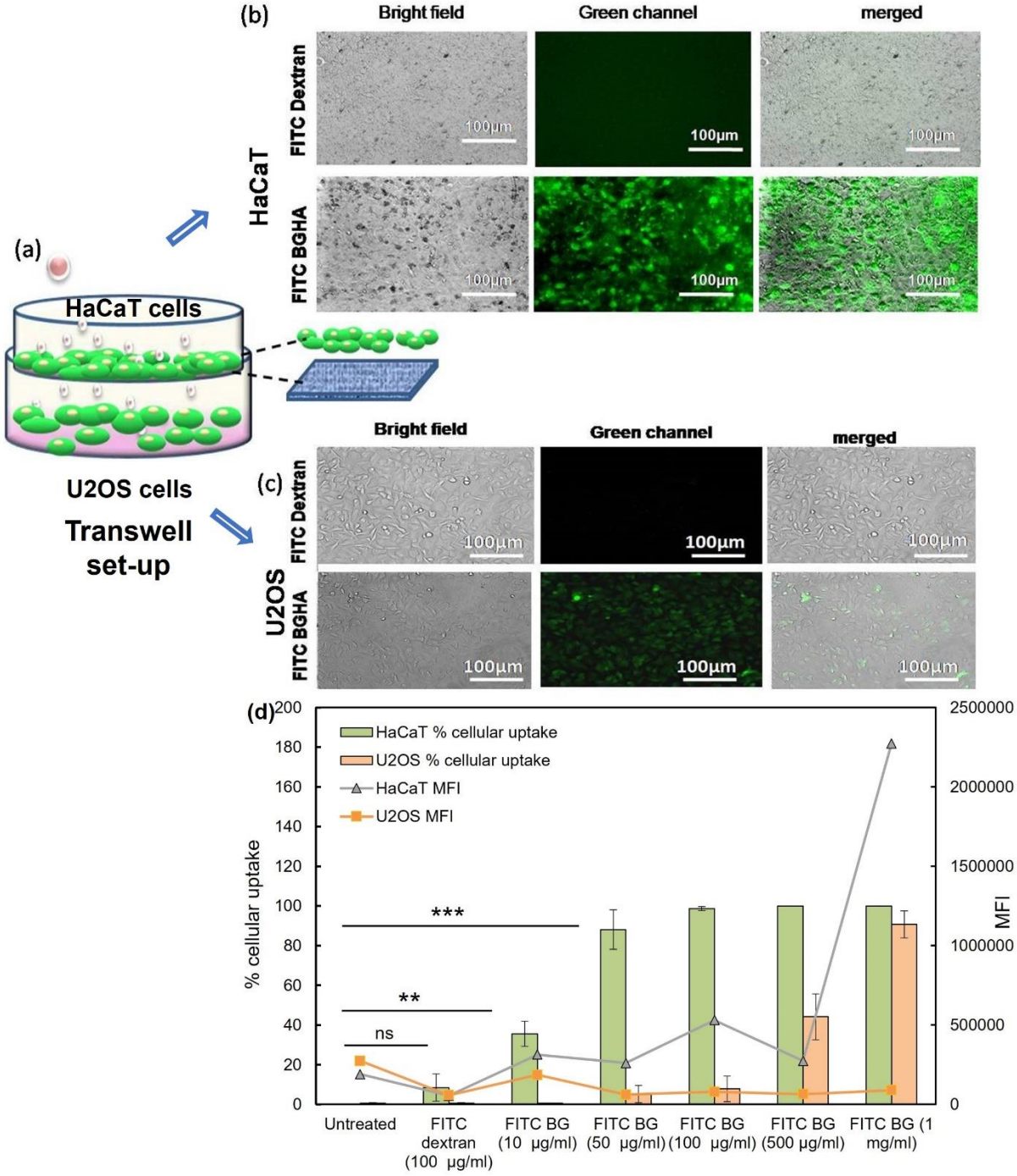

Figure 4.13 : (a) Graphical representation of transwell study, fluorescence microscopy for cellular uptake of FITC BGHA (100 µg/ml) and FITC-Dextran (100 µg/ml) on (b) HaCaT cells in transwell chamber and (c) on U2OS in receptor chamber; (d) FACS based quantitation of the same

4.5 *Ex-vivo* studies of FITC-BGHA and FITC-HA-BGHA in Strat-M® membrane-based Franz diffusion chamber:

To simulate the skin penetration properties of BGHA nanocomposites (with or without external HA conjugation) when applied topically, Franz Diffusion chamber-based assays were conducted (Figure 4.14a). It was observed that both FITC- tagged BGHA (FITC-BGHA) and externally conjugated FITC-HA-BGHA could remain minimally in the artificial skin membrane in the Franz diffusion chamber, while some amount of the same could penetrate the membrane and be deposited in the receptor PBS solution (Figure 4.14 b). Similar to what was observed in transwell-based studies, penetration of FITC-BGHA is higher than FITC-HA-BGHA suggesting that particle size is a factor for penetration in addition to surface charge and probable interactions with lipid components of the skin membrane. Furthermore, the retention and penetration levels were found to have been dependent on concentration and frequency of application. For instance, multiple applications of FITC-BGHA resulted in better penetration than a single large dose application (data not shown).

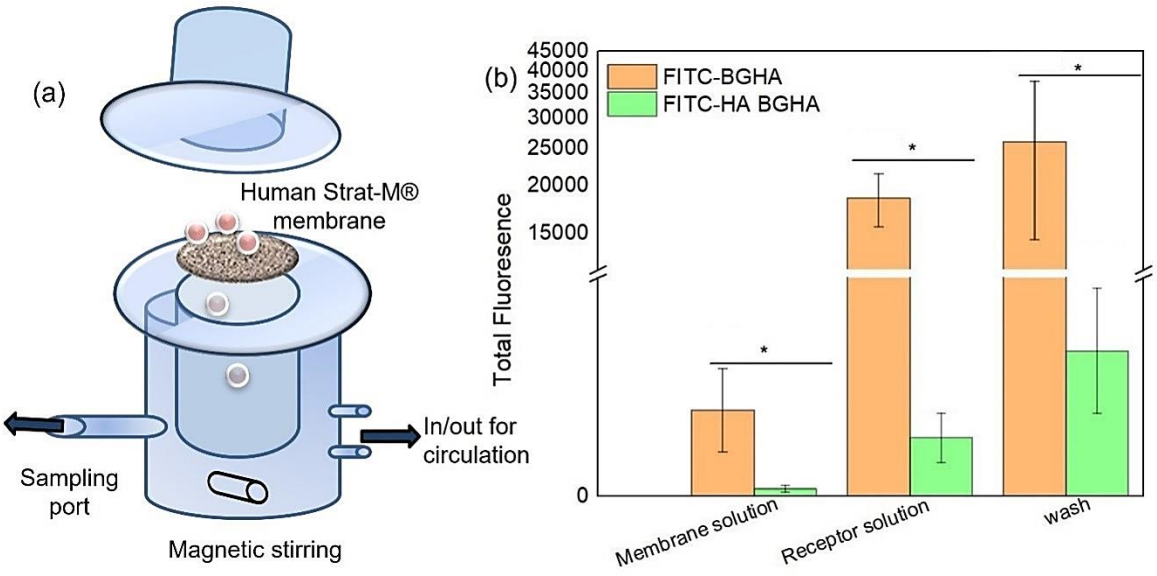

Figure 4.14 : (a) Graphical representation of the Franz-diffusion assay with mounted Strat-M® membrane; (b) measurement of fluorescence of the wash solution indicated nanocomposites that did not enter the skin, while that of the membrane solution indicated those that have been retained in the

skin membrane. The fluorescence reading of the receptor solution indicated nanocomposites that had thoroughly penetrated the skin membrane

The artificial membrane used, Strat-M®, mimics the lipid chemistry of human skin and is composed of layers of porous polyether sulfones (PES) and polyolefin fabric. With a thickness of 300 μm, the membrane mimics the epidermis, dermis, and subcutaneous skin tissue by modulating the porosity and thickness of its layers[181].

Other studies on penetration across the Strat-M membrane have included formulations for nicotine [181], caffeine [182], rhododendrol [182], which suggest the movement of hydrophilic compounds with enhancers such as polyols. Silica micro- and nanocomposites have also been suggested to overcome the stratum corneum in synthetic [183] or porcine skin membrane [184–186] and accumulate in the epidermis [187]. Amorphous FITC-labeled silica nanocomposites have been reported to penetrate the cyanoacrylate-stripped skin surface, with the study indicating the penetration of 42 nm silica nanocomposites through the stratum corneum and translocation to cellular layers comprising endothelial cells [178]. Similarly, silica nanocomposites, along with ionic liquids, have been shown to penetrate by "dragging" the nanocomposites with deep eutectic solvents through the stratum corneum [151]. The penetration of silica nanocomposites into the skin has been suggested to be mainly size-dependent [178] and has been utilized in numerous topical application strategies [187].

4.6 Implications and limitations of the study

The BGHA nanocomposites can have multiple applications in the medical and cosmeceutical fields. BGHA nanocomposites can be used as HA adjuvants in moisturizers, dermal fillers and other skin aesthetic targeting creams and lotions. In the case of biomedical applications, it can be applied as anti-inflammatory agent in osteoarthritis treatments, skin wound healing and regeneration, and as a component in soft and hard tissue implants, etc. Although our current

study focuses on topical application, it can also be used for systemic delivery of HA for various applications like bone repair and regeneration, etc.

This study provides preliminary evidence for the potential application of BGHA nanocomposites as both cargo and a delivery vehicle for HA, to and potentially across human skin. It is important to note that while synthetic membrane-based studies are useful for observing trends and correlations and optimizing formulations in the pharmaceutical, self-care, and cosmetic industries, they do not provide absolute permeability values for human skin[181]. Moreover, it has been suggested that biomimetic skin membranes provide more constant penetration profiles for mesoporous silica nanocomposites due to their homogeneous structure, unlike human or animal skin [151]. Nevertheless, previous studies on mesoporous amorphous silica nanocomposites [151,178,186] and our current results with bioactive glass nanocomposites suggest the potential for particle-based formulations to enhance drug retention and bioavailability in skin through intercalation with the stratum corneum.

The skin penetration of silica nanocomposites is generally thought to be influenced by various factors, including physico-chemical properties, surface area, dose, duration, frequency of exposure, skin surface conditions, and method of determining absorption [188]. While a few studies have reported conclusive evidence about human skin penetration [151], the majority of the literature remains ambiguous [152]. The stratum corneum is typically considered the primary barrier for absorption of nanocomposites into skin tissue, and suggested pathways for nanocomposites include passage through corneocytes or intercellular lipid matrices [152].

At this stage there are still a few unanswered questions about the strategy that we introduce in this study. Some of these are the structural configuration of HA when in composite form, loading and release kinetics of HA from the nanocomposites, the intactness of the functional properties of HA when in nanocomposite form, etc. Further, more optimization of reaction

conditions and pre-cursor concentrations needs to be carried out for increasing yield of the product along with elaborate *ex-vivo* and *in-vivo* studies.

4.7 Conclusion

The bio-inspired synthesis route for generating BGHA nanocomposites in a one-pot process, without the need for solvents, catalysts, or reagents, represents a significant step forward. The successful delivery of these nanocomposites, either with or without externally grafted HA, across biologic barriers is highly encouraging. In this study, we have attempted to understand the interaction of these nanocomposites with the skin at multiple levels, including uptake studies in keratinocytes, uptake and penetration of keratinocyte sheets in transwell-based studies, and retention and penetration in synthetic membranes mimicking human skin. All these studies have yielded positive results, which further encourage detailed mechanistic elucidation and *in-vivo* experimentation in future research.

CHAPTER 5

Conclusion and future prospects:

The development of third generation bioactive glass is a challenging yet intriguing endeavor. However, this innovation is crucial as it adds a new dimension to bioactive glass as a material, capable of altering complex tissue repair and regeneration pathways. With the potential to develop bioactive, biodegradable, mesoporous, and hybrid materials with clinically relevant molecules; in the nano-range, bio-inspired bioactive glass may play a significant role in drug delivery, in-situ tissue repair, and minimally invasive surgery. This could greatly benefit treatment for a range of diseases, injuries and bone related geriatric disorders. In fact, as predicted by Prof. Hench, the use of bioactive glasses due to their relevance as gene activating biomaterials may just be the "starting point" for bio-stimuli inducing biomaterials which are both disease and patient-specific.

The work in this thesis aims to contribute towards the common goal of developing diverse types of bioactive glass applicable in multiple fields, such as drug delivery, bone-tissue engineering, anti-cancer treatment, topical applications, and the cosmeceutical industry. Through a bio-inspired approach, we have attempted to synthesize composites of bioactive glass with unconventional templates, most of which were also the desired cargo. We have explored the various properties of these synthesized materials through multiple studies, many of which were attractive in terms of applications in the biomedical and cosmetic industries.

The key findings of the thesis are summarized below:

- The bio-inspired route is a viable method for synthesizing bioactive glass nanocomposites without the use of organic solvents, nitrates, ammonia, or high temperature calcination.

- Different templates, such as gelatin-CCNP, DOX, and HMW HA, can be used as structure directing agents for synthesis of bioactive glass nanocomposites through the bio-inspired method
- The mild reaction conditions and absence of the calcination step allow for the preservation of the structure and function of templates like DOX and HA.
- The retained template in the formed BG nanocomposite can be utilized as cargo for delivery-purposes.
- The formed nanocomposites have sizes in the nano-range, are mesoporous and amorphous in nature. Moreover, these nanocomposites demonstrate varying degrees bioactivity when immersed in simulated body fluid.
- The majority of the bioactive glass nanocomposites are biocompatible at concentrations ranging from 10 μg/ml to1 mg/ml and exhibit effective cellular uptake in skin and bone cells.
- The formed bioactive glass nanocomposites can serve as drug delivery agents for anti-cancer therapy, anti-inflammatory treatments for osteoarthritis, and viscoelastic agents.
- Lastly, if explored further, the formed bioactive glass nanocomposites due to their size and surface charge, can prove to be effective topical and transdermal delivery agents.

Hollow Bioactive glass nanoparticles:

- Mesoporous with pore size between 20-30 nm
- Sizes in range of 100 nm
- Demonstrates good bioactivity in SBF
- Biocompatible to bone cells (1 ug/ml to 1 mg/ml)

DOX-BG bioactive glass ceramic nanocomposites

- DOX acts as template as well as cargo

- Increased concentration of DOX in reaction mixture increases loading in formed DOX-BG nanocomposites
- Show sizes in nano-range and is mesoporous in nature
- Show sustained drug delivery
- Demonstrates bioactivity when immersed in SBF
- Shows better efficiency when compared to free DOX of equivalent dose in killing of osteosarcoma cells

BGHA and HA-BGHA nanocomposites

- Synthesized using HMW-HA as template which also acts as condensed cargo in the formed BGHA nanocomposites. Also suitable for externally conjugating HA on its surface1
- Size 100-200 nm and surface charge -21 to -25 mV
- Mesoporous and amorphous in nature
- Demonstrated viscoelastic properties
- Biocompatible to skin and bone cell lines (10ug/ml to 1 mg/ml)
- Attractive cellular uptake properties in bone and skin cell lines
- Probability of transcellular movement across keratinocytes as demonstrated by the transwell assay
- Probability of transdermal movement across artificial skin membrane as demonstrated by Franz diffusion chamber assay.

The studies conducted in this thesis focus on the use of unconventional but biologically relevant templates. This opens up possibilities for exploring other biologically relevant cargos such as drugs or biologicals, to be used as templates for bioactive glass synthesis

through bio-inspired methods. Current studies use synthetic surfactants to generate mesoporous bioactive glass nanoparticles. However, these surfactants are generally not considered safe for biological applications which limits the applications of bioactive glass synthesized using them. Additionally, the use of synthetic surfactants requires their removal through harsh chemical treatments or high temperature heating, both of which hinder the one-pot synthesis of bioactive glass with proteins, hormones, drugs, antibodies etc. Therefore, an additional step is always required for post-synthesis loading or conjugation of these components to the bioactive glass nanoparticles. Through the bio-inspired route, various biologically relevant components such as proteins, hormones, antibodies, peptides, drugs and enzymes can be used for forming composites with bioactive glass. This should not only allow for development of various new nanocomposites of bioactive glass but should also help in their targeted delivery, controlled release, and the creation of stable formulations. We are currently exploring many such amino acids, vitamins, and drugs as templates for developing bioactive glass composites while evaluating their packaging in its silica network, stability, release and most importantly, their efficacy.

However, these studies are still in their early stages and further research is needed to establish this synthesis route for such nanocomposites. Unlike the sol-gel methods, there have been very few studies reporting bio-inspired methods for bioactive glass synthesis and hence more research is required for better understanding of the mechanism and viability of this method. Additional studies are required to identify the correct templates, determine their optimum concentration for synthesis, assess the feasibility to form composites with bioactive glass, and evaluate their stability and loading efficiency. There is still ample opportunity to optimize the reaction conditions, develop the bioactivity property, the biodegradation profile, and maintain the structure

and functional properties of the biomolecules when packaged in bioactive glass nanocomposites. This is particularly important for proteins, enzymes, and certain drugs which have a higher likelihood of losing their functionality when in bound or packaged form in the nanocomposites.

Furthermore, most of our biological studies are carried out *in-vitro*. Therefore, further investigations are needed to study nanocomposites like DOX-BG and BGHA in more comprehensive ways, using *in-vitro*, *ex-vivo*, and animal models. More research is necessary to examine their long-term stability in biological fluids, bio-distribution and systemic release parameters, biodegradability, targeting specificity, biological safety and other factors. In summary, the studies in this thesis represent initial investigations in this field and requires thorough scientific insights to better understand the viability of this synthesis route and its potential widespread application. If successfully developed, the bio-inspired route for synthesizing nanocomposites of bioactive glass with biological components can be one of the simplest, most cost-effective, and environmentally friendly routes.

REFERENCES

(1) Hench, L. L. The Story of Bioglass®. *J Mater Sci Mater Med* **2006**, *17* (11), 967–978.

(2) Hench, L. L.; Clark, A. E.; Schaake, H. F. Effects of Microstructure on the Radiation Stability of Amorphous Semiconductors. *J Non Cryst Solids* **1972**, *8*, 837–843.

(3) Hench, L. L. Genetic Design of Bioactive Glass. *J Eur Ceram Soc* **2009**, *29* (7), 1257–1265.

(4) Jones, J. R.; Hench, L. L. Biomedical Materials for New Millennium: Perspective on the Future. *Materials Science and technology* **2001**, *17* (8), 891–900.

(5) Piotrowski, G.; Hench, L. L.; Allen, W. C.; Miller, G. J. Mechanical Studies of the Bone Bioglass Interfacial Bond. *J Biomed Mater Res* **1975**, *9* (4), 47–61.

(6) Hench, L. L.; Pantano Jr, C. G.; Buscemi, P. J.; Greenspan, D. C. Analysis of Bioglass Fixation of Hip Prostheses. *J Biomed Mater Res* **1977**, *11* (2), 267–282.

(7) Hench, L. L.; Clark, A. E. Biocompatibility of Orthopedic Implants. *by DF Williams, CRC Press, Boca Raton* **1982**, 129–170.

(8) Larry L Hench. Bioceramics. *Journal of the American Ceramic Society* **2005**, *18* (7).

(9) Ratner, B. D.; Williams, D. F. Biocompatibility of Clinical Implant Materials. *CRC, Boca Raton, FL* **1981**.

(10) Hench, L. L. Bioceramics: From Concept to Clinic. *Journal of the american ceramic society* **1991**, *74* (7), 1487–1510.

(11) Hench, L. L.; West, J. K. *Biological Applications of Bioactive Glasses*; Harwood Academic Publishers, 1996.

(12) Greenspan, D. C.; Hench, L. L. Chemical and Mechanical Behavior of Bioglass-coated Alumina. *J Biomed Mater Res* **1976**, *10* (4), 503–509.

(13) Gross, U.; Strunz, V. The Interface of Various Glasses and Glass Ceramics with a Bony Implantation Bed. *J Biomed Mater Res* **1985**, *19* (3), 251–271.

(14) Wilson, J.; Pigott, G. H.; Schoen, F. J.; Hench, L. L. Toxicology and Biocompatibility of Bioglasses. *J Biomed Mater Res* **1981**, *15* (6), 805–817.

(15) Douek, E. Otologic Applications of Bioglass® Implants. *Bioceramics* **1991**, *4*.

(16) Hench, L. L.; Hench, J. W.; Greenspan, D. C. Bioglass: A Short History and Bibliography. *Journal of the Australasian Ceramic Society* **2004**, *40* (1), 1–42.

(17) Kaur, G.; Pickrell, G.; Sriranganathan, N.; Kumar, V.; Homa, D. Review and the State of the Art: Sol–Gel and Melt Quenched Bioactive Glasses for Tissue Engineering. *J Biomed Mater Res B Appl Biomater* **2016**, *104* (6), 1248–1275.

(18) Fagerlund, S.; Hupa, L. Melt-Derived Bioactive Silicate Glasses. **2016**.

(19) Romeis, S.; Hoppe, A.; Eisermann, C.; Schneider, N.; Boccaccini, A. R.; Schmidt, J.; Peukert, W. Enhancing in Vitro Bioactivity of Melt-derived 45S5 Bioglass® by Comminution in a Stirred Media Mill. *Journal of the American Ceramic Society* **2014**, *97* (1), 150–156.

(20) Li, R.; Clark, A. E.; Hench, L. L. An Investigation of Bioactive Glass Powders by Sol-gel Processing. *Journal of Applied Biomaterials* **1991**, *2* (4), 231–239.

(21) Vale, A. C.; Pereira, P. R.; Barbosa, A. M.; Torrado, E.; Alves, N. M. Optimization of Silver-Containing Bioglass Nanoparticles Envisaging Biomedical Applications. *Materials Science and Engineering: C* **2019**, *94*, 161–168.

(22) Smith, S.; ElKashty, O.; Tamimi, F.; Tran, S. D.; Cerruti, M. Titanium-Containing Silicate-Based Sol–Gel Bioactive Glass: Development, Characterization, and Applications. *Langmuir* **2021**, *37* (49), 14243–14253.

(23) Bari, A.; Bloise, N.; Fiorilli, S.; Novajra, G.; Vallet-Regí, M.; Bruni, G.; Torres-Pardo, A.; González-Calbet, J. M.; Visai, L.; Vitale-Brovarone, C. Copper-Containing Mesoporous Bioactive Glass Nanoparticles as Multifunctional Agent for Bone Regeneration. *Acta Biomater* **2017**, *55*, 493–504.

(24) Gharbi, A.; Oudadesse, H.; El Feki, H.; Cheikhrouhou-Koubaa, W.; Chatzistavrou, X.; V. Rau, J.; Heinämäki, J.; Antoniac, I.; Ashammakhi, N.; Derbel, N. High Boron Content Enhances Bioactive Glass Biodegradation. *J Funct Biomater* **2023**, *14* (7), 364.

(25) Zheng, K.; Boccaccini, A. R. Sol-Gel Processing of Bioactive Glass Nanoparticles: A Review. *Adv Colloid Interface Sci* **2017**, *249*, 363–373.

(26) Hench, L. L.; West, J. K. The Sol-Gel Process. *Chem Rev* **1990**, *90* (1), 33–72.

(27) Vichery, C.; Nedelec, J.-M. Bioactive Glass Nanoparticles: From Synthesis to Materials Design for Biomedical Applications. *Materials* **2016**, *9* (4), 288.

(28) Ghimire, P. P.; Jaroniec, M. Renaissance of Stöber Method for Synthesis of Colloidal Particles: New Developments and Opportunities. *J Colloid Interface Sci* **2021**, *584*, 838–865.

(29) Stöber, W.; Fink, A.; Bohn, E. Controlled Growth of Monodisperse Silica Spheres in the Micron Size Range. *J Colloid Interface Sci* **1968**, *26* (1), 62–69.

(30) Taghvaei, A. H.; Danaeifar, F.; Gammer, C.; Eckert, J.; Khosravimelal, S.; Gholipourmalekabadi, M. Synthesis and Characterization of Novel Mesoporous Strontium-Modified Bioactive Glass Nanospheres for Bone Tissue Engineering Applications. *Microporous and Mesoporous Materials* **2020**, *294*, 109889.

(31) Li, X.; Qu, F.; Li, W.; Lin, H.; Jin, Y. Synthesis of Hierarchically Porous Bioactive Glasses Using Natural Plants as Template for Bone Tissue Regeneration. *J Solgel Sci Technol* **2012**, *63*, 416–424.

(32) Santhiya, D.; Burghard, Z.; Greiner, C.; Jeurgens, L. P. H.; Subkowski, T.; Bill, J. Bioinspired Deposition of TiO2 Thin Films Induced by Hydrophobins. *Langmuir* **2010**, *26* (9), 6494–6502.

(33) Bauermann, L. P.; del Campo, A.; Bill, J.; Aldinger, F. Heterogeneous Nucleation of ZnO Using Gelatin as the Organic Matrix. *Chemistry of materials* **2006**, *18* (8), 2016–2020.

(34) Bauermann, L. P.; Bill, J.; Aldinger, F. Bio-Friendly Synthesis of ZnO Nanoparticles in Aqueous Solution at near-Neutral PH and Low Temperature. *J Phys Chem B* **2006**, *110* (11), 5182–5185.

(35) Kröger, N.; Sandhage, K. H. From Diatom Biomolecules to Bioinspired Syntheses of Silica-and Titania-Based Materials. *MRS Bull* **2010**, *35* (2), 122–126.

(36) Lei, Q.; Guo, J.; Kong, F.; Cao, J.; Wang, L.; Zhu, W.; Brinker, C. J. Bioinspired Cell Silicification: From Extracellular to Intracellular. *J Am Chem Soc* **2021**, *143* (17), 6305–6322.

(37) Goel, H.; Santhiya, D. Effect of PH on Bio-Inspired Synthesis of L-Lysine Templated Bioactive Glass Hybrid Xerogels for Tailored Textural and Rheological Properties. *Mater Chem Phys* **2022**, *281*, 125828.

(38) Gupta, N.; Santhiya, D. Role of Cellulose Functionality in Bio-Inspired Synthesis of Nano Bioactive Glass. *Materials Science and Engineering: C* **2017**, *75*, 1206–1213.

(39) Santhiya, D.; kumari Alajangi, H.; Anjum, F.; Murugavel, S.; Ganguli, M. Bio-Inspired Synthesis of Microporous Bioactive Glass-Ceramic Using CT-DNA as a Template. *J Mater Chem B* **2013**, *1* (45), 6329–6338.

(40) Gupta, N.; Santhiya, D. In Situ Mineralization of Bioactive Glass in Gelatin Matrix. *Mater Lett* **2017**, *188*, 127–129.

(41) Goel, H.; Santhiya, D. Role of Trigonella Foenum-Graecum Leaf Extract in Tailoring the Synthesis and Properties of Bioactive Glass Nanoparticles. *Sustainable Materials and Technologies* **2022**, *33*, e00485.

(42) Pappas, G. S.; Bilalis, P.; Kordas, G. C. Synthesis and Characterization of SiO2–CaO–P2O5 Hollow Nanospheres for Biomedical Applications. *Mater Lett* **2012**, *67* (1), 273–276.

(43) Wang, Y.; Pan, H.; Chen, X. The Preparation of Hollow Mesoporous Bioglass Nanoparticles with Excellent Drug Delivery Capacity for Bone Tissue Regeneration. *Front Chem* **2019**, *7*, 283.

(44) Hu, Q.; Li, Y.; Zhao, N.; Ning, C.; Chen, X. Facile Synthesis of Hollow Mesoporous Bioactive Glass Sub-Micron Spheres with a Tunable Cavity Size. *Mater Lett* **2014**, *134*, 130–133.

(45) Luz, G. M.; Mano, J. F. Nanoengineering of Bioactive Glasses: Hollow and Dense Nanospheres. *Journal of nanoparticle research* **2013**, *15* (2), 1–11.

(46) Li, Y.; Bastakoti, B. P.; Yamauchi, Y. Smart Soft-Templating Synthesis of Hollow Mesoporous Bioactive Glass Spheres. *Chem.–Eur. J* **2015**, *21*, 8038–8042.

(47) Liu, T.; Li, Z.; Ding, X.; Zhang, L.; Zi, Y. Facile Synthesis of Hollow Bioactive Glass Nanospheres with Tunable Size. *Mater Lett* **2017**, *190*, 99–102.

(48) Li, B.; Luo, W.; Wang, Y.; Wu, H.; Zhang, C. Bioactive SiO2-CaO-P2O5 Hollow Nanospheres for Drug Delivery. *J Non Cryst Solids* **2016**, *447*, 98–103.

(49) Mutlu, N.; Beltrán, A. M.; Nawaz, Q.; Michálek, M.; Boccaccini, A. R.; Zheng, K. Combination of Selective Etching and Impregnation toward Hollow Mesoporous Bioactive Glass Nanoparticles. *Nanomaterials* **2021**, *11* (7), 1846.

(50) Ding, X.; Zheng, J.; Ju, F.; Wang, L.; Kong, J.; Feng, J.; Liu, T. Facile Fabrication of Hollow Mesoporous Bioactive Glass Spheres: From Structural Behaviour to in Vitro Biology Evaluation. *Ceram Int* **2021**, *47* (24), 34836–34844.

(51) Duan, H.; Diao, J.; Zhao, N.; Ma, Y. Synthesis of Hollow Mesoporous Bioactive Glass Microspheres with Tunable Shell Thickness by Hydrothermal-Assisted Self-Transformation Method. *Mater Lett* **2016**, *167*, 201–204.

(52) Izquierdo-Barba, I.; Vallet-Regí, M. Mesoporous Bioactive Glasses: Relevance of Their Porous Structure Compared to That of Classical Bioglasses. *Biomedical glasses* **2015**, *1* (1).

(53) Kong, C. H.; Steffi, C.; Shi, Z.; Wang, W. Development of Mesoporous Bioactive Glass Nanoparticles and Its Use in Bone Tissue Engineering. *J Biomed Mater Res B Appl Biomater* **2018**, *106* (8), 2878–2887.

(54) Wang, Y.; Chen, X. Facile Synthesis of Hollow Mesoporous Bioactive Glasses with Tunable Shell Thickness and Good Monodispersity by Micro-Emulsion Method. *Mater Lett* **2017**, *189*, 325–328.

(55) Goel, H.; Gupta, N.; Santhiya, D.; Dey, N.; Bohidar, H. B.; Bhattacharya, A. Bioactivity Reinforced Surface Patch Bound Collagen-Pectin Hydrogel. *Int J Biol Macromol* **2021**, *174*, 240–253.

(56) Gupta, N.; Singh, A.; Dey, N.; Chattopadhyay, S.; Joseph, J. P.; Gupta, D.; Ganguli, M.; Pal, A. Pathway-Driven Peptide–Bioglass Nanocomposites as the Dynamic and Self-Healable Matrix. *Chemistry of Materials* **2021**, *33* (2), 589–599.

(57) Virtudazo, R. V. R.; Watanabe, H.; Shirai, T.; Fuji, M. Simple Preparation and Initial Characterization of Semi-Amorphous Hollow Calcium Silicate Hydrate Nanoparticles by Ammonia-Hydrothermal-Template Techniques. *Journal of nanoparticle research* **2013**, *15* (5), 1–9.

(58) Nakashima, Y.; Takai, C.; Razavi-Khosroshahi, H.; Suthabanditpong, W.; Fuji, M. Synthesis of Ultra-Small Hollow Silica Nanoparticles Using the Prepared Amorphous Calcium Carbonate in One-Pot Process. *Advanced Powder Technology* **2018**, *29* (4), 904–908.

(59) Douglas, T. E. L.; Piwowarczyk, W.; Pamula, E.; Liskova, J.; Schaubroeck, D.; Leeuwenburgh, S. C. G.; Brackman, G.; Balcaen, L.; Detsch, R.; Declercq, H.; Cholewa-Kowalska, K.; Dokupil, A.; Cuijpers, V. M. J. I.; Vanhaecke, F.; Cornelissen, R.; Coenye, T.; Boccaccini, A. R.; Dubruel, P. Injectable Self-Gelling Composites for Bone Tissue Engineering Based on Gellan Gum Hydrogel Enriched with Different Bioglasses. *Biomedical Materials (Bristol)* **2014**, *9* (4). https://doi.org/10.1088/1748-6041/9/4/045014.

(60) Chen, J.-F.; Ding, H.-M.; Wang, J.-X.; Shao, L. Preparation and Characterization of Porous Hollow Silica Nanoparticles for Drug Delivery Application. *Biomaterials* **2004**, *25* (4), 723–727.

(61) Gautam, M.; Santhiya, D.; Dey, N. Zein Coated Calcium Carbonate Nanoparticles for the Targeted Controlled Release of Model Antibiotic and Nutrient across the Intestine. *Mater Today Commun* **2020**, *25*, 101394.

(62) Gupta, N.; Santhiya, D.; Aditya, A. Tailored Smart Bioactive Glass Nanoassembly for Dual Antibiotic in Vitro Sustained Release against Osteomyelitis. *J Mater Chem B* **2016**, *4* (47), 7605–7619.

(63) Kokubo, T.; Takadama, H. How Useful Is SBF in Predicting in Vivo Bone Bioactivity? *Biomaterials* **2006**, *27* (15), 2907–2915.

(64) Wu, K. C.-W.; Yamauchi, Y. Controlling Physical Features of Mesoporous Silica Nanoparticles (MSNs) for Emerging Applications. *J Mater Chem* **2012**, *22* (4), 1251–1256.

(65) Dias, L. L. S.; Mansur, H. S.; Donnici, C. L.; Pereira, M. M. Synthesis and Characterization of Chitosan-Polyvinyl Alcohol-Bioactive Glass Hybrid Membranes. *Biomatter* **2011**, *1* (1), 114–119.

(66) Koike, N.; Chaikittisilp, W.; Shimojima, A.; Okubo, T. Surfactant-Free Synthesis of Hollow Mesoporous Organosilica Nanoparticles with Controllable Particle Sizes and Diversified Organic Moieties. *RSC Adv* **2016**, *6* (93), 90435–90445.

(67) Virtudazo, R. V. R.; Tanaka, H.; Watanabe, H.; Fuji, M.; Shirai, T. Facile Preparation in Synthesizing Nano-Size Hollow Silicate Particles by Encapsulating Colloidal-Hydroxyapatite Nanoparticles. *J Mater Chem* **2011**, *21* (45), 18205–18207.

(68) Sing, K. S. W.; Williams, R. T. Physisorption Hysteresis Loops and the Characterization of Nanoporous Materials. *Adsorption Science & Technology* **2004**, *22* (10), 773–782.

(69) Vikulina, A.; Webster, J.; Voronin, D.; Ivanov, E.; Fakhrullin, R.; Vinokurov, V.; Volodkin, D. Mesoporous Additive-Free Vaterite CaCO3 Crystals of Untypical Sizes: From Submicron to Giant. *Mater Des* **2021**, *197*, 109220.

(70) Kokubo, T. Bioactive Glass Ceramics: Properties and Applications. *Biomaterials* **1991**, *12* (2), 155–163.

(71) Fuji, M.; Han, Y. S.; Takai, C. Synthesis and Applications of Hollow Particles. *KONA Powder and Particle Journal* **2013**, *30*, 47–68.

(72) Fuji, M.; Takai, C.; Tarutani, Y.; Takei, T.; Takahashi, M. Surface Properties of Nanosize Hollow Silica Particles on the Molecular Level. *Advanced Powder Technology* **2007**, *18* (1), 81–91.

(73) Fuji, M. Hollow Particles as Controlled Small Space to Functionalize Materials. *Journal of the ceramic society of Japan* **2015**, *123* (1441), 835–844.

(74) Virtudazo, V. R. R.; Fuji, M.; Takai, C.; Shirai, T. Development of Eco-Friendly Techniques for Preparation of Porous Nano-/Micro-Size Hollow Silicate Particles. **2012**.

(75) Jones, J. R. Reprint of: Review of Bioactive Glass: From Hench to Hybrids. *Acta Biomater* **2015**, *23*, S53–S82.

(76) Kaur, G.; Pandey, O. P.; Singh, K.; Homa, D.; Scott, B.; Pickrell, G. A Review of Bioactive Glasses: Their Structure, Properties, Fabrication and Apatite Formation. *Journal of Biomedical Materials Research Part A: An Official Journal of The Society for Biomaterials, The Japanese Society for Biomaterials, and The Australian Society for Biomaterials and the Korean Society for Biomaterials* **2014**, *102* (1), 254–274.

(77) Matos, R. J. R.; Soares, P. I. P.; Silva, J. C.; Borges, J. P. Magnetic Bioactive Glass-Based 3D Systems for Bone Cancer Therapy and Regeneration. *Materials Proceedings* **2022**, *8* (1), 18.

(78) Danewalia, S. S.; Singh, K. Bioactive Glasses and Glass–Ceramics for Hyperthermia Treatment of Cancer: State-of-Art, Challenges, and Future Perspectives. *Mater Today Bio* **2021**, *10*, 100100.

(79) Liu, Y.; Lin, R.; Ma, L.; Zhuang, H.; Feng, C.; Chang, J.; Wu, C. Mesoporous Bioactive Glass for Synergistic Therapy of Tumor and Regeneration of Bone Tissue. *Appl Mater Today* **2020**, *19*, 100578.

(80) Sharifi, E.; Bigham, A.; Yousefiasl, S.; Trovato, M.; Ghomi, M.; Esmaeili, Y.; Samadi, P.; Zarrabi, A.; Ashrafizadeh, M.; Sharifi, S. Mesoporous Bioactive Glasses in Cancer Diagnosis and Therapy: Stimuli-responsive, Toxicity, Immunogenicity, and Clinical Translation. *Advanced Science* **2022**, *9* (2), 2102678.

(81) Jayalekshmi, A. C.; Sharma, C. P. Gold Nanoparticle Incorporated Polymer/Bioactive Glass Composite for Controlled Drug Delivery Application. *Colloids Surf B Biointerfaces* **2015**, *126*, 280–287.

(82) Wu, C.; Fan, W.; Chang, J. Functional Mesoporous Bioactive Glass Nanospheres: Synthesis, High Loading Efficiency, Controllable Delivery of Doxorubicin and Inhibitory Effect on Bone Cancer Cells. *J Mater Chem B* **2013**, *1* (21), 2710–2718.

(83) Kevadiya, B. D.; Zhang, L.; Davé, R. N. Sustained Release of Poorly Water-Soluble Drug from Hydrophilic Polymeric Film Sandwiched between Hydrophobic Layers. *AAPS PharmSciTech* **2018**, *19* (6), 2572–2584.

(84) Wang, X.; Zhang, Y.; Ma, Y.; Chen, D.; Yang, H.; Li, M. Selenium–Containing Mesoporous Bioactive Glass Particles: Physicochemical and Drug Delivery Properties. *Ceram Int* **2016**, *42* (2), 3609–3617.

(85) Singh, R. K.; Kurian, A. G.; Patel, K. D.; Mandakhbayar, N.; Lee, N.-H.; Knowles, J. C.; Lee, J.-H.; Kim, H.-W. Label-Free Fluorescent Mesoporous Bioglass for Drug Delivery, Optical Triple-Mode Imaging, and Photothermal/Photodynamic Synergistic Cancer Therapy. *ACS Appl Bio Mater* **2020**, *3* (4), 2218–2229.

(86) Firuzeh, M.; Labbaf, S.; Sabouri, Z. A Facile Synthesis of Mono-Dispersed, Spherical and Mesoporous Bioactive Glass Nanoparticles for Biomedical Applications. *J Non Cryst Solids* **2021**, *554*, 120598.

(87) Li, X.; Liang, Q.; Zhang, W.; Li, Y.; Ye, J.; Zhao, F.; Chen, X.; Wang, S. Bio-Inspired Bioactive Glasses for Efficient MicroRNA and Drug Delivery. *J Mater Chem B* **2017**, *5* (31), 6376–6384.

(88) Zhang, Y.; Hu, M.; Wang, X.; Zhou, Z.; Liu, Y. Design and Evaluation of Europium Containing Mesoporous Bioactive Glass Nanospheres: Doxorubicin Release Kinetics and Inhibitory Effect on Osteosarcoma MG 63 Cells. *Nanomaterials* **2018**, *8* (11), 961.

(89) Wang, X.; Wang, G.; Zhang, Y. Research on the Biological Activity and Doxorubicin Release Behavior in Vitro of Mesoporous Bioactive SiO2-CaO-P2O5 Glass Nanospheres. *Appl Surf Sci* **2017**, *419*, 531–539.

(90) ur Rahman, M. S.; Tahir, M. A.; Noreen, S.; Yasir, M.; Khan, M. B.; Mahmood, T.; Bahadur, A.; Shoaib, M. Osteogenic Silver Oxide Doped Mesoporous Bioactive Glass for Controlled Release of Doxorubicin against Bone Cancer Cell Line (MG-63): In Vitro and in Vivo Cytotoxicity Evaluation. *Ceram Int* **2020**, *46* (8), 10765–10770.

(91) Lin, S. Tailoring the Nanostructure of Sol-Gel Derived Bioactive Glasses and Investigating Their Interactions with Proteins. Imperial College London 2010.

(92) Lin, S.; Ionescu, C.; Pike, K. J.; Smith, M. E.; Jones, J. R. Nanostructure Evolution and Calcium Distribution in Sol–Gel Derived Bioactive Glass. *J Mater Chem* **2009**, *19* (9), 1276–1282.

(93) Wu, C.; Chang, J. Mesoporous Bioactive Glasses: Structure Characteristics, Drug/Growth Factor Delivery and Bone Regeneration Application. *Interface Focus* **2012**, *2* (3), 292–306.

(94) Kumar, A.; Aditya, A.; Murugavel, S. Effect of Surfactant Concentration on Textural Characteristics and Biomineralization Behavior of Mesoporous Bioactive Glasses. *Materials Science and Engineering: C* **2019**, *96*, 20–29.

(95) Shih, C.-C.; Chien, C.-S.; Kung, J.-C.; Chen, J.-C.; Chang, S.-S.; Lu, P.-S.; Shih, C.-J. Effect of Surfactant Concentration on Characteristics of Mesoporous Bioactive Glass Prepared by Evaporation Induced Self-Assembly Process. *Appl Surf Sci* **2013**, *264*, 105–110.

(96) Jiang, S.; Hua, L.; Guo, Z.; Sun, L. One-Pot Green Synthesis of Doxorubicin Loaded-Silica Nanoparticles for in Vivo Cancer Therapy. *Materials Science and Engineering: C* **2018**, *90*, 257–263.

(97) Baghbanbashi, M.; Pazuki, G.; Khoee, S. One Pot Doxorubicin Partitioning and Encapsulation on Silica Nanoparticle, Applying Aqueous Two Phase System for Preparation of PH-Responsive Nanocarriers. **2021**.

(98) Li, S.; Ma, Y.; Yue, X.; Cao, Z.; Dai, Z. One-Pot Construction of Doxorubicin Conjugated Magnetic Silica Nanoparticles. *New Journal of Chemistry* **2009**, *33* (12), 2414–2418.

(99) He, X.; Hai, L.; Su, J.; Wang, K.; Wu, X. One-Pot Synthesis of Sustained-Released Doxorubicin Silica Nanoparticles for Aptamer Targeted Delivery to Tumor Cells. *Nanoscale* **2011**, *3* (7), 2936–2942.

(100) Sun, J.; Piao, J.; Wang, L.; Javed, M.; Hong, C.; Pan, C. One-pot Synthesis of Redox-responsive Polymers-coated Mesoporous Silica Nanoparticles and Their Controlled Drug Release. *Macromol Rapid Commun* **2013**, *34* (17), 1387–1394.

(101) Wang, J.; Xu, D.; Deng, T.; Li, Y.; Xue, L.; Yan, T.; Huang, D.; Deng, D. Self-Decomposable Mesoporous Doxorubicin@ Silica Nanocomposites for Nuclear Targeted Chemo-Photodynamic Combination Therapy. *ACS Appl Nano Mater* **2018**, *1* (4), 1976–1984.

(102) Balabushevich, N. G.; Kovalenko, E. A.; Le-Deygen, I. M.; Filatova, L. Y.; Volodkin, D.; Vikulina, A. S. Hybrid CaCO3-Mucin Crystals: Effective Approach for Loading and Controlled Release of Cationic Drugs. *Mater Des* **2019**, *182*, 108020.

(103) Zheng, H.; Zhang, Y.; Liu, L.; Wan, W.; Guo, P.; Nyström, A. M.; Zou, X. One-Pot Synthesis of Metal–Organic Frameworks with Encapsulated Target Molecules and Their Applications for Controlled Drug Delivery. *J Am Chem Soc* **2016**, *138* (3), 962–968.

(104) Ak, G.; Karakayalı, T.; Cin, A. N.; Özel, B.; Şanlıer, Ş. H. One Pot Green Synthesis of Doxorubicin and Curcumin Loaded Magnetic Nanoparticles and Cytotoxicity Studies. *Anti-Cancer Agents in Medicinal Chemistry (Formerly Current Medicinal Chemistry-Anti-Cancer Agents)* **2021**, *21* (18), 2563–2571.

(105) Prokopowicz, M. Bioactive Silica-Based Nanomaterials for Doxorubicin Delivery: Evaluation of Structural Properties Associated with Release Rate. *Materials Science and Engineering: C* **2013**, *33* (7), 3942–3950.

(106) Prokopowicz, M.; Czarnobaj, K.; Szewczyk, A.; Sawicki, W. Preparation and in Vitro Characterisation of Bioactive Mesoporous Silica Microparticles for Drug Delivery Applications. *Materials Science and Engineering: C* **2016**, *60*, 7–18.

(107) Prokopowicz, M.; Żegliński, J.; Gandhi, A.; Sawicki, W.; Tofail, S. A. M. Bioactive Silica-Based Drug Delivery Systems Containing Doxorubicin Hydrochloride: In Vitro Studies. *Colloids Surf B Biointerfaces* **2012**, *93*, 249–259.

(108) Dey, N.; Santhiya, D.; Das, A. Bio-Inspired Synthesis of Hollow Mesoporous Bioactive Glass Nanoparticles Using Calcium Carbonate as Solid Template. *ChemistrySelect* **2022**, *7* (12), e202200392.

(109) Oh, C.; Shim, S.-B.; Lee, Y.-G.; Oh, S.-G. Effects of the Concentrations of Precursor and Catalyst on the Formation of Monodisperse Silica Particles in Sol–Gel Reaction. *Mater Res Bull* **2011**, *46* (11), 2064–2069.

(110) Dixit, C. K.; Bhakta, S.; Kumar, A.; Suib, S. L.; Rusling, J. F. Fast Nucleation for Silica Nanoparticle Synthesis Using a Sol–Gel Method. *Nanoscale* **2016**, *8* (47), 19662–19667.

(111) Huo, Q.; Liu, J.; Wang, L.-Q.; Jiang, Y.; Lambert, T. N.; Fang, E. A New Class of Silica Cross-Linked Micellar Core− Shell Nanoparticles. *J Am Chem Soc* **2006**, *128* (19), 6447–6453.

(112) Kesse, X.; Vichery, C.; Nedelec, J.-M. Deeper Insights into a Bioactive Glass Nanoparticle Synthesis Protocol to Control Its Morphology, Dispersibility, and Composition. *ACS Omega* **2019**, *4* (3), 5768–5775.

(113) Siddiqui, B.; Al-Dossary, A. A.; Elaissari, A.; Ahmed, N. Exploiting Recent Trends for the Synthesis and Surface Functionalization of Mesoporous Silica Nanoparticles towards Biomedical Applications. *Int J Pharm X* **2022**, 100116.

(114) Racles, C.; Zaltariov, M.-F.; Peptanariu, D.; Vasiliu, T.; Cazacu, M. Functionalized Mesoporous Silica as Doxorubicin Carriers and Cytotoxicity Boosters. *Nanomaterials* **2022**, *12* (11), 1823.

(115) Heidari Nia, M.; Koshani, R.; Munguia-Lopez, J. G.; Kiasat, A. R.; Kinsella, J. M.; van de Ven, T. G. M. Biotemplated Hollow Mesoporous Silica Particles as Efficient Carriers for Drug Delivery. *ACS Appl Bio Mater* **2021**, *4* (5), 4201–4214.

(116) Ślósarczyk, A.; Paszkiewicz, Z.; Paluszkiewicz, C. FTIR and XRD Evaluation of Carbonated Hydroxyapatite Powders Synthesized by Wet Methods. *J Mol Struct* **2005**, *744*, 657–661.

(117) Bano, N.; Jikan, S. S.; Basri, H.; Adzila, S.; Zago, D. M. XRD and FTIR Study of A&B Type Carbonated Hydroxyapatite Extracted from Bovine Bone. In *AIP Conference Proceedings*; AIP Publishing LLC, 2019; Vol. 2068, p 20100.

(118) Zhang, Q.; Ye, Z.; Wang, S.-T.; Yin, J. Facile One-Pot Synthesis of PEGylated Monodisperse Mesoporous Silica Nanoparticles with Controllable Particle Sizes. *Chinese Chemical Letters* **2014**, *25* (2), 257–260.

(119) Ortiz-Islas, E.; Sosa-Arróniz, A.; Manríquez-Ramírez, M. E.; Rodríguez-Pérez, C. E.; Tzompantzi, F.; Padilla, J. M. Mesoporous Silica Nanoparticles Functionalized with Folic Acid for Targeted Release Cis-Pt to Glioblastoma Cells. *Reviews on Advanced Materials Science* **2021**, *60* (1), 25–37.

(120) ALOthman, Z. A. A Review: Fundamental Aspects of Silicate Mesoporous Materials. *Materials* **2012**, *5* (12), 2874–2902.

(121) Vazquez, N. I.; Gonzalez, Z.; Ferrari, B.; Castro, Y. Synthesis of Mesoporous Silica Nanoparticles by Sol–Gel as Nanocontainer for Future Drug Delivery Applications. *Boletín de la Sociedad Española de Cerámica y Vidrio* **2017**, *56* (3), 139–145.

(122) Chaudhary, A.; Dwivedi, C.; Gupta, A.; Nandi, C. K. One Pot Synthesis of Doxorubicin Loaded Gold Nanoparticles for Sustained Drug Release. *RSC Adv* **2015**, *5* (118), 97330–97334.

(123) Day, C. M.; Sweetman, M. J.; Song, Y.; Plush, S. E.; Garg, S. Functionalized Mesoporous Silica Nanoparticles as Delivery Systems for Doxorubicin: Drug Loading and Release. *Applied Sciences* **2021**, *11* (13), 6121.

(124) Szewczyk, A.; Skwira, A.; Prokopowicz, M. Drug-Loaded Mesoporous Silica/Calcium Phosphate Composites for Bone Regeneration. *Engineering of Biomaterials* **2019**, *22* (150).

(125) Liu, Y.; Nadeem, A.; Sebastian, S.; Olsson, M. A.; Wai, S. N.; Styring, E.; Engellau, J.; Isaksson, H.; Tägil, M.; Lidgren, L. Bone Mineral: A Trojan Horse for Bone Cancers. Efficient Mitochondria Targeted Delivery and Tumor Eradication with Nano Hydroxyapatite Containing Doxorubicin. *Mater Today Bio* **2022**, *14*, 100227.

(126) Duo, Y.; Li, Y.; Chen, C.; Liu, B.; Wang, X.; Zeng, X.; Chen, H. DOX-Loaded PH-Sensitive Mesoporous Silica Nanoparticles Coated with PDA and PEG Induce pro-Death Autophagy in Breast Cancer. *RSC Adv* **2017**, *7* (63), 39641–39650.

(127) Fallacara, A.; Baldini, E.; Manfredini, S.; Vertuani, S. Hyaluronic Acid in the Third Millennium. *Polymers (Basel)* **2018**, *10* (7), 701.

(128) Rudhramyna Gnaneshwar. *Hyaluronic Acid: A Wonder Molecule for the Cosmetic and Pharma Industries*; 2021. https://cdn.syngeneintl.com/2021/08/31014839/Hyaluronic-Acid-A-wonder-molecule-for-the-cosmetic-and-pharma-industries.pdf.

(129) Zhu, J.; Tang, X.; Jia, Y.; Ho, C.-T.; Huang, Q. Applications and Delivery Mechanisms of Hyaluronic Acid Used for Topical/Transdermal Delivery–a Review. *Int J Pharm* **2020**, *578*, 119127.

(130) Kozaka, S.; Kashima, A.; Wakabayashi, R.; Nakata, T.; Ueda, T.; Goto, M. Effective Transcutaneous Delivery of Hyaluronic Acid Using an Easy-to-Prepare Reverse Micelle Formulation. *Cosmetics* **2020**, *7* (3), 52.

(131) Yamada, M.; Dang, N.; Lin, L. L.; Flewell-Smith, R.; Jane L. Espartero, L.; Bramono, D.; Grégoire, S.; Belt, P. J.; Prow, T. W. Elongated Microparticles Tuned for Targeting Hyaluronic Acid Delivery to Specific Skin Strata. *Int J Cosmet Sci* **2021**, *43* (6), 738–747.

(132) Vázquez-González, M. L.; Calpena, A. C.; Domènech, Ò.; Montero, M. T.; Borrell, J. H. Enhanced Topical Delivery of Hyaluronic Acid Encapsulated in Liposomes: A Surface-Dependent Phenomenon. *Colloids Surf B Biointerfaces* **2015**, *134*, 31–39.

(133) Wu, X.; Zhang, H.; He, S.; Yu, Q.; Lu, Y.; Wu, W.; Ding, N.; Zhu, Q.; Chen, Z.; Ma, Y. Improving Dermal Delivery of Hyaluronic Acid by Ionic Liquids for Attenuating Skin Dehydration. *Int J Biol Macromol* **2020**, *150*, 528–535.

(134) Chen, M.; Gupta, V.; Anselmo, A. C.; Muraski, J. A.; Mitragotri, S. Topical Delivery of Hyaluronic Acid into Skin Using SPACE-Peptide Carriers. *Journal of controlled release* **2014**, *173*, 67–74.

(135) Tokudome, Y.; Komi, T.; Omata, A.; Sekita, M. A New Strategy for the Passive Skin Delivery of Nanoparticulate, High Molecular Weight Hyaluronic Acid Prepared by a Polyion Complex Method. *Sci Rep* **2018**, *8* (1), 1–9.

(136) Jones, J. R. Review of Bioactive Glass: From Hench to Hybrids. *Acta Biomater* **2013**, *9* (1), 4457–4486.

(137) Hench, L. L.; Jones, J. R. Bioactive Glasses: Frontiers and Challenges. *Front Bioeng Biotechnol* **2015**, *3*, 194.

(138) Baino, F.; Hamzehlou, S.; Kargozar, S. Bioactive Glasses: Where Are We and Where Are We Going? *J Funct Biomater* **2018**, *9* (1), 25.

(139) Ege, D.; Zheng, K.; Boccaccini, A. R. Borate Bioactive Glasses (BBG): Bone Regeneration, Wound Healing Applications, and Future Directions. *ACS Appl Bio Mater* **2022**, *5* (8), 3608–3622.

(140) Hench, L. L.; Splinter, R. J.; Allen, W. C.; Greenlee, T. K. Bonding Mechanisms at the Interface of Ceramic Prosthetic Materials. *J Biomed Mater Res* **1971**, *5* (6), 117–141.

(141) Hench, L. L.; Polak, J. M. Third-Generation Biomedical Materials. *Science (1979)* **2002**, *295* (5557), 1014–1017.

(142) El-Fiqi, A. Nano-bioactive Glass: Advances and Applications. *Bioactive Glasses and Glass-Ceramics: Fundamentals and Applications* **2022**, 173–201.

(143) Ji, L.; Xu, T.; Gu, J.; Liu, Q.; Zhou, S.; Shi, G.; Zhu, Z. Preparation of Bioactive Glass Nanoparticles with Highly and Evenly Doped Calcium Ions by Reactive Flash Nanoprecipitation. *J Mater Sci Mater Med* **2021**, *32* (5), 1–10.

(144) Zheng, K.; Kang, J.; Rutkowski, B.; Gawęda, M.; Zhang, J.; Wang, Y.; Founier, N.; Sitarz, M.; Taccardi, N.; Boccaccini, A. R. Toward Highly Dispersed Mesoporous Bioactive Glass Nanoparticles with High Cu Concentration Using Cu/Ascorbic Acid Complex as Precursor. *Front Chem* **2019**, *7*, 497.

(145) Khorshidi, H.; Zhang, C.; Najafi, E.; Ghasemi, M. Fresh, Mechanical and Microstructural Properties of Alkali-Activated Composites Incorporating Nanomaterials: A Comprehensive Review. *J Clean Prod* **2022**, 135390.

(146) Hajinezhad, M. R.; Shahraki, S.; Nikfarjam, Z.; Davodabadi, F.; Mirinejad, S.; Rahdar, A.; Sargazi, S.; Barani, M. Development of a New Vesicular Formulation for Delivery of Ifosfamide: Evidence from in Vitro, in Vivo, and in Silico Experiments. *Arabian Journal of Chemistry* **2023**, 105086.

(147) Xing, T.; Dong, C.; Hu, X.; Zhang, J.; Zhao, Y.; Xue, J.; Wang, X. Theoretical Study on the Interactions between Cellulose and Different Methyltriethoxysilane Hydrolysis Products. *Bioresources* **2022**, *17* (4).

(148) Nabeshi, H.; Yoshikawa, T.; Matsuyama, K.; Nakazato, Y.; Matsuo, K.; Arimori, A.; Isobe, M.; Tochigi, S.; Kondoh, S.; Hirai, T. Systemic Distribution, Nuclear Entry and Cytotoxicity of Amorphous Nanosilica Following Topical Application. *Biomaterials* **2011**, *32* (11), 2713–2724.

(149) Hirai, T.; Yoshikawa, T.; Nabeshi, H.; Yoshida, T.; Akase, T.; Yoshioka, Y.; Itoh, N.; Tsutsumi, Y. Dermal Absorption of Amorphous Nanosilica Particles after Topical Exposure for Three Days. *Pharmazie* **2012**, *67* (8), 742–743.

(150) Ostrowski, A.; Nordmeyer, D.; Boreham, A.; Brodwolf, R.; Mundhenk, L.; Fluhr, J. W.; Lademann, J.; Graf, C.; Rühl, E.; Alexiev, U. Skin Barrier Disruptions in Tape Stripped and Allergic Dermatitis Models Have No Effect on Dermal Penetration and Systemic Distribution of AHAPS-Functionalized Silica Nanoparticles. *Nanomedicine* **2014**, *10* (7), 1571–1581.

(151) Zhao, Z.; Li, M.; Zheng, L.; Yang, Y.; Cui, X.; Xu, T.; Zhang, W.; Wang, C. Noninvasive Transdermal Delivery of Mesoporous Silica Nanoparticles Using Deep Eutectic Solvent. *Journal of Controlled Release* **2022**, *343*, 43–56.

(152) Labouta, H. I.; Schneider, M. Interaction of Inorganic Nanoparticles with the Skin Barrier: Current Status and Critical Review. *Nanomedicine* **2013**, *9* (1), 39–54.

(153) Mehnath, S.; Karthikeyan, K.; Rajan, M.; Jeyaraj, M. Fabrication of Bone-Targeting Hyaluronic Acid Coupled Alendronate-Bioactive Glass for Osteosarcoma Therapy. *Mater Chem Phys* **2021**, *273*, 125146.

(154) Sergi, R.; Bellucci, D.; Cannillo, V. A Review of Bioactive Glass/Natural Polymer Composites: State of the Art. *Materials* **2020**, *13* (23), 5560.

(155) Coulson-Thomas, V. J.; Gesteira, T. F. Dimethylmethylene Blue Assay (DMMB). *Bio Protoc* **2014**, *4* (18), e1236–e1236.

(156) Scott, J. E.; Cummings, C.; Brass, A.; Chen, Y. Secondary and Tertiary Structures of Hyaluronan in Aqueous Solution, Investigated by Rotary Shadowing-Electron Microscopy and Computer Simulation. Hyaluronan Is a Very Efficient Network-Forming Polymer. *Biochemical Journal* **1991**, *274* (3), 699–705.

(157) Choi, K.-M.; Kuroda, K. Double Function of Tris (Hydroxymethyl) Aminomethane (THAM) for the Preparation of Colloidal Silica Nanospheres and the Conversion to Ordered Mesoporous Carbon. *Chemical Communications* **2011**, *47* (39), 10933–10935.

(158) Demadis, K. D.; Pachis, K.; Ketsetzi, A.; Stathoulopoulou, A. Bioinspired Control of Colloidal Silica in Vitro by Dual Polymeric Assemblies of Zwitterionic Phosphomethylated Chitosan and Polycations or Polyanions. *Adv Colloid Interface Sci* **2009**, *151* (1–2), 33–48.

(159) Lechner, C. C.; Becker, C. F. W. Silaffins in Silica Biomineralization and Biomimetic Silica Precipitation. *Mar Drugs* **2015**, *13* (8), 5297–5333.

(160) Zheng, C.; Levenston, M. E. Fact versus Artifact: Avoiding Erroneous Estimates of Sulfated Glycosaminoglycan Content Using the Dimethylmethylene Blue Colorimetric Assay for Tissue-Engineered Constructs. *Eur Cell Mater* **2015**, *29*, 224.

(161) Dey, N.; Santhiya, D.; Das, A. One-Pot Synthesis of Doxorubicin-Bioactive Glass-Ceramic Hybrid Nanoparticles through a Bio-Inspired Route for Anti-Cancer Therapy. *ChemistrySelect* **2023**, *8* (5), e202203664.

(162) Abd El-Aziz, A. M.; Abd El-Fattah, A.; El-Maghraby, A.; Ghareeb, D. A.; Kandil, S. Viscoelasticity, Mechanical Properties, and in Vitro Bioactivity of Gelatin/Borosilicate Bioactive Glass Nanocomposite Hydrogels as Potential Scaffolds for Bone Regeneration. *Polymers (Basel)* **2021**, *13* (12), 2014.

(163) Fallacara, A.; Marchetti, F.; Pozzoli, M.; Citernesi, U. R.; Manfredini, S.; Vertuani, S. Formulation and Characterization of Native and Crosslinked Hyaluronic Acid Microspheres for

Dermal Delivery of Sodium Ascorbyl Phosphate: A Comparative Study. *Pharmaceutics* **2018**, *10* (4), 254.

(164) Li, Q.; Li, M.; Zhu, P.; Wei, S. In Vitro Synthesis of Bioactive Hydroxyapatite Using Sodium Hyaluronate as a Template. *J Mater Chem* **2012**, *22* (38), 20257–20265.

(165) Taghian Dehaghani, M.; Ahmadian, M.; Fathi, M. Synthesis, Characterization, and Bioactivity Evaluation of Amorphous and Crystallized 58s Bioglass Nanopowders. *Int J Appl Ceram Technol* **2015**, *12* (4), 867–874.

(166) Lukowiak, A.; Lao, J.; Lacroix, J.; Nedelec, J.-M. Bioactive Glass Nanoparticles Obtained through Sol–Gel Chemistry. *Chemical Communications* **2013**, *49* (59), 6620–6622.

(167) Pavlath, A. E.; Gregorski, K. S. Atmospheric Pyrolysis of Carbohydrates with Thermogravimetric and Mass Spectrometric Analyses. *J Anal Appl Pyrolysis* **1985**, *8*, 41–48.

(168) Lefebvre, L.; Gremillard, L.; Chevalier, J.; Zenati, R.; Bernache-Assolant, D. Sintering Behaviour of 45S5 Bioactive Glass. *Acta Biomater* **2008**, *4* (6), 1894–1903.

(169) Murzyn, P.; Malata, G.; Wiśniewska, J.; Kapeluszna, E.; Nocuń-Wczelik, W. Characterization of 40-Year-Old Calcium Silicate Pastes by Thermal Methods and Other Techniques. *J Therm Anal Calorim* **2019**, *138*, 4271–4278.

(170) Ricci, V.; Zonari, D.; Cannito, S.; Marengo, A.; Scupoli, M. T.; Malatesta, M.; Carton, F.; Boschi, F.; Berlier, G.; Arpicco, S. Hyaluronated Mesoporous Silica Nanoparticles for Active Targeting: Influence of Conjugation Method and Hyaluronic Acid Molecular Weight on the Nanovector Properties. *J Colloid Interface Sci* **2018**, *516*, 484–497.

(171) Hate, S. S.; Reutzel-Edens, S. M.; Taylor, L. S. Influence of Drug–Silica Electrostatic Interactions on Drug Release from Mesoporous Silica-Based Oral Delivery Systems. *Mol Pharm* **2020**, *17* (9), 3435–3446.

(172) Sanjay, C.; Ghate, V. M.; Lewis, S. A. Mesoporous Silica Particles for Dermal Drug Delivery: A Review. *International Journal of Applied Pharmaceutics* **2018**, 23–26.

(173) Umaran, M. V. A.; Menchavez, R. L. Aqueous Dispersion of Red Clay-Based Ceramic Powder with the Addition of Starch. *Materials Research* **2013**, *16*, 375–384.

(174) Kotla, N. G.; Bonam, S. R.; Rasala, S.; Wankar, J.; Bohara, R. A.; Bayry, J.; Rochev, Y.; Pandit, A. Recent Advances and Prospects of Hyaluronan as a Multifunctional Therapeutic System. *Journal of Controlled Release* **2021**, *336*, 598–620.

(175) Fakhari, A.; Phan, Q.; Thakkar, S. V; Middaugh, C. R.; Berkland, C. Hyaluronic Acid Nanoparticles Titrate the Viscoelastic Properties of Viscosupplements. *Langmuir* **2013**, *29* (17), 5123–5131.

(176) Vivero-Escoto, J. L.; Slowing, I. I.; Trewyn, B. G.; Lin, V. S. Mesoporous Silica Nanoparticles for Intracellular Controlled Drug Delivery. *Small* **2010**, *6* (18), 1952–1967.

(177) Jones, J. R.; Brauer, D. S.; Hupa, L.; Greenspan, D. C. Bioglass and Bioactive Glasses and Their Impact on Healthcare. *Int J Appl Glass Sci* **2016**, *7* (4), 423–434.

(178) Rancan, F.; Gao, Q.; Graf, C.; Troppens, S.; Hadam, S.; Hackbarth, S.; Kembuan, C.; Blume-Peytavi, U.; Rühl, E.; Lademann, J. Skin Penetration and Cellular Uptake of Amorphous Silica Nanoparticles with Variable Size, Surface Functionalization, and Colloidal Stability. *ACS Nano* **2012**, *6* (8), 6829–6842.

(179) Morhenn, V. B.; Lemperle, G.; Gallo, R. L. Phagocytosis of Different Particulate Dermal Filler Substances by Human Macrophages and Skin Cells. *Dermatologic Surgery* **2002**, *28* (6), 484–490.

(180) Mo, C.; Lu, L.; Liu, D.; Wei, K. Development of Erianin-Loaded Dendritic Mesoporous Silica Nanospheres with pro-Apoptotic Effects and Enhanced Topical Delivery. *J Nanobiotechnology* **2020**, *18* (1), 1–14.

(181) Haq, A.; Goodyear, B.; Ameen, D.; Joshi, V.; Michniak-Kohn, B. Strat-M® Synthetic Membrane: Permeability Comparison to Human Cadaver Skin. *Int J Pharm* **2018**, *547* (1–2), 432–437.

(182) Arce, F. J.; Asano, N.; See, G. L.; Itakura, S.; Todo, H.; Sugibayashi, K. Usefulness of Artificial Membrane, Strat-M®, in the Assessment of Drug Permeation from Complex Vehicles in Finite Dose Conditions. *Pharmaceutics* **2020**, *12* (2), 173.

(183) Sapino, S.; Oliaro-Bosso, S.; Zonari, D.; Zattoni, A.; Ugazio, E. Mesoporous Silica Nanoparticles as a Promising Skin Delivery System for Methotrexate. *Int J Pharm* **2017**, *530* (1–2), 239–248.

(184) Boonen, J.; Baert, B.; Lambert, J.; De Spiegeleer, B. Skin Penetration of Silica Microparticles. *Die Pharmazie-An International Journal of Pharmaceutical Sciences* **2011**, *66* (6), 463–464.

(185) Ugazio, E.; Gastaldi, L.; Brunella, V.; Scalarone, D.; Jadhav, S. A.; Oliaro-Bosso, S.; Zonari, D.; Berlier, G.; Miletto, I.; Sapino, S. Thermoresponsive Mesoporous Silica Nanoparticles as a Carrier for Skin Delivery of Quercetin. *Int J Pharm* **2016**, *511* (1), 446–454.

(186) Valetti, S.; Thomsen, H.; Wankar, J.; Falkman, P.; Manet, I.; Feiler, A.; Ericson, M. B.; Engblom, J. Can Mesoporous Nanoparticles Promote Bioavailability of Topical Pharmaceutics? *Int J Pharm* **2021**, *602*, 120609.

(187) Arriagada, F.; Nonell, S.; Morales, J. Silica-Based Nanosystems for Therapeutic Applications in the Skin. *Nanomedicine* **2019**, *14* (16), 2243–2267.

(188) Nafisi, S.; Schäfer-Korting, M.; Maibach, H. I. Perspectives on Percutaneous Penetration: Silica Nanoparticles. *Nanotoxicology* **2015**, *9* (5), 643–657.